Title

The Lightness of Water Vapor, Clouds, and Tropical Climate



Author

Seidel, Seth

Publication Date

2023

Peer reviewed|Thesis/dissertation

The Lightness of Water Vapor, Clouds, and Tropical Climate

By

SETH D. SEIDEL

DISSERTATION

Submitted in partial satisfaction of the requirements for the degree of

DOCTOR OF PHILOSOPHY

in

Atmospheric Science

in the

OFFICE OF GRADUATE STUDIES

of the

UNIVERSITY OF CALIFORNIA

DAVIS

Approved:

Da Yang, Chair

Matthew Igel

Paul Ullrich

Committee in Charge

2023

Abstract

The Lightness of Water Vapor, Clouds, and Tropical Climate

by

Seth D. Seidel

Doctor of Philosophy in Atmospheric Science

University of California, Davis

Da Yang, Chair

In this dissertation I tell two stories about tropical climate. In the first story we investigate a negative climate feedback due to the lightness of water vapor. The molecular weight of water vapor is less than that of dry air, making humid air less dense than dry air at a given temperature and pressure. Using idealized cloud-resolving model simulations, we demonstrate that this vapor buoyancy in the humid regions of Earth's tropics must be balanced by warmer temperatures in the dry regions. This horizontal temperature difference gives rise to a negative lapse-rate-type climate feedback of about -0.15 $W/m^2/K$, which we call the vapor buoyancy feedback. Then, using a general circulation model, we show that this feedback is robust to the presence of planetary rotation and does not result in a countervailing water vapor feedback. Finally, using a one-dimensional radiative-convective climate model, we quantify the vapor-buoyancy feedback in relation to other clear-sky longwave feedbacks active in the tropical atmosphere.

In the second story we investigate the temperature of high clouds in the tropics. Tropical anvil clouds are generally observed to rise as the climate warms, causing their temperature to change little. However, the precise magnitude and mechanism of this temperature change remains the subject of some controversy. In this study, I conduct over 100 idealized experiments in a convection-permitting model. We note that the radiative tropopause – the location in the upper troposphere where radiative heating equals zero – warms at approximately the same rate as the cloud anvils so long as the simulations are performed using Earth-like parameters. From there, we show how radiative heating due to sunlight, carbon dioxide, and ozone all modify the temperature and warming trend of the anvil clouds.

# Contents

# The Lightness of Water Vapor, Clouds, and Tropical Climate

## 1 Introduction

According to the most recent IPCC report, a doubling of atmospheric $CO_2$ relative to its pre-industrial concentration is likely to result in 2.5º to 4.0º C of surface warming, though warmer or colder outcomes cannot be ruled out (Forster et al., 2021). Reducing this uncertainty has a potential global economic benefit in the trillions of dollars (Hope, 2015). As such, this *climate sensitivity* problem remains one of the most active areas of research in modern climate science. One path to narrowing the range of potential climate sensitivites is to improve our understanding of the underlying *climate feedbacks* – the sensitivities of top-of-atmosphere radiation to climate warming. The goal of my doctoral work is to help clarify the physics of particular climate feedbacks in the hope that this new knowledge may help to reduce our uncertainty regarding climate change.

Generally, there are two modeling approaches one may employ to study climate feedbacks. In the decomposition approach, one may analyze model outputs using offline radiative transfer calculations in order to achieve a complete decomposition of Earth's total climate sensitivity (see, for example, Zelinka et al., 2020). The advantage of that approach is that every feedback in the model is accounted for. However, along the way, one must combine potentially unrelated processes into a single feedback component. For example, feedbacks due to temperature change are all lumped into either a Planck (vertically uniform) or lapse-rate (vertically non-uniform) climate feedback. Clouds of different types and origins are all classified together based on their altitude and latitude band. These choices are necessarily arbitrary, obscuring our visibility into the underlying feedback processes. In the second approach, which I call the process-based approach, we forego the complete picture in order to evaluate specific, physically coherent feedback processes. This allows us to develop new intuitions about climate feedbacks and even to identify novel feedback processes which may be misrepresented in comprehensive climate models.

This dissertation ties together several contributions to our understanding of tropical climate feedbacks which were developed using the process-based approach. It is comprised solely of my first-author manuscripts. As such, it excludes a substantial portion of my PhD work related to vapor buoyancy, including my analyses of observational data (D. Yang & Seidel, 2020) and of Coupled Model Intercomparison Project (CMIP) data (D. Yang et al., 2022; D. Yang & Seidel, 2023). This choice allows for a more focused document.

In Chapter 2, we describe a novel climate feedback mechanism in which the small molecular weight of water vapor conspires with weak buoyancy gradients in the tropics to cause outsize atmospheric warming in tropical dry regions. We call the resulting increase in outgoing longwave radiation the *vapor-buoyancy feedback*. We proceed to test the feedback in a model experiment designed to contain all the necessary physics, but no more. In Chapter 3, we address two major outstanding questions from Chapter 2: (a) does the vapor-buoyancy feedback occur in an atmosphere with appreciable planetary rotation, and (b) does vapor buoyancy induce a countervailing positive water vapor feedback? We address both questions through modeling experiments in an idealized GCM. These experiments should (hopefully) convince the audience that the physics of the vapor-buoyancy feedback are robust.

Chapter 4 provides context for the vapor-buoyancy feedback. By introducing vapor buoyancy into a simple 1D climate model, we can compare the magnitude of the vapor-buoyancy feedback to other clear-sky longwave feedbacks across a range of climate states. The model also permits us to explore the critical longwave feedback transition from surface emission to atmospheric emission which occurs at surface temperatures near those of Earth's present-day tropics.

In Chapter 5, we shift our focus from the dry-region middle troposphere to clouds in the upper troposphere. Using a large collection of cloud-resolving simulations, we probe the limits of the Fixed Anvil Temperature (FAT) hypothesis, which predicts that high clouds rise as the climate warms so that their emission temperature changes little. We corroborate a long-standing assumption in the FAT literature that, for earth-like climates, the anvil level is closely tied to the sharp decline in radiative cooling below

tropopause. We further investigate the potential role of ozone as either enabling or confounding the physics of FAT.

## 1.1 Acknowledgements

The selection of a PhD advisor is the most important decision a student makes, but it is clouded by uncertainty. Based on a handful of conversations and emails, we must choose who will guide our work for half a decade and set the stage for the rest of our career. It feels even more risky if they have never had another student before. I was fortunate, though. Da Yang has been an insightful collaborator and supportive mentor throughout this process. There have been easily a dozen times in which I would have given up on a scientific question but for an insistence that we must find an angle to make it work.

My time in graduate school was greatly enriched by many personal and professional relationships. To my fellow members of the Yang group, Argel, Wenyu, Lin, and Hing: I learned a lot from each of you. Thank you to Argel, Lucas, and Leif for six years of friendship, and to all my officemates in Hoagland 236 for your camaraderie. Thank you to Matt for helpful discussions and mentorship over the years. Thank you to all the members of my committee for the feedback and other support you have offered over the years: Da, Matt, Paul, Bill, and Terry. Finally, I want to thank Lauren, my wife, for her unwavering love and support from the beginning of my PhD process to the end.

It is easy to lament academic peer review when it falls short, but a team of passionate reviewers greatly improved the manuscript that became Chapter 5 of this dissertation. They helped to transform a study I was which I was unsure of into something I felt proud of. To Dennis Hartmann, Thomas Birner, and one anonymous reviewer: Thank you.

The work presented in this dissertation was funded by several organizations: Berkeley Lab (through LDRD funding), the Packard Foundation, and the National Science Foundation. The computational resources required for the numerical experiments in Chapters 2, 3, and 5 were provided by the Department

of Energy National Energy Research Scientific Computing Center at Berkeley Lab and by the National Center for Atmospheric Research.

# 2 Vapor-Buoyancy Feedback in a Cloud-Resolving Model

**Abstract**

Moist air is lighter than dry air at the same temperature, pressure and volume because the molecular weight of water is less than that of dry air. We call this the *vapor buoyancy effect*. Although this effect is well documented, its impact on Earth's climate has been overlooked. Here we show that the lightness of water vapor helps to stabilize tropical climate by increasing the outgoing longwave radiation (OLR). In the tropical atmosphere, buoyancy is horizontally uniform. Then the vapor buoyancy in the moist regions must be balanced by warmer temperatures in the dry regions. These higher temperatures increase tropical OLR. This radiative effect increases with warming, leading to a negative climate feedback. At a near-present-day surface temperature, vapor buoyancy is responsible for a radiative effect of 1 $W/m^2$ and a negative climate feedback of about 0.15 $W/m^2/K$.

## 2.1 Introduction

Geological evidence suggests that tropical sea surface temperature (SST) varies considerably less than higher-latitude SST (Evans et al., 2018; Frieling et al., 2017; Keating-Bitonti et al., 2011; Pearson et al., 2007). Though this geological evidence reflects a wide range of uncertainty, the consensus is that tropical climate is more stable than extratropical climate. This local climate stability in the tropics has global implications. Global climate warming results in greater warming at the poles than in the tropics, weakening the meridional temperature gradient (Masson-Delmotte et al., 2014). This would alter the general circulation of the atmosphere. Past work has considered how the temperature gradient would decline with warming through the polar amplification of climate warming, caused by polar-region feedbacks (Budyko, 1969; Cvijanovic & Caldeira, 2015; Masson-Delmotte et al., 2014) or by enhanced poleward energy transport (Cai, 2005; Lee, 2014). Instead, we propose a low-latitude feedback that leads to tropical damping by emitting more energy to space with warming.

Tropical climate stability may be explained by negative climate feedbacks, which in a warming climate cause additional outgoing longwave radiation (OLR) or reduced shortwave absorption by the earth system. Previous studies have explored such feedback mechanisms. Lindzen et al. proposed that increased sea surface temperature in the tropics would result in reduced cirrus clouds, leading to enhanced OLR from Earth's atmosphere (Lindzen et al., 2001). Studies have also proposed that the ability of atmospheric circulations to transport energy and to create dry, emissive regions is key to regulate tropical climate (Cai, 2005; Pierrehumbert, 1995). More recent studies have considered convection's tendency to aggregate more in warmer climates, yielding broader and drier clear-sky regions, efficiently emitting longwave radiation to space (Bony et al., 2016; Emanuel et al., 2014; Mauritsen & Stevens, 2015). However, each of these mechanisms is currently subject to considerable uncertainties in a warming climate (Bony et al., 2015; Boucher et al., 2013).

Here, we offer another explanation of the tropics' climate stability by way of a robust clear-sky feedback. The magnitude of this feedback may be estimated with greater certainty than for feedbacks depending on changes in clouds and circulation. In a recent paper, Yang and Seidel (D. Yang & Seidel, 2020) proposed a clear-sky vapor buoyancy feedback that stabilizes tropical climate. Using a semi-analytical model, the authors estimated that the radiative effect is about 2–4 W/m2 and that the feedback parameter is about 0.2 W/m2/K, which seem to be substantial for Earth's climate. The authors further suggested that this effect exponentially increases with climate warming, so it could effectively stabilize tropical climate at higher temperatures. However, due to their theoretical approach, the key ingredients of the feedback are assumed or even imposed, as opposed to self-emerging in the model. For example, they imposed a weak buoyancy gradient (WBG) in the tropical free troposphere, rather than explicitly simulating it in the model. The magnitude of the proposed feedback critically depends on water vapor's distribution in the tropical atmosphere, which was also not explicitly represented. Here we will explicitly simulate atmospheric circulations and water vapor distributions using a cloud-resolving model (CRM). CRMs have a typical grid spacing of O(1 km) and can adequately simulate deep convective storms. In our numerical

experiments, an atmosphere with weak horizontal buoyancy gradient and realistic water vapor distribution will self-emerge. This paper will show that the lightness of water vapor has a profound impact on Earth's energy balance and climate stability.

### 2.1.1 The Vapor Buoyancy Feedback

The "recipe" for the proposed mechanism requires three key ingredients: (I1) large-scale circulations that organize the tropics into comparatively moist and dry regions (Pierrehumbert, 1995), (I2) a weak horizontal buoyancy gradient (WBG) (Charney, 1963; Huang et al., 2013; Sobel et al., 2002), and (I3) the vapor buoyancy effect itself. While each of these ideas has a long history, the novelty of our proposal lies in their synthesis.

(I1) The tropical atmosphere is organized into comparatively moist and dry regions by large-scale circulations, e.g. the Hadley and Walker circulations (Fig. 2.1A). The ascending branches of these circulations are characterized by ubiquitous deep convection (thunderstorms) and high relative humidity (RH). There, the atmosphere is opaque to longwave radiation and may approach a local runaway greenhouse state, in which OLR remains roughly constant with surface warming (INGERSOLL AP, 1969; Pierrehumbert, 1995). The descending branches are characterized by clear skies and low RH. The circulations transport energy from the moist region to the dry region, where longwave radiation is emitted from Earth's atmosphere. While much of the subtropics are part of such a dry region associated with the subsiding branch of the Hadley circulations, even large parts of the deep tropics can be characterized by dry, subsiding air due to east-west atmospheric circulations, such as the Walker circulation. Since the moist region's OLR is relatively insensitive to surface warming, it is the properties of the dry region – its temperature, water vapor profiles, and spatial area – that primarily determine the tropics' OLR and how OLR responds to climate forcings.

(I2) We are interested in in the atmospheric temperature in the dry region and thereby in how buoyancy is distributed in the tropical atmosphere. Buoyancy is an upward force by virtue of the density difference

between an air parcel and the surrounding environment. In Earth's atmosphere, buoyancy is determined by its temperature and water vapor mixing ratio (kg/kg). We shall use this relationship between buoyancy, temperature, and water vapor content to understand the dry-region temperature profile. The weak buoyancy gradient (WBG) approximation simplifies the dynamics of the tropical free troposphere by assuming buoyancy to be horizontally homogeneous. In the tropics, the effect of planetary rotation is comparatively small, so gravity waves can effectively smooth out horizontal buoyancy anomalies (Charney, 1963; Huang et al., 2013; Sobel et al., 2002). Sometimes this is further simplified to the weak temperature gradient approximation (WTG), which assumes that water vapor has a negligible effect on buoyancy. However, for our purposes we must be more precise.

(I3) The vapor buoyancy effect, also known as the virtual effect, accounts for how the molecular weight of water vapor influences the buoyancy of moist air. Water vapor has a molecular mass of 18 g/mol, considerably less than the mass of dry air at 29 g/mol. A parcel of moist air is lighter and more buoyant than a parcel of dry air at the same temperature and pressure. To capture this effect, we use virtual temperature to represent buoyancy:

$$T_v = T\left(\frac{1 + r/\epsilon}{1 + r}\right) \qquad [1]$$

$T$ is the parcel's temperature (K), $r$ is its water vapor mixing ratio (kg/kg), and $\epsilon = M_v/M_d$ where $M_v$ and $M_d$ are the average molecular mass of water vapor and dry air, respectively.

The above ingredients produce the vapor buoyancy feedback (Fig. 2.1). In the tropical atmosphere, the temperature profile of the moist region is set by convective storms, and temperature must increase toward the dry region, balancing reduced vapor buoyancy according to WBG (dark red line in Fig. 2.1a). This makes the dry region warmer than it otherwise would be in the absence of vapor buoyancy (light red line in Fig. 2.1a). The greater temperature leads to more OLR. This is a negative radiative effect, and its magnitude depends on the humidity contrast between the moist and dry regions (Fig. 2.1b). Assuming RH remains the same, the humidity contrast increases with warming, leading to a larger horizontal temperature

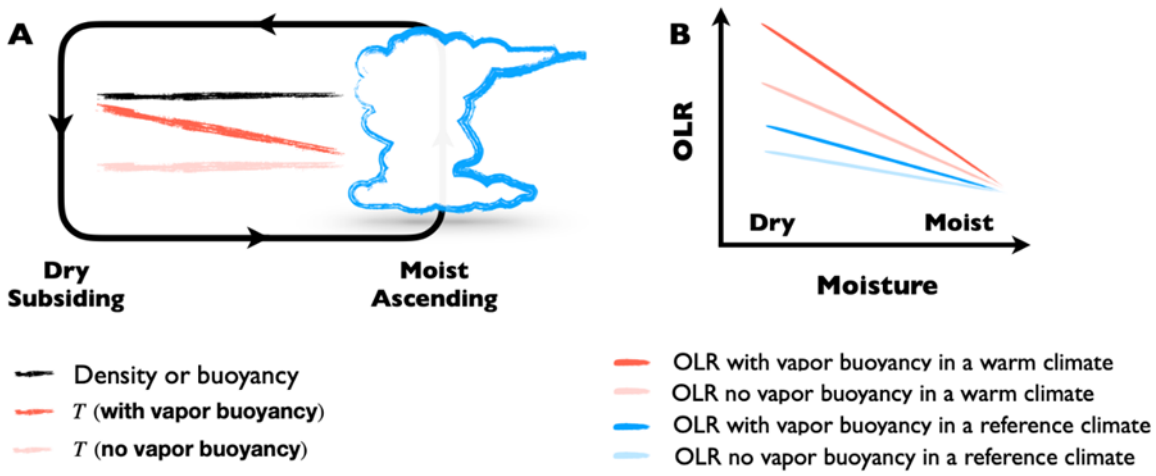


**Figure 2.1**. **Proposed mechanism of the vapor buoyancy feedback. (A)** The atmosphere is organized into moist and dry regions, with the dry region being responsible for most of the atmosphere's OLR. In an atmosphere with vapor buoyancy, the weak buoyancy gradient necessitates a warmer dry region than if there were no vapor buoyancy effect, which increases OLR. **(B)** The expected dependence of OLR on column water vapor according to our hypothesis. We expect there to be little difference in the OLR originating from the moist regions, but the vapor buoyancy effect will yield greater OLR in the dry region. We expect this OLR difference to be greater in warmer climates. This constitutes a negative climate feedback.

difference and thereby a stronger radiative effect of vapor buoyancy in a warmer climate (Fig. 2.1b). This is thus a negative feedback, stabilizing the climate.

The vapor buoyancy feedback represents a substantial departure from the current understanding of the tropical lapse rate feedback, in which latent heating causes the moist adiabatic lapse rate to decline with climate warming (Flato et al., 2013). The upper troposphere warms more than the surface, increasing OLR. That process can be represented in a single column. However, the origin and amplitude of the vapor buoyancy feedback depend on horizontal distributions of temperature and moisture. Understanding the vapor buoyancy feedback, therefore, requires at least two columns (D. Yang & Seidel, 2020) or even two dimensions as in this study.

We make three predictions according to this theory:

(P1) There is a substantial horizontal temperature gradient in the lower free troposphere where WBG is effective and where water vapor is abundant (Fig. 2.1a).

(P2) The vapor buoyancy effect increases OLR (Fig. 2.1).

(P3) The strength of this effect increases with surface temperature (Fig. 2.1b).

## 2.2 Methods

***Cloud-Resolving Simulations***

We simulate convective self-aggregation in a non-rotating 2D atmosphere using the System for Atmospheric Modeling (SAM, version 6.10.8) (M. F. Khairoutdinov & Randall, 2003). The radiation scheme is that of the National Center for Atmospheric Research (NCAR) Community Atmosphere Model, version 3 (CAM3) (Collins et al., 2006). The microphysics is the SAM one-moment parameterization. The horizontal domain size is 2048 km, and the model top is at 35 km. The horizontal resolution is 2 km. The vertical resolution is 50m for the lowest 1km and increases to 600 m above 3 km. A sponge layer occupies the upper 10km of the model domain. The incoming solar radiation is fixed at 413.9 $W/m^2$ to match the annual mean insolation on the equator. We fix the SST to a uniform value, and we perform simulations for a wide range of SSTs, from 280 K to 320 K. Each simulation is integrated for 1000 days. This paper presents two types of simulations: control simulations with the vapor buoyancy effect, and mechanism-denial simulations without the vapor buoyancy effect. We switch off the vapor buoyancy effect by removing the buoyancy dependence on water vapor in the vertical momentum equation, following Yang (D. Yang, 2018b). A CRM typically has horizontal grid spacing of $O$ (1 km), which is sufficient to resolve deep convective clouds and has been widely used to study tropical convection. However, in order to fully resolve boundary layer clouds, one would need large eddy simulations with typical horizontal grid spacing of about 50 m. Because our proposed mechanism mainly concerns how vapor buoyancy affects clear-sky temperature profiles in the free troposphere, CRM simulations are sufficient.

***Analysis in moisture space***

We analyze the model output in precipitable water (PW) space. Each simulation contains 1024 columns, integrated over 1000 days, saved in 4-hour intervals. Removing the first 250 days of each simulation, we calculated the one-day moving mean of the output and then sorted each of the 1024 × 4500 columns according the percentile rank of PW. We then calculate an average profile at each percentile, yielding 100 percentile-ranked average columns for each simulation. We could instead rank columns according to column relative humidity, but the results presented here are robust to either method. We use the column-sorted data to test the three predictions.

***Radiative Kernel Calculation***

We use the CAM radiative transfer model (Collins et al., 2006; Zender, 1999) to compute radiative kernels (Cronin & Wing, 2017; Soden et al., 2008). The kernels represent the change in clear-sky OLR with respect to atmospheric temperature profile, or $\frac{\partial OLR}{\partial T}(p)$ and with respect to the vapor profile, $\frac{\partial OLR}{\partial q}(p)$. Following the method introduced by Cronin and Wing (Cronin & Wing, 2017), we calculate "approximate" kernels using the precipitable water-sorted columns presented previously. The kernels are based on the control simulations. We calculate each of these partial derivatives by perturbing the temperature or water vapor at a single model level, then running the radiative transfer scheme on both the original and the perturbed atmospheric profiles. We use perturbations of + 0.5 K in temperature and -1% in specific humidity to calculate the kernels. The temperature and water vapor radiative kernels for the simulations of 290 K, 300 K, and 310 K SSTs are presented in Figure 2.A1.1

## 2.3 Results

We test the vapor buoyancy feedback using 2D cloud-resolving simulations of idealized overturning circulations with identifiable moist and dry patches. We perform numerical simulations over a wide range of SSTs. At a given SST, we perform two simulations: a *control simulation* with the vapor buoyancy effect,

and a *mechanism-denial simulation* without the vapor buoyancy effect. This pair of simulations highlights the effect of vapor buoyancy. A similar approach has been widely used, *e.g.*, to study the effect of clouds in climate models. To implement the idealized circulations, we employ convective self-aggregation, a phenomenon in which an atmosphere under uniform boundary conditions spontaneously develops a large-scale overturning circulation with an ascending region characterized by deep convection and a subsiding region characterized by anomalously dry conditions (Bretherton et al., 2005; Holloway & Woolnough, 2016; C. Muller & Bony, 2015; C. J. Muller & Held, 2012; D. Yang, 2018a). Convective self-aggregation is particularly suitable for investigating the vapor buoyancy feedback because its steady overturning circulation has discernible, persistent moist and dry regions. The model setup for these simulations is discussed in Methods.

Convective self-aggregation is successfully simulated in a wide range of climates. Figure 2.2 shows the evolution of precipitable water (PW) over space and time at different SSTs, without and with the vapor buoyancy effect. Notably, the horizontal scale of self-aggregation depends on the temperature and the presence of the vapor buoyancy effect. Yang (D. Yang, 2018b) showed that the vapor buoyancy effect is responsible for the scale of self-aggregation. This is because the horizontal scale is principally determined by the horizontal mass flux within the boundary layer, which is in turn determined by the boundary layer density gradient. In a self-aggregated boundary layer, most of the density differences across the domain arise mainly due to vapor buoyancy, rather than to temperature buoyancy. Therefore, by removing the vapor buoyancy effect we have also removed a principal scale-setting mechanism.

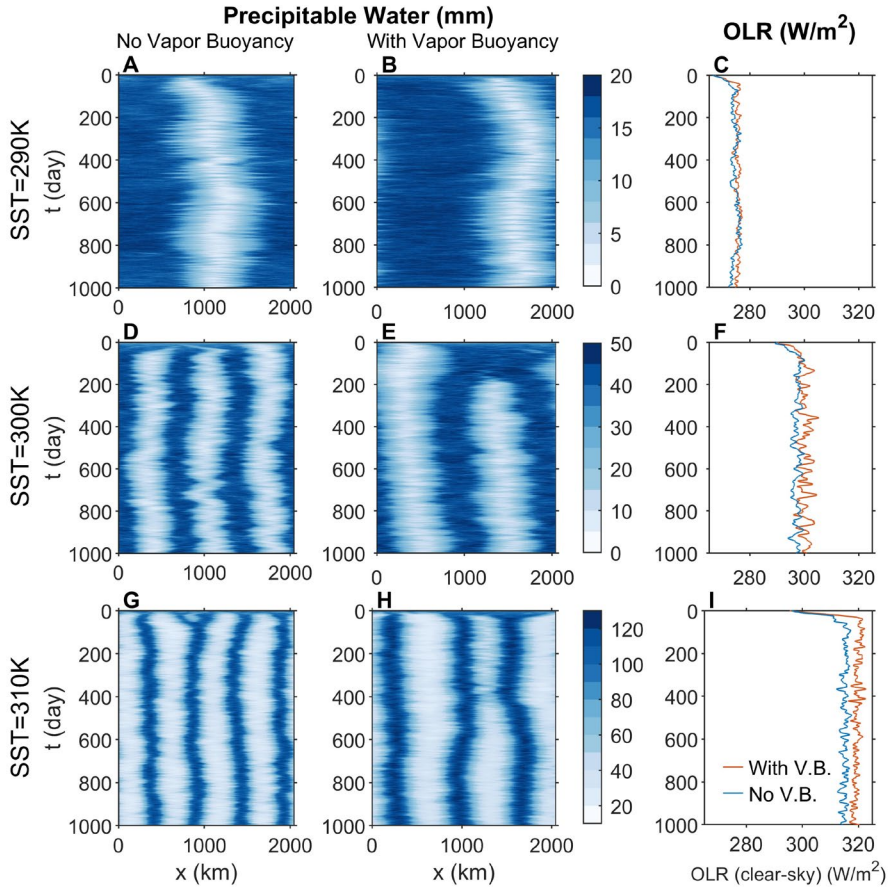


**Figure 2.2. Simulated water vapor fields and OLR in different climates. (A, B, D, E, G, H)** Precipitable water over time, showing convective self-aggregation. During the course of a simulation, the atmosphere organizes into distinct moist and dry regions despite the uniform boundary conditions. Deep convection occurs almost exclusively in the moist regions, while clear skies and low humidity characterize the dry region. **(C, F, I)** A 10-day moving average of clear-sky outgoing longwave radiation (OLR). Once a distinct dry region develops in each simulation, the atmosphere with vapor buoyancy exhibits greater radiative cooling.

### 2.3.1 Prediction 1: A substantial temperature gradient

Figure 2.3 shows that the vapor buoyancy effect is responsible for substantial temperature gradients in the lower free troposphere. The horizontal axis is the percentile rank of PW, the sorting method for which is covered in the Methods section. The red lines are absolute temperature contours (isotherms), and the black lines are virtual temperature contours (isopycnals). Both atmospheres exhibit negligible horizontal gradients in buoyancy, but there is a substantial temperature gradient in the control atmosphere with vapor buoyancy, which has also been observed in the real tropical atmosphere (D. Yang & Seidel, 2020). The

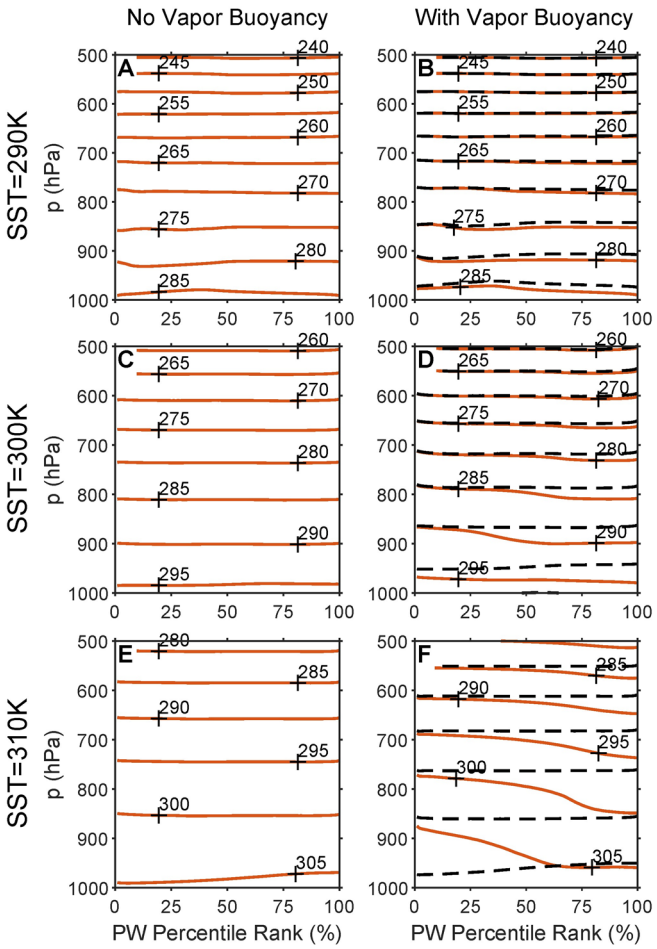


**Figure 2.3**. **Temperature and virtual temperature fields as organized by column precipitable water.** Red contours correspond to absolute temperature (isotherms) and black contours correspond to virtual temperature (i.e. density) for the pair of simulations with **(A, B)** SST = 290 K, **(C, D)** SST = 300 K, and **(E, F)** SST = 310 K. The temperature profile is nearly identical in the moist region of either atmosphere. The virtual temperature gradient is weak in the free troposphere, warming the dry columns when the vapor buoyancy effect is turned on.

temperature profiles are nearly identical in the moist region of either atmosphere, but they diverge towards the dry regions: the vapor buoyancy effect warms the lower free troposphere in the dry region. Comparing the 90$^{th}$ percentile column to the 10$^{th}$ percentile column in the 300K simulation, the temperature difference peaks at 1.7 K, at a pressure level of 872 hPa. Given that this difference is not present in the mechanism-denial simulations where water vapor does not affect buoyancy, we can attribute warming to the vapor buoyancy effect.

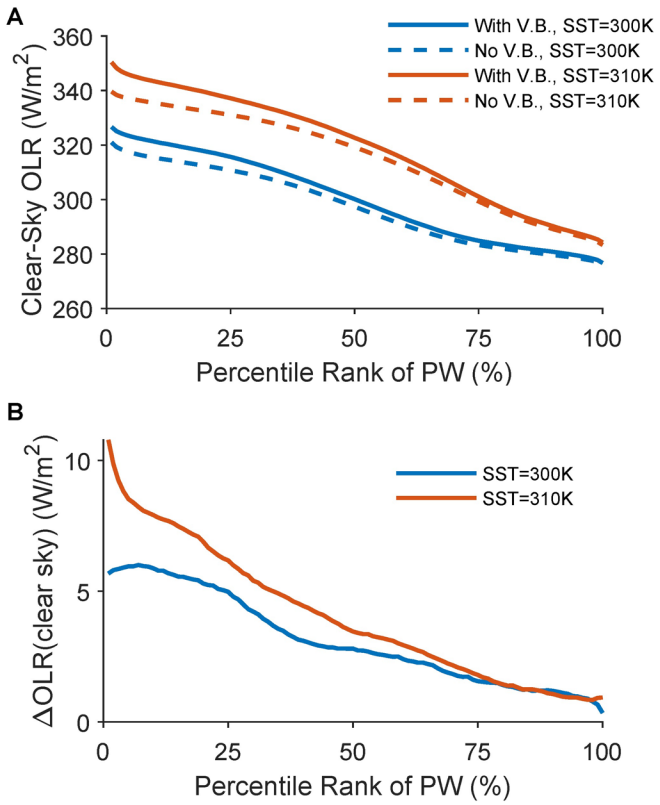


**Figure 2.4**. **Simulated difference in OLR. (A)** The relationship between clear-sky OLR and the percentile rank of precipitable water, with and without the vapor buoyancy effect. There are similar values for OLR in the moist region, but the with-vapor-buoyancy atmosphere emits greater OLR in the dry region, consistent with the prediction in Fig. 2.1B. **(B)** The increase in OLR from adding the vapor buoyancy effect.

### 2.3.2 Prediction 2: The vapor buoyancy effect increases OLR

We shall compare control and mechanism-denial simulations at SST=300K, showing that the vapor buoyancy effect increases OLR at a given PW rank and that the vapor buoyancy effect increases the domain-average OLR by warming the lower troposphere of the dry, subsiding region. We focus on the clear-sky OLR diagnostics because our prediction is based upon clear-sky radiation and because we found the all-sky and clear-sky OLR increases to be of similar magnitudes. The following chapter reports the all-sky feedback for a similar experiment in a GCM Using the same column-sorting approach as for Fig. 2.3, we have calculated clear-sky OLR's dependence upon PW. Figure 2.4a shows that the vapor buoyancy effect

enhances clear-sky OLR. The strength of this effect is near zero in the moistest columns but increases gradually towards the driest columns. This is consistent with the prediction presented in Fig. 2.1b. The time series of domain-mean OLR are shown in Fig. 2.2. As the atmospheres self-aggregate, OLR in the control experiment exceeds that in the mechanism-denial experiment, and this difference persists. Averaged over the last 750 days of simulation, this effect accounts for a 3.1 W/m$^2$ increase in OLR in the Earth-like reference climate with SST = 300 K. Compared to the 4 W/m$^2$ direct radiative forcing associated with the doubling atmospheric $CO_2$, vapor buoyancy's influence on OLR is quite profound.

### 2.3.3 Prediction 3: The strength of this effect increases with SST

Figure 2.4A shows clear-sky OLR for the control and mechanism-denial simulations for 300 K and 310 K SSTs. The gap in clear-sky OLR between the two simulations is greater in the SST = 310 K simulation pair. Figure 2.4B shows this more clearly, depicting the difference in clear-sky OLR in either pair of simulations. This confirms the prediction in Fig. 2.1B.

To see the domain-mean differences in OLR, we refer first to the time series in Fig. 2.2. The difference in domain-mean OLR increases with SST. Figure 2.5A depicts the domain- and time-averaged change in clear-sky OLR due to vapor buoyancy across a wide range of climates:

$$\Delta OLR = OLR_v - OLR_{nv} \qquad [2]$$

where *v* and *nv* denote the control (with vapor buoyancy) and mechanism-denial simulations (no vapor buoyancy), respectively. As shown in Fig. 2.5A, $\Delta OLR$ is 3.1 W/m$^2$ when SST=300K and 4.1 W/m$^2$ when SST=310K. $\Delta OLR$ in general increases with SST, acting as a negative climate feedback. If a perturbation were to warm the climate, the vapor buoyancy effect would counteract that by increasing OLR. However, the signal in Fig. 2.5A results from a combination of factors, including the vapor buoyancy feedback, changes in water vapor distribution, and others, so ΔOLR does not increase monotonically with surface temperature. To separate these effects from one another, we perform radiative kernel calculations.

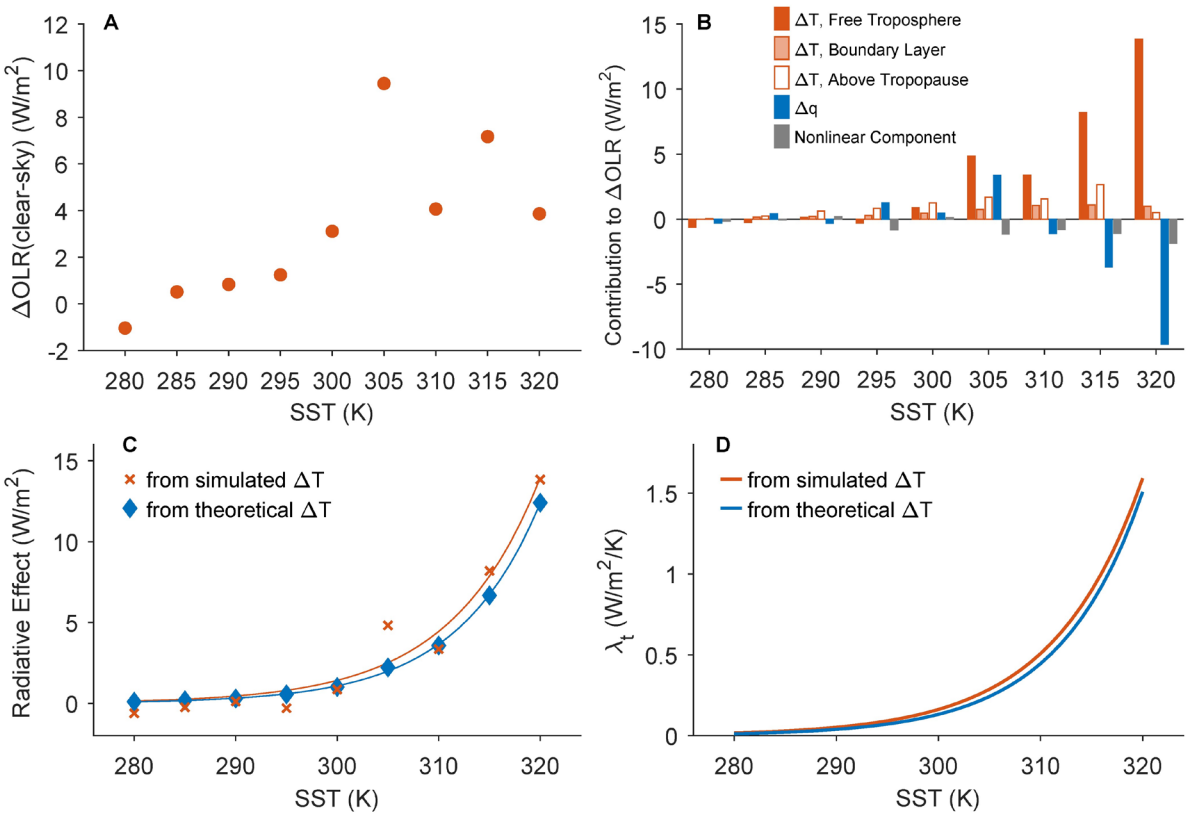


**Figure 2.5**. **Feedback analysis. (A)** The increase in clear-sky OLR from adding the vapor buoyancy effect. Since radiative cooling increases with SST, this constitutes a negative climate feedback. **(B)** Domain-averaged ΔOLR decomposed into components due to the linear effects of both temperature and water vapor. The temperature contribution is split into free troposphere, boundary layer, and above tropopause components. The boundary layer top was assumed at 900hPa. Tropopause was identified as the lowest level where domain- and time-averaged radiative heating is approximately zero in the simulation with vapor buoyancy. The nonlinear component is calculated as the residual of the ΔOLR from the simulations. The free troposphere temperature component contains the proposed vapor buoyancy radiative effect. **(C)** The marks represent the radiative effect, which is calculated by multiplying the temperature radiative kernel by the $\Delta T$ profiles. The curves represent exponential fits to the marks. **(D)** The vapor buoyancy feedback parameter $\lambda_t$, calculated based on the exponential fits, shows the strength of the vapor buoyancy feedback.

### 2.3.4 The Components of $\Delta OLR$

We use radiative kernels to quantify the share of $\Delta OLR$ that results from changes in both temperature and water vapor, respectively, between the control and mechanism-denial simulations. Refer to the Methods section for a description of the radiative kernels and how they are applied to the simulation data. The kernels themselves are presented in the appendix to this chapter. Figure 2.5B shows the result of the kernel analysis,

which is a linear decomposition of $\Delta OLR$ into its components due to the differences in the temperature and moisture fields between the two simulations at a given SST.

The proposed radiative effect of vapor buoyancy results from the free-troposphere temperature difference, $\Delta T$, between the control simulation and the mechanism-denial simulation (the left column of Fig. 2.6). The free troposphere lies between the boundary layer top and the tropopause. We take $p_{bl} = 900$ hPa as the boundary layer top. Considering the tropopause as the radiative-convective boundary, we have identified it where radiative cooling rate is approximately zero. The free-troposphere temperature component of $\Delta OLR$ is an estimate of the radiative effect of vapor buoyancy (dark red bars in Fig. 2.5b). Since the water vapor field is held constant when applying the temperature kernel, this estimate holds the area of the dry, subsiding region as constant between simulations. Therefore, the calculated OLR difference is only due to temperature

changes. This method estimates the radiative effect as about 0.9 W/m$^2$ at 300 K SST. This increases to about 14 W/m$^2$ at 320 K SST, suggesting a robust negative climate feedback mechanism in the atmosphere with vapor buoyancy.

The linear component of ΔOLR associated with differences in water vapor contributes significantly (blue bars in Fig. 2.5b). This result suggests that water vapor distribution changes when we switch off the

vapor buoyancy effect, which is not considered in the simple model developed by Yang and Seidel (D. Yang & Seidel, 2020). The water vapor contribution to ΔOLR reinforces the radiative effect of vapor buoyancy around the reference climate but significantly counteracts it in warmer climates, lacking a robust trend with SST. Understanding this behavior would require us to study how vapor buoyancy affects the water vapor distribution, which is beyond the scope of this paper. We have also computed the boundary-layer contributions to ΔOLR and find that the effect is negligible. The temperature above tropopause is a positive component of ΔOLR, possibly because the stratosphere is in radiative balance with a warmer troposphere in the control simulations due to vapor buoyancy. This stratosphere component is substantial in the reference

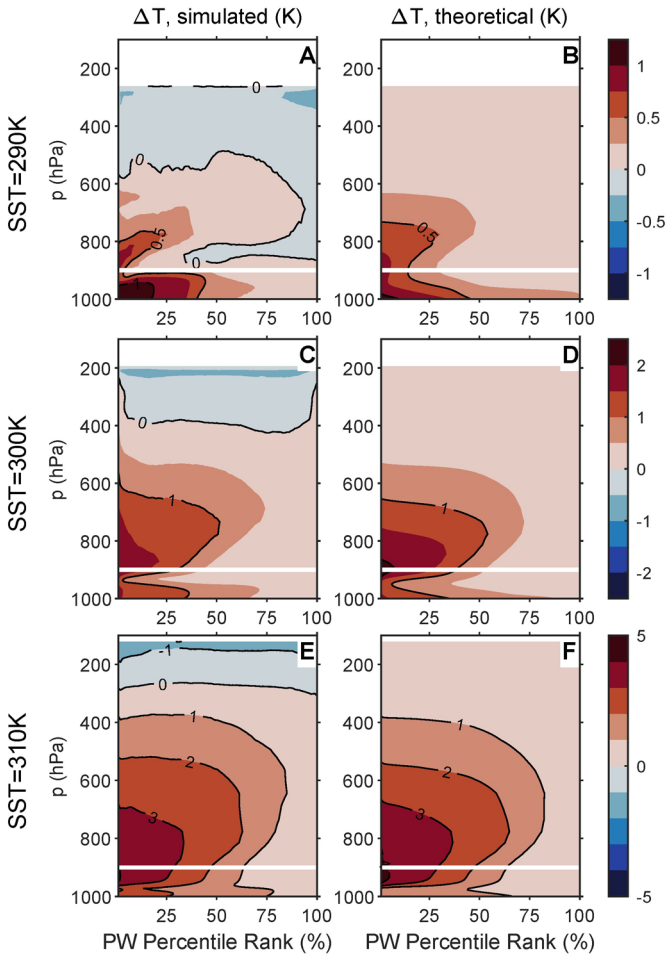


**Figure 2.6**. **Temperature difference due to vapor buoyancy. (A, C, E)** $\Delta T$ is the additional temperature due to the vapor buoyancy effect as calculated by subtracting the temperature profiles of the simulations with and without the vapor buoyancy effect. That is, we subtract the left-hand panels of Fig. 2.3 from the right-hand panels. We do not show values of $\Delta T$ above the tropopause, where WBG no longer applies. **(B, D, F)** $\Delta T$ as calculated from a single simulation using [4]. The white lines denote the 900 hPa level we use for the boundary layer top. We do not show values of $\Delta T$ above the tropopause, where WBG no longer applies.

climate but quickly becomes much smaller relative to the free-troposphere component with climate warming. We do not consider this to be part of the radiative effect of vapor buoyancy, as WBG dynamics do not apply in the stratosphere. This simplification will not affect the overall estimate of the feedback parameter because the increasing trend of the radiative effect is dominated by the free troposphere component. The vapor buoyancy feedback is mainly a free-troposphere feedback process. The nonlinear term is the residual of the linear decomposition. The smallness of that residual supports the approximate linearity of the problem, which is necessary for the radiative kernel analysis.

### 2.3.5 Estimating the radiative effect from a single atmosphere

So far, we have estimated the radiative effect of vapor buoyancy by simulating two different atmospheres: the control atmosphere (with vapor buoyancy) and the mechanism-denial atmosphere (without vapor buoyancy). Now we will develop another method to estimate $\Delta T$ and its associated radiative effect from *only* the control atmosphere. This approach will demonstrate that the simulated effect arises due to the robust physics we propose, as opposed to model details. This new calculation of $\Delta T$ will also show how to estimate the radiative effect of vapor buoyancy using either observations or comprehensive climate models.

According to WBG, we assume that the buoyancy of any air parcel is set by convective plumes with RH = 100%. The temperature difference $\Delta T$ due to vapor buoyancy is calculated as the difference between the temperature of the observed or simulated atmosphere and the temperature of convective plumes with equal density:

$$T_m\left(\frac{1+{r_m^*}/{\epsilon}}{1+r_m^*}\right) = T\left(\frac{1+{r}/{\epsilon}}{1+r}\right), \qquad [3]$$

where $T$ is the observed temperature of the dry parcel, $r$ is the observed water vapor mixing ratio (kg/kg), $T_m = T - \Delta T$ is the temperature of the convective plume, and $r_m^* = r_m^*(T_m, p)$ is the saturation mixing ratio of the moist parcel. We rearrange [3] using the relationship $T_m = T - \Delta T$:

$$\Delta T = T\left(\frac{1+{r_m^*(T_m,p)}/{\epsilon}}{1+r_m^*(T_m,p)} - \frac{1+{r}/{\epsilon}}{1+r}\right)\left(\frac{1+r_m^*(T_m,p)}{1+{r_m^*(T_m,p)}/{\epsilon}}\right) \qquad [4]$$

We have chosen this precise form of $\Delta T$, without approximations, as analytical tractability is unnecessary here. On the right-hand side, the values of *T* and *r* are both known. These are the properties of the observed or simulated air parcel. However, $r_m^*$ is a function of $T_m$, and therefore a function of $\Delta T$. $\Delta T$ cannot be readily isolated to one side of the equation without further approximation. Therefore, we solve

[4] iteratively. We use the Newton-Raphson method, with the derivative approximated numerically, ending the iteration when the correction is less than $10^{-3}$ K.

The right column in Fig. 2.6 shows this theoretical calculation of $\Delta T$, applying [4] to the control simulation data. In the lower troposphere, the magnitude and structure of $\Delta T$ are both remarkably similar between the two methods, indicating that [4] appropriately captures the warming due to the vapor buoyancy effect. This correspondence breaks down near the tropopause: the simulation results show that the atmosphere is slightly cooler with vapor buoyancy. This difference has little impact on the radiative effect calculation, as we show below.

We calculate the radiative effect of vapor buoyancy by applying the temperature radiative kernels to the theoretical calculation of $\Delta T$ for each simulation with vapor buoyancy. As before, we only use data from the free troposphere. Figure 2.5C shows the results of this new, theoretical calculation of the radiative effect of vapor buoyancy alongside the previous calculation. The simulation-pair marks in Fig. 2.5C are simply a reproduction of the free-troposphere-temperature component in Fig. 2.5B. The results show that the radiative effect exponentially increases with SST, which is likely because $\Delta T$ increases with SST exponentially (D. Yang & Seidel, 2020). The two fitted curves correspond well in both magnitude and trend. Thus, the temperature and vapor profiles of a single, with-vapor-buoyancy atmosphere are sufficient to estimate the strength of the radiative effect of vapor buoyancy.

### 2.3.6 The feedback parameter

Finally, it is useful to calculate a feedback parameter – the amount by which the radiative effect increases per unit surface warming. We define the feedback parameter as:

$$\lambda_t = \frac{d\mathrm{R_{vb}}}{d\mathrm{SST}}, \qquad [5]$$

where $R_{vb}$ is the radiative effect of vapor buoyancy. $\lambda_t$ measures the total sensitivity of the radiative effect of vapor buoyancy to SST. $\lambda_t$ results from a combination of changes with climate warming in both $\Delta T$ and

the atmosphere's base state (water vapor and temperature profiles). Yang and Seidel (D. Yang & Seidel, 2020) calculated $\lambda_{vb}$, which isolates only the change in $R_{vb}$ due to the change in $\Delta T$, and found it has a similar magnitude as $\lambda_t$. Figure 2.5D shows $\lambda_t$ based on the fitted exponential curves in Fig. 2.5C. In the Earth-like reference climate, we estimate $\lambda_t$ to be 0.16 and 0.13 W/m$^2$/K for the simulation-pair and theoretical calculations of $\Delta T$, respectively. Following our assumption of an exponential trend in $R_{vb}$, $\lambda_t$ also increases exponentially with climate warming, achieving a magnitude of about 1.5 W/m$^2$/K at 320 K. This is comparable to the atmospheric Planck feedback, a leading-order longwave feedback that results from a uniform warming of the atmosphere, which attains a magnitude of is about 4.6 W/m$^2$/K at that temperature (with fixed specific humidity). The vapor buoyancy feedback reaches 1/3 of the magnitude of the Planck feedback at a 320 K surface temperature. In such warm climates, the vapor buoyancy feedback may be of primary importance for climate stability of the Earth and other terrestrial planets. These climates are much more stable than what has been recognized in past studies that ignored the vapor buoyancy effect (Kopparapu et al., 2013; Pierrehumbert, 1995).

## 2.4 Discussion

This paper tests the hypothesis that the vapor buoyancy effect stabilizes Earth's climate in the tropics. Using 2D CRM simulations, we have demonstrated that the radiative effect of vapor buoyancy is approximately 1 W/m$^2$ in the reference climate, a value comparable to the direct radiative forcing due to doubling atmospheric $CO_2$. More importantly, our calculations suggest that this radiative effect exponentially increases with climate warming. This effect results in a negative feedback of around 0.15 W/m$^2$/K in the reference climate, which is of the same order of magnitude as the net cloud feedback and surface albedo feedback (Boucher et al., 2013; Flato et al., 2013).

Contemporary cloud-resolving and general circulation models have the physics necessary to simulate the vapor buoyancy feedback. Therefore, the feedback should be reflected in past model-based assessments of climate sensitivity. However, simulation does not entail understanding. This study explains how the vapor

buoyancy feedback occurs and presents evidence that it helps to shape Earth's tropical climate. Other authors have aggregated all greater-than-surface warming of the troposphere together into a single "lapse rate feedback" (Flato et al., 2013; Soden & Held, 2006). Such a combined approach may not be appropriate. The origin and amplitude of the vapor buoyancy feedback depend on the *horizontal* distributions of temperature and moisture. Understanding the vapor buoyancy feedback, therefore, requires at least two columns or even two dimensions. This is fundamentally different from the conventional explanation of the tropical lapse rate feedback based on a single column process – the temperature profile (the moist adiabat) is steepening from additional latent heating with warming.

Single-column models are widely used to simulate clouds and climate both on the Earth and on other planets (Kopparapu et al., 2013). These models simulate a representative atmospheric column, usually in a radiative-convective equilibrium state. Such a model is not able to represent the vapor buoyancy feedback, which requires at least two columns and would underestimate climate stability. This deficiency reinforces past arguments in favor of using two-column models, which represent the two branches of an overturning circulation (Pierrehumbert, 1995; J. Yang & Abbot, 2014). In such a model, the column processes, such as convection, may be either parameterized or explicitly simulated. However, the effects of large-scale dynamics are always parameterized, often by imposing a weak horizontal temperature gradient: the two columns have equal temperatures (Schneider et al., 2019; J. Yang & Abbot, 2014). Such an assumption precludes the vapor buoyancy feedback. By excluding the vapor buoyancy effect, these modeling frameworks have considerable biases in estimating atmospheric buoyancy, cloud fraction, radiative feedbacks and thereby climate stability. Therefore, it is desirable to properly represent the vapor buoyancy effect when using the column modeling approach.

The vapor buoyancy feedback requires that the atmosphere is organized into large-scale overturning circulations and that there is abundant water vapor. These criteria are best met in Earth's tropics. The strength of this feedback is determined by the magnitude of water vapor differences across the tropics and the relative size of the dry, subsiding regions of the atmosphere. We refer the reader to Bretherton, et al.

(Bretherton et al., 2004), whose Fig. 2.3B depicts that not only are there very large water vapor differences within the tropics, but also a broad dry region to emit OLR. Therefore, the vapor buoyancy feedback may play a profound role in stabilizing Earth's tropical climate at present. We expect it plays an even greater role in explaining Earth's past climates. A recent review of paleoclimate data and simulations of the hot Eocene climate has suggested surface temperatures as high as 310 K in the tropics (Pagani et al., 2013). Though considerably warmer than our present climate, such a temperature still reflects greater stability in tropical climate than in extratropical climate. Referring to our Fig. 2.5D, such surface temperatures would imply a much stronger vapor buoyancy feedback than at present (about 0.5 $W/m^2/K$). Therefore, the vapor buoyancy feedback may have played a leading role in stabilizing tropical climates in the past.

The vapor buoyancy feedback may also stabilize (or destabilize) planetary climates. Several characteristics of a planet may alter the vapor buoyancy feedback:

1. **The planetary rotation rate.** Many planets rotate more slowly than Earth. Recent work has considered the habitability of tidally locked extrasolar planets with persistent day and night hemispheres. With an orbital period in the tens of Earth days, atmospheric dynamics on such planets would resemble those of Earth's tropics. Rather than altering the meridional temperature gradient, a negative vapor buoyancy feedback on such a planet would effectively expand the inner edge of the habitable zone – the set of orbits where liquid water can exist near the surface.
2. **The ratio of the molar mass of vapor to that of dry air ($\varepsilon$).** In planetary atmospheres, the molecular weights of dry air and vapor may be strikingly different from Earth's. The vapor buoyancy effect would be much stronger for water vapor in a carbon dioxide atmosphere. On the other hand, where water vapor is found in a hydrogen atmosphere, the vapor buoyancy effect would be reversed. Then, the proposed vapor buoyancy feedback would also work in reverse, yielding a positive, destabilizing climate feedback.

3. **The surface temperature.** The feedback strength is remarkably sensitive to surface temperature. It is likely that there are warm terrestrial planets close to the inner edge of their habitable zones. On such planets, the vapor buoyancy feedback more effectively stabilizes the climate than on Earth.

This study uses a 2D CRM with uniform SST. In the 2D CRM simulations, gravity waves, WBG, and water vapor distributions are explicitly simulated, which makes this study a meaningful advance beyond Yang and Seidel (D. Yang & Seidel, 2020). However, there are several limitations due to the idealized approach presented in this paper. For example, the overturning circulations simulated are due to self-aggregation rather than surface temperature gradients as in Earth's Hadley and Walker circulations. There may be departures from the temperature and water vapor profiles actually observed in the tropics. Therefore, it would be desirable to quantify the vapor buoyancy feedback using comprehensive 3D climate models and observations in future studies. In addition, we have mainly discussed the clear-sky radiative effect in this study. It is also desirable to understand and quantify the cloud effect associated with vapor buoyancy.

## 2.5 Appendix: Radiative Kernels

Figure 2.7 presents the radiative kernel calculations discussed in the Methods section. The first two columns represent the kernels as actually applied in this study. The third column is what the water vapor kernel looks like under an assumption of constant relative humidity with climate warming. We do not apply that assumption, and we present this kernel only for comparison to past work on radiative kernels.

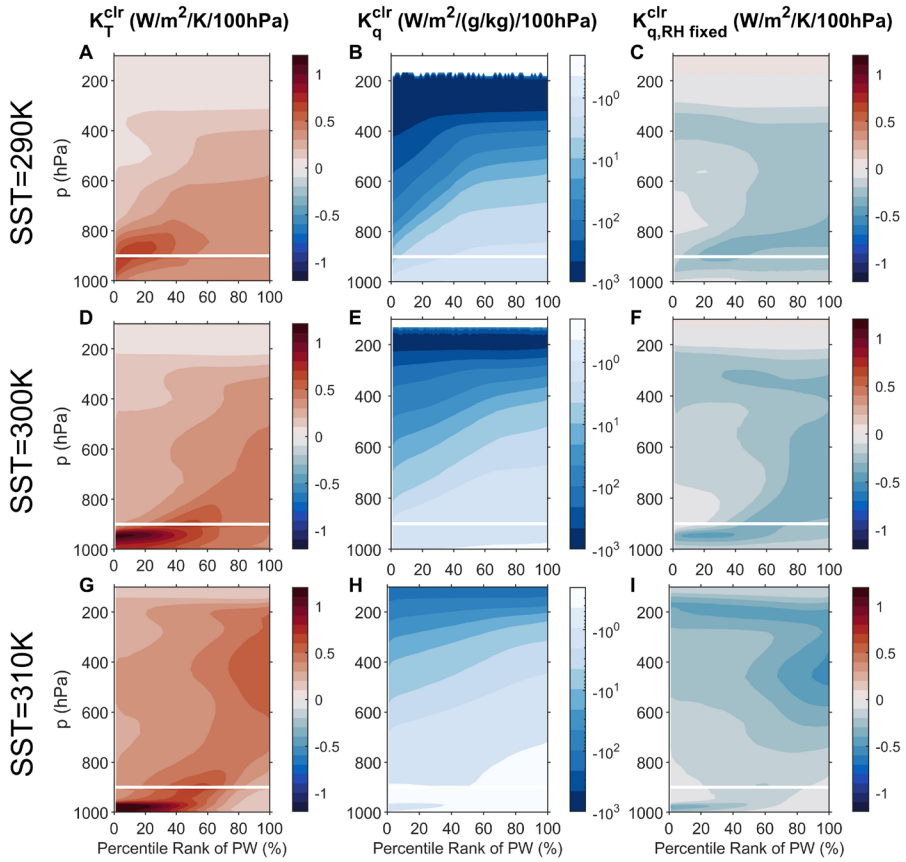


**Figure 2.7. Radiative kernels. (A, D, G)** The temperature radiative kernel, which reflects the sensitivity of clear-sky OLR to changes in atmospheric temperature. **(B, E, H)** The specific humidity radiative kernel, which reflects the sensitivity of clear-sky OLR to changes in atmospheric water vapor. We do not show values where they become positive in the stratosphere. **(C, F, I)** The specific humidity radiative kernel applied to increased water vapor from warming at constant-relative humidity. The white lines denote the 900 hPa level we use for the boundary layer top.

# 3 Vapor-Buoyancy Feedback in an Idealized General Circulation Model

**Abstract**

Humid air is lighter than dry air at the same temperature and pressure because the molecular weight of water vapor is less than that of dry air. This effect is known as vapor buoyancy (VB). In this work we use experiments in an idealized general circulation model (GCM) to show that VB warms the tropical free troposphere and leads to a significant increase in outgoing longwave radiation (OLR). This radiative effect increases with climate warming, causing a negative climate feedback there. We call this the VB feedback. Although this VB feedback was first corroborated in simplified models, it was heretofore unclear whether the VB feedback is significantly impaired by planetary rotation, clouds, or a countervailing water vapor feedback. However, our GCM simulations show that the VB feedback is robust and maintains an appreciable magnitude when considering these factors.

## 3.1 Introduction

The previous chapter demonstrated the VB feedback mechanism when convection is explicitly resolved. However, that experiment had several limitations. First, the CRM lacked planetary rotation, which left it unclear whether the VB feedback would occur where the WBG assumption is only approximate, as strict WBG requires negligible planetary rotation. That would confine the VB feedback to a narrow equatorial band, rendering it unimportant in the global energy balance. Second, the CRM relied on the self-organizing nature of convection to give rise to a tropical circulation, whereas a realistic Hadley Circulation may have a different water vapor budget and thereby a distinct moisture distribution. This left it unclear whether the negative VB feedback would be accompanied by a countervailing positive component of water vapor feedback, as might be expected with increasing atmospheric temperature (Isaac M. Held & Shell, 2012; Jeevanjee et al., 2021). It was also unclear whether there would be a compensating (positive) or reinforcing (negative) cloud feedback due to vapor buoyancy.

The present study will address these unanswered questions regarding the VB feedback. We shall use simulations in a general circulation model to ask whether rotation or changes in dry-region water vapor significantly affect the VB feedback. The methods employed in this chapter are very similar to those in the previous chapter, as the focus is on whether the VB feedback persists with the switch to a GCM. The parameterized nature of GCM convection also allows us to narrowly target the role of atmospheric dynamics in the VB feedback, as it is possible to remove VB from the dynamical calculations but not the convection parameterizations.

## 3.2 Simulation Design

To test whether the VB feedback occurs in an atmosphere with planetary rotation, we rely on aquaplanet simulations in the Community Atmosphere Model, version 6 (CAM6) (G. Danabasoglu et al., 2020). To calculate radiative fluxes and tendencies, CAM6 employs the Rapid Radiative Transfer Model for GCMs (RRTMG, Mlawer et al. 1997). The model is run with fixed $CO_2$ concentration of 348 ppmv. Shallow convection is parameterized using the Cloud Layers Unified By Binormals (CLUBB) scheme, and deep convection is parameterized using the Zhang-McFarlane scheme (Bogenschutz et al., 2013; Zhang & McFarlane, 1995). The surface temperature is the same as that used in the GCM simulations reported by Yang et al. (2022). The model is run at an approximately 2-degree horizontal resolution.

In order to test the role of VB, we perform three simulations at each surface temperature: (1) CNTL, an unmodified version of the model; (2) MD-DYN, in which VB is removed from the model's dynamics but not its moist parameterizations; and (3) MD-ALL, in which VB is removed from the dynamics as well as the boundary-layer and convection schemes. The MD-DYN experiment is intended to isolate only the physics of the VB feedback, as well as to emulate several climate models who exclude VB from their

pressure gradient calculation, but not their moist parameterizations.[1] The MD-ALL simulation is intended to test whether the VB feedback is active compared to a more physically consistent counterfactual. The MD-DYN and MD-ALL experiments correspond to the MD1 and MD2 experiments in Yang et al. (2022); however, we use a different model here.

## 3.3 Results

### 3.3.1 Hotter atmosphere due to VB

In this section, we want to ask: Is the atmosphere hotter due to VB in an environment with appreciable planetary rotation? Here we are concerned with the difference in temperature $\Delta T$ due to VB:

$$\Delta T_{MD-DYN} = T_{CNTL} - T_{MD-DYN}, \tag{1}$$

$$\Delta T_{MD-ALL} = T_{CNTL} - T_{MD-ALL}, \tag{2}$$

where $T_{VB}$ is the temperature of the atmosphere in the control simulation, and $T_{MD}$ is the temperature in a mechanism-denial simulation. Figs. 3.1a and 3.1b show $\Delta T_{MD-DYN}$ fand $\Delta T_{MD-ALL}$ , respectively, at the control surface temperature (300 K at the equator). The subtropical middle troposphere is up to 1 K warmer in the CNTL simulation than the MD-DYN simulation and up to 2.5 K warmer in the CNTL simulation than in the MD-ALL simulation. Figs. 3.1d and 3.1e show $\Delta T_{sim}$ when the surface temperature is 4 K greater. $\Delta T_{sim}$ increases with climate warming.

To test whether the warmer atmosphere depicted in Fig. 3.1 is explained by VB, we develop a simple analytic expression for $\Delta T$. We begin with a precise expression for virtual temperature:

$$T_v = T(1 + \nu q) \tag{3}$$

[1] Our design of the MD-DYN experiment is simply to zero out the virtual temperature parameter (*zvir*) which is used in the dynamical core. This affects not only the dynamical core, but also the rest of the model except for the convection and PBL schemes. Notably, this includes surface flux calculations. However, our testing showed these made little difference in the results presented here.

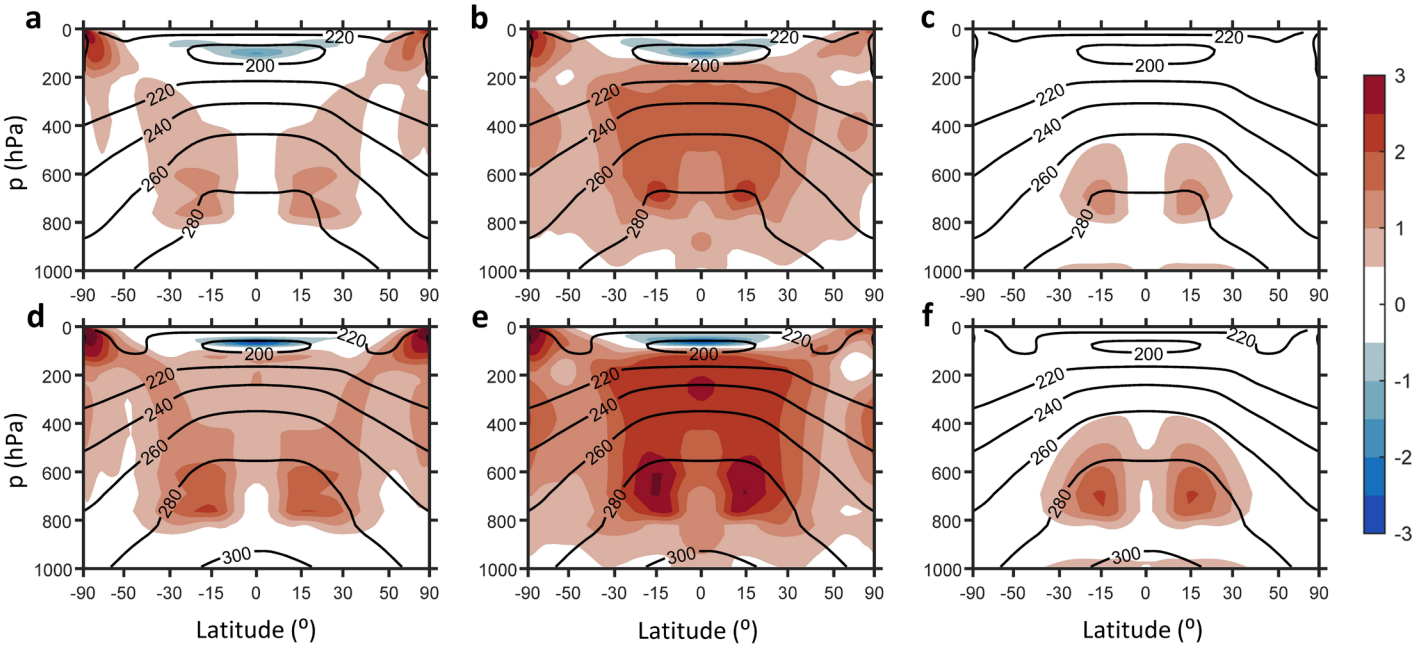


**Figure 3.1.** Temperature difference due to VB. (a) $\Delta T_{MD-DYN}$ for an equatorial surface temperature of 300 K. (b) $\Delta T_{MD-ALL}$ for an equatorial surface temperature for 300 K. (c) $\Delta T_{theory}$ for an equatorial surface temperature of 300 K. (d) $\Delta T_{MD-DYN}$ for an equatorial surface temperature of 306 K. (e) $\Delta T_{MD-ALL}$ for an equatorial surface temperature of 306 K. (f) $\Delta T_{theory}$ for an equatorial surface temperature of 306 K.

where $T$ is temperature, $q$ is specific humidity, and $\nu = \frac{M_d}{M_v} - 1 \approx 0.61$ is the virtual parameter. $M_v$ and $M_d$ are the molar masses of water vapor and dry air, respectively. Since density is approximately horizontally homogeneous in the tropical free troposphere (Charney, 1963; Sobel et al., 2002), we equate the virtual temperature of a parcel of saturated air ($T_{v,sat}$) and the virtual temperature of air in the simulated or observed atmosphere ($T_v$):

$$T_v = T_{v,sat}. \tag{4}$$

Substituting the definition of virtual temperature:

$$T(1 + \nu q) = T_{sat}\left(1 + \nu q^*(T_{sat})\right). \tag{5}$$

We define $\Delta T = T - T_{sat}$ as the temperature difference due to VB. We further linearize $q^*$ around T using the Clausius Clapeyron relation $\partial_T q^* = \frac{Lq^*}{R_v T^2}$, where L is the latent heat of vaporization of water vapor, and $R_v$ is the gas constant of water vapor. Substituting $T_{sat} = T - \Delta T$ into Eq. 5 and expanding around $\Delta T$:

$$T(1 + \nu q) = T(1 + \nu q^*) - \Delta T\left(1 + \nu q^*(T) + \nu \frac{L}{R_v T} q^*(T)\right) + \Delta T^2 \nu \frac{L}{R_v T^2} q^*(T). \quad (6)$$

We note that $\nu q^*(T) \ll 1$ and exclude that term. We also exclude the higher order ($\Delta T^2$) term and then reorganize:

$$\Delta T_{theory} = \frac{\nu T(q^*(T) - q)}{1 + \nu\left(\frac{L}{R_v T}\right) q^*(T)}. \quad (7)$$

Unlike the similar expression derived in Chapter 2, which required iterations to solve, this expression is analytical. Figs. 3.1c and 3.1f show $\Delta T_{theory}$ calculated from the control simulation. In the middle troposphere, $\Delta T_{theory}$ is a close match to $\Delta T_{MD-DYN}$ (Figs. 3.1a and 3.1d), but substantially underestimates $\Delta T_{MD-ALL}$. This is because $\Delta T_{theory}$ captures the warming due to VB's interaction with the large-scale dynamics, but it does not account for differences due to boundary-layer turbulence or convection. For greater clarity, Fig. 3.2 compares $\Delta T_{MD-DYN}$, $\Delta T_{MD-ALL}$, and $\Delta T_{theory}$ at the 691 hPa model level. $\Delta T_{theory}$ closely approximates $\Delta T_{MD-DYN}$, particularly in the tropics (± 30º).

Fig. 3.2 shows that $\Delta T_{theory}$ captures the gross features and scale of the meridional pattern of $\Delta T_{MD-ALL}$ within the tropics. However, in both Fig. 3.1 and Fig. 3.2, it is apparent that $\Delta T_{MD-ALL}$ is considerably greater than $\Delta T_{MD-DYN}$. This may be due to differences in temperature and water vapor in the equatorial boundary layer. Figure 3.3a shows moist static energy is greater in CNTL than in MD-ALL between 800 hPa and the surface. According to the convective quasi-equilibrium hypothesis, upon which the Zhang- McFarlane convection scheme is formulated, we expect that the more energetic CNTL boundary

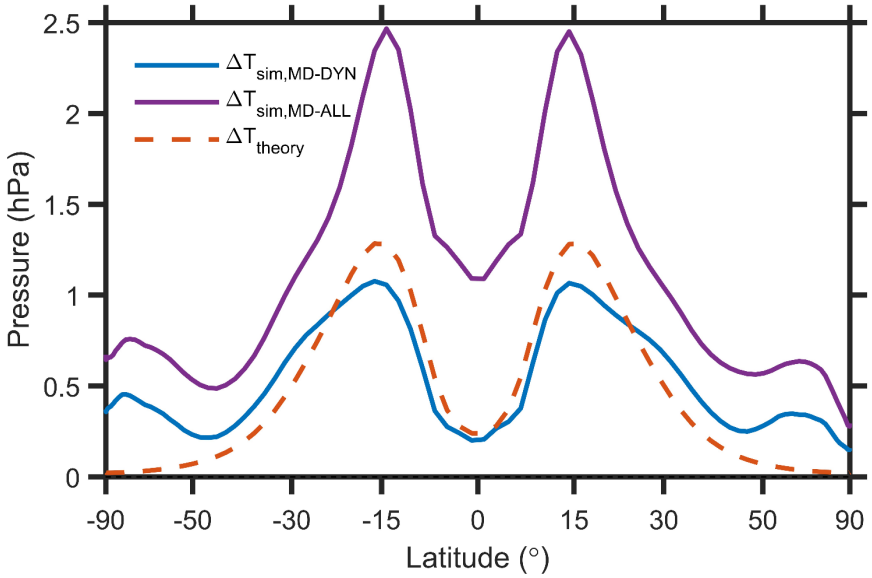


**Figure 3.2.** Temperature difference due to VB at the 691 hPa model level.

layer would lead to a greater equilibrium temperature in the free troposphere (EMANUEL et al., 1994; Zhang & McFarlane, 1995). Then, those free-troposphere temperature differences would be communicated to the rest of the tropics via weak-buoyancy-gradient dynamics. We support the first portion of this hypothesis by calculating a moist adiabatic temperature profile. Using the analytical theory provided by Romps (2017), we first calculate the lifting condensation level for an equator-average (±5°) parcel lifted from 913 hPa model level. Then we calculate the moist adiabat from that lifting condensation level.

The horizontal axis of Fig. 3.3b shows the calculated moist-adiabatic temperature $T_{ma}$ for each model level between 300 and 800 hPa in the same ±5° latitude band. The vertical axis is the actual simulated temperature at that level. Filled circles denote the CNTL simulation, and open circles denote MD-ALL. Overall, $T_{ma}$ is a strong predictor of $T$, as the marks are parallel to the one-to-one line. More importantly, a difference in $T_{ma}$ between CNTL and MD-ALL is generally matched by an approximately equal difference in $T$. This suggests that differences in boundary-layer moist static energy are responsible for the large values of $\Delta T_{MD-ALL}$ at the equator, which are then communicated to the subtropics via large-scale dynamics. However, in the next section we show that the large difference between $\Delta T_{MD-DYN}$ and $\Delta T_{MD-ALL}$ does not lead to large differences in the clear-sky longwave feedback.

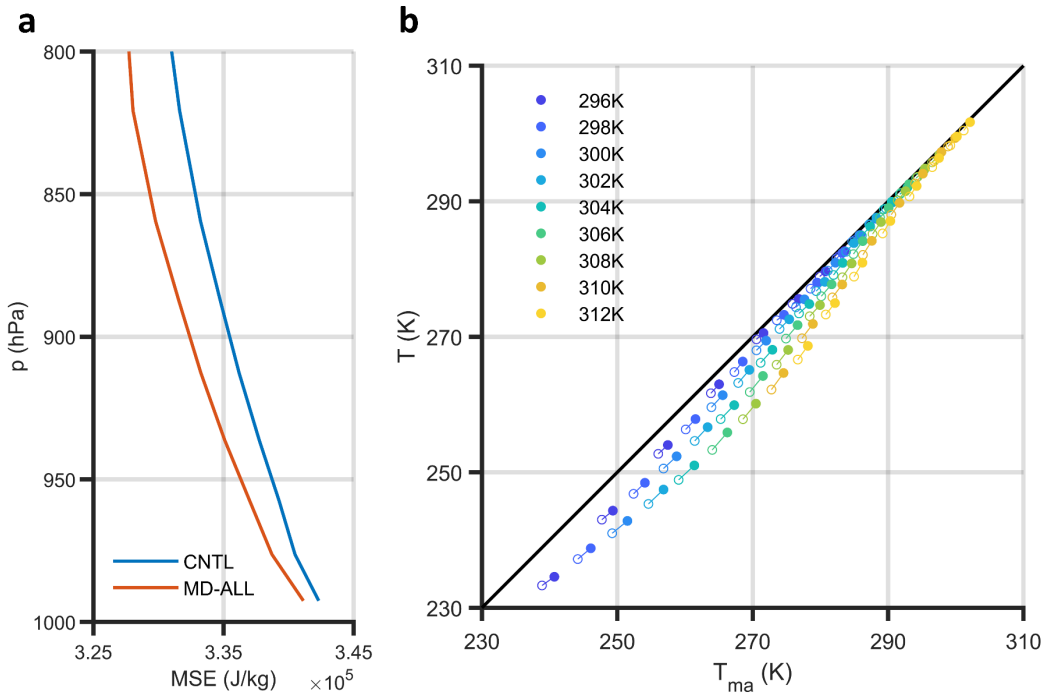


**Figure 3.3.** (a) Equatorial region (±5°) moist static energy for the CNTL and MD-ALL simulations with an equatorial surface temperature of 300 K. (b) Equatorial region (±5°) free-troposphere temperature as predicted by moist-adiabatic ascent from the equatorial boundary layer (horizontal axis) plotted against the simulated difference in temperature. Filled circles denote data from the CNTL simulation, and open circles denote MD-ALL.

Even in a model with appreciable planetary rotation, VB warms the atmosphere by the amount we would expect in theory. This suggests that the vapor-buoyancy feedback is active in the real-world subtropics. We shall evaluate the simulated feedback in the next subsection.

### 3.3.2 Clear-sky VB feedback

Here we investigate the differences in simulated clear-sky outgoing longwave radiation ($\Delta OLR_{clr}$). The yellow marks in Fig. 3.4a show tropical-average (± 30° latitude) $\Delta OLR_{clr}$. One may think of this as the total radiative effect of vapor buoyancy. $\Delta OLR_{clr}$ increases as the climate warms, suggesting that the vapor-buoyancy feedback is active there.

We can attribute $\Delta OLR_{clr}$ to simulated differences in tropospheric temperature and specific humidity, as we will show the stratospheric effects are small. To do so, we use clear-sky approximate radiative kernels, which are linear response functions of top-of-atmosphere radiation to perturbations in temperature and

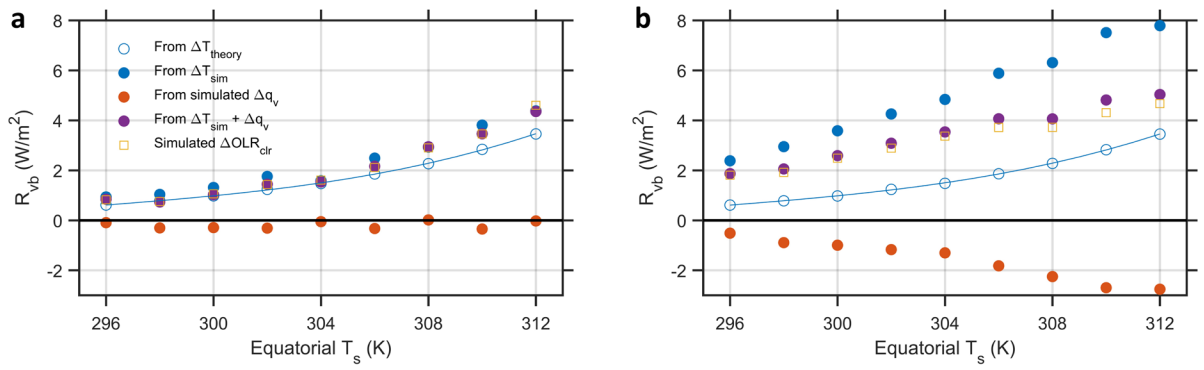


**Figure 3.4.** Difference in net clear-sky radiation at top of atmosphere for (a) the MD-DYN experiment and (b) the MD-ALL experiment. Closed blue circles indicate the radiative effect implied by $\Delta T_{vb}$ as simulated by either experiment. Open blue circles indicate the radiative effect implied by $\Delta T_{THEORY}$. The red circles indicate the radiative effect implied by differences in specific humidity between the CNTL and MD simulations. The violet circles indicate the sum of the temperature and specific humidity effects. The yellow squares indicate the simulated difference in clear-sky OLR. The blue curve indicates a cubic fit to the open circles.

humidity. The kernels are described in Appendix B. We take the inner products of the temperature and humidity kernels with the thermodynamic perturbations $\Delta T_{MD-DYN}$ and $\Delta q_{MD-ALL}$, using the lapse-rate tropopause[2] as the upper limit for the integral. The solid blue circles in Fig. 3.4a show the differences in $\Delta OLR_{clr}$ due to tropospheric $\Delta T_{MD-DYN}$, whereas the red circles show the differences due to tropospheric $\Delta q_{MD-DYN}$. The violet circles show the sum of these two radiative effects, and they closely approximate $\Delta OLR_{clr}$, suggesting that stratospheric effects are negligible. Finally, the open blue circles indicate the temperature radiative effect using $\Delta T_{theory}$.

We can draw two inferences from Fig. 3.4a. First, VB is responsible for a robust negative feedback as shown by the trend in $\Delta OLR_{clr}$ and that this trend can be explained well by $\Delta T_{theory}$. Second, there is essentially no countervailing change in the water vapor feedback due to VB, as is seen by the fact that tropospheric water vapor does not contribute to the trend in $\Delta OLR_{clr}$. To supplement this result, Appendix A discusses the differences in humidity between CNTL and MD-DYN.

[2] We use a lapse-rate threshold of 2 K/km to define the tropopause, as in Zelinka et al. (2020)
.

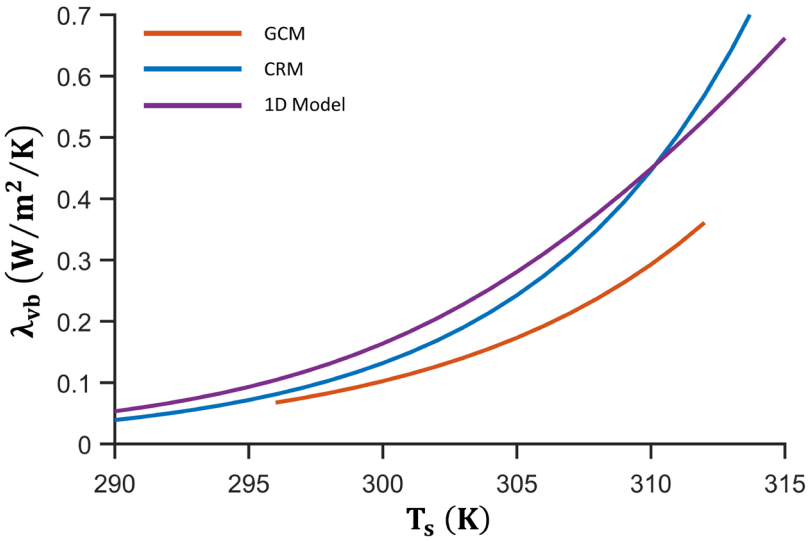


**Figure 3.5.** Tropical-average VB feedback derived from a hierarchy of climate models. The CRM result is reported in Seidel and Yang (2020).

Figure 3.4b is the same as Fig. 3.4a but for the MD-ALL experiment. In this experiment, there *is* an additional positive water vapor feedback due to VB, indicated by the negative trend of the red marks with climate warming. However, this is offset by a greater negative feedback due to $\Delta T_{MD-ALL}$. The sum of the temperature and water vapor radiative effects in the MD-ALL experiment indicate a negative VB feedback similar to that in MD-DYN and to the vapor-buoyancy feedback implied by $\Delta T_{theory}$. The combined temperature and water vapor feedbacks in MD-ALL can be linearly estimated as 0.20 W/m$^2$/K over the whole temperature range, compared to 0.22 W/m$^2$/K for MD-DYN. The MD-DYN and MD-ALL experiments show very similar clear-sky feedbacks. This may be understood by considering that the additional VB-induced warming shown in the MD-ALL experiment (compared to MD-DYN) occurs in convective plumes and communicated to the rest of the tropical atmosphere from there by the large-scale dynamics. The free troposphere's source of water vapor (convection) is warming, so the atmosphere will also be wetter if RH is approximately fixed. This causes a countervailing water vapor feedback which balances the additional temperature feedback in MD-ALL.

The magnitude of a climate feedback is measured by its feedback parameter, which represents a top-of-atmosphere flux sensitivity to a unit increase of surface temperature. We fit a cubic curve to the $\Delta T_{theory}$

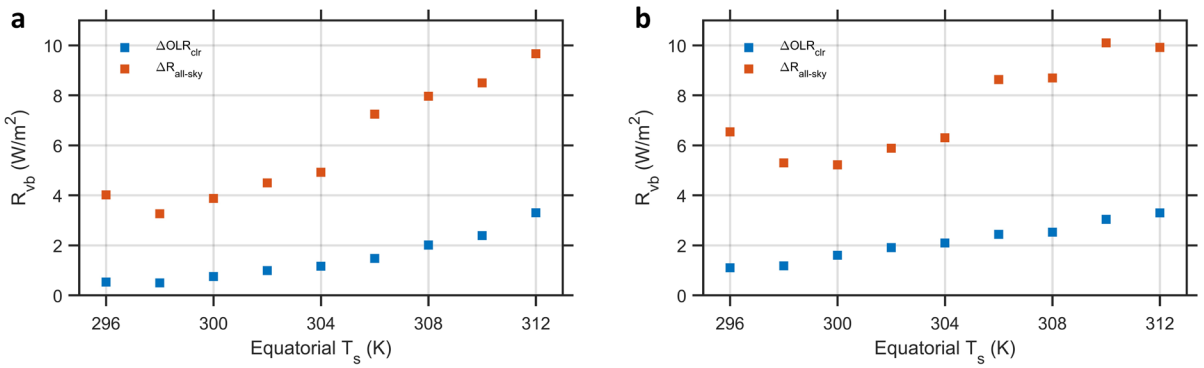


**Figure 3.6.** Difference in net all-sky radiation at top of atmosphere for (a) the MD-DYN experiment and (b) the MD-ALL experiment (red squares). $\Delta OLR_{clr}$ is shown for comparison.

marks in Fig. 3.4 and take its derivative. This gives us the feedback parameter represented by the red curve in Fig. 3.5. Plotted alongside these data, the blue curve represents the feedback parameter as estimated by a curve fit in the SY20 CRM experiment. The purple curve shows an estimate from a simple 1D column model which shall be described in Chapter 4. These curves represent a hierarchy of models for the VB feedback: a 3D GCM, a 2D CRM, and 1D column model. The three models broadly agree upon the magnitude of the VB feedback and its trend with warming, thus corroborating one another.

### 3.3.3 All-sky and global-average feedbacks due to VB

Our analysis of feedbacks due to VB has so far been limited to clear-sky radiative effects in the tropics. However, it is useful to ask whether VB alters the total climate feedback in a more complete picture: in the global average, with cloud radiative effects included. Figures 7a and 7b show the globally averaged differences in top-of-atmosphere all-sky radiation between CNTL and MD-DYN and CNTL and MD-ALL, respectively. As in the previous sections, we adopt a sign convention that upwelling fluxes are positive so that a positive trend indicates a *negative* climate feedback. For MD-DYN compared to CNTL, the all-skyradiative effect is greater than the clear-sky radiative effect by 4 to 6 W/m$^2$. We can roughly estimate the feedback magnitude as 0.35 W/m$^2$/K as the slope from the coldest ($T_{eq} = 296\,K$, $\Delta R_{all} = 4.0\,W/m^2/K$) to the warmest ($T_{eq} = 312\,K$, $\Delta R_{all} = 5.6\,W/m^2/K$) surface temperatures. This is greater than a comparable clear-sky longwave estimate of 0.17 W/m$^2$/K. That is, cloud radiative effects *add* to the

vapor buoyancy feedback. Calculating feedbacks in the same way for MD-ALL, the total all-sky feedback is 0.21 W/m$^2$/K, compared to 0.14 W/m$^2$/K for clear-sky OLR. The MD-DYN experiment shows a greater difference in cloud feedback than MD-ALL, which may be attributable to MD-DYN's mismatch between its treatment of large-scale dynamics and its treatment of shallow convection and surface fluxes. However, it should be noted again that the MD-DYN experiment is consistent with several GCMs which appear to exclude VB from their dynamics but not their parameterizations (D. Yang et al., 2022). Our simulations suggest that that modeling choices may introduce an artificial positive feedback component to the climate system, which may be averted by including VB in the dynamical calculations.

## 3.4 Discussion

We have used idealized GCM simulations to corroborate a vapor-buoyancy feedback in Earth's tropics. The VB feedback is spatially extensive and robust even when one considers VB's influence on the water vapor feedback. This result was not clear in our earlier study (SY20), which used a cloud resolving model with zero rotation. These results suggest that the VB feedback is physically valid in a warm, wet, rotating atmosphere such as Earth's. Since VB *causes* a difference in clear-sky feedback, the VB feedback is not merely an artifact of unconventional feedback decomposition as suggested by Colman and Soden (2021). Without VB, the mean tropical climate feedback would in fact be less negative. This intuition is important for the development of climate models, as well. Several state-of-the-art GCMs exclude VB from their dynamics and consequently emit less outgoing longwave radiation (D. Yang & Seidel, 2023).

The VB feedback is likely present in the comprehensive climate models which include VB in their pressure gradient calculations. If temperature feedbacks are decomposed under an assumption of constant specific humidity, then the VB feedback would be part of the calculated lapse-rate climate feedback, as it derives from a difference in atmospheric warming relative to surface warming. However, if (temperature-)relative humidity is assumed fixed when calculating feedbacks, as suggested by Held and Shell (2012) and Jeevanjee et al. (2021), the negative VB feedback quantified here would instead be split between a negative

lapse-rate feedback and a negative relative humidity feedback (due to decreasing relative humidity). This difficulty could be rectified by redefining relative humidity with respect to a constant-density saturation rather than a constant-temperature saturation, as discussed in Appendix A. However, that assumption may not be appropriate for the boundary layer. There is no perfect choice of moisture variable for feedback decomposition.

Although we have performed analyses using a wide array of methods and models, future studies may still rectify several knowledge gaps. Further modeling experiments could include continents in order to more realistically simulate VB's influence on cloud feedbacks. It may also be worthwhile to consider the effects of interactive surface temperatures, as the VB feedback's outsize influence in the tropics may reduce the meridional temperature gradient in a warming climate.

## 3.5 Appendix A: Muted changes in humidity due to VB

Figs. 3.7a and 3.7c show $\Delta RH_T$, the difference in relative humidity between CNTL and MD-DYN. The subscript $T$ denotes that this is a conventional relative humidity, calculated with respect to constant-temperature saturation process. The atmosphere is less humid in the CNTL simulations, particularly in the subtropical middle troposphere, where VB causes the greatest warming. This suggests that VB dries the atmosphere. Furthermore, it appears that the magnitude of $\Delta RH_T$ increases with warming. This is inconvenient for understanding climate feedbacks, as $RH_T$ is often used as the state variable (held fixed) for evaluating temperature-based climate feedbacks (Isaac M. Held & Shell, 2012; Zelinka et al., 2020).

For this reason, it is helpful to explore an alternative notion of relative humidity. We define density-relative humidity as the concentration of water vapor in a parcel of air ($q$) compared to the concentration which would be achieved in a constant-density saturation ($q^*(T_v, p)$):

$$\mathrm{RH}_\rho = \frac{q}{q^*(T_v, p)}. \tag{8}$$

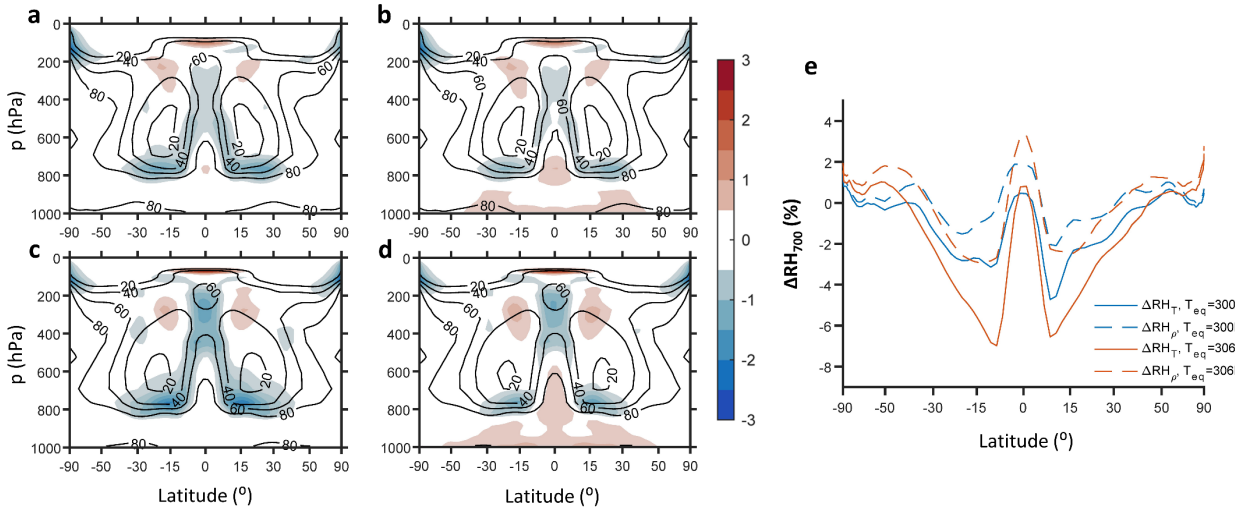


**Figure 3.7.** Difference in zonal-average relative humidity due to VB (color contours); zonal-average CNTL simulation humidity (black contours). (a) $\Delta RH_T$ for an equatorial surface temperature of 300K. (b) $\Delta RH_\rho$ for an equatorial surface temperature of 300K. (d) $\Delta RH_\rho$ for an equatorial surface temperature of 306K. (e) $\Delta RH_T$ and $\Delta RH_\rho$ at 700 hPa.

$RH_\rho$ is a useful measure in the free troposphere if one assumes the cloud-free atmosphere is principally moistened by horizontal motions along isentropes (surfaces of constant virtual potential temperature). Thisalternative notion of humidity is not entirely novel. Romps (2014) developed an analytical model for tropical relative humidity in which RH was defined as the ratio of specific humidity in a subsaturated environment to the specific humidity of a saturated plume at the same density and pressure, which is how we define $RH_\rho$. That model suggested that RH is enhanced by isentropic mixing from moist plumes but reduced by subsidence drying. However, it neglected the lightness of water vapor, so the distinction between $RH_\rho$ and $RH_T$ was not apparent.

In Earth's atmosphere, $RH_\rho$ is necessarily greater than $RH_T$ since adding more water vapor to a parcel under a constant-density process necessitates a lower temperature, and smaller $q^*$. The relationship between $RH_\rho$ and $RH_T$ can be derived from the relationship $q^*(T_v, p) = q^*\left(T - \Delta T_{theory}\right)$. Linearizing $q^*$ around the Clausius-Clapeyron relation $\partial_T q^* = \frac{L}{R_v T^2} q^*$, this gives:

$$RH_\rho = \frac{q}{q^*(T,p) - \frac{L}{R_v T^2} q^*(T,p) \Delta T_{theory}}. \quad (9)$$

This simplifies to:

$$RH_\rho = \frac{RH_T}{1 - \frac{L}{R_v T^2} \Delta T_{theory}}, \quad (10)$$

where $RH_T$ is the conventional (temperature-)relative humidity. The departure between $RH_\rho$ and $RH_T$ grows considerably with warming, owing to its dependence on $\Delta T_{theory}$. For a parcel of air with $RH_T = 50\%$ and a pressure of 800 hPa, $RH_\rho$ increases from 52% at a temperature of 280 K to 57% at a temperature of 300 K.

Figs. 3.7b and 3.7d show $\Delta RH_\rho$ for the MD-DYN experiment at two different surface temperatures. Since $\Delta T_{theory}$ is zero in an atmosphere without VB, $\mathrm{RH_\rho} = \mathrm{RH_T}$ for the mechanism-denial experiments. Comparing to Figs. 3.7a and 3.7d, $\Delta RH_\rho$ shows weaker minimums than $\Delta RH_T$ in the subtropical middle troposphere. In Fig. 3.7e, we compare $\Delta RH_T$ and $\Delta RH_\rho$ at the 691 hPa model level, which tells a similar story: $\Delta RH_\rho$ shows weaker VB-induced drying of the subtropics compared to $\Delta RH_T$, and a compensating wetting of the deep tropics. This suggests an intensification or narrowing of the model's intertropical convergence zone due to VB. Furthermore, $RH_\rho$ is more nearly fixed than $RH_T$ is as the climate warms, especially in the subtropics.

## 3.6 Appendix B. Clear-sky radiative kernels

To decompose perturbations in clear-sky OLR into contributions due to temperature and water vapor, we construct clear-sky radiative kernels, shown in Fig. 3.8. Radiative kernels are linear response functions of top-of-atmosphere radiation to atmospheric properties. We use the approximate kernel technique from Cronin and Wing (2017), calculating the linear response of top-of-atmosphere radiation to small

perturbations in the zonal mean thermodynamic profiles. Our kernels are derived from +0.5 K perturbations in temperature and -1% perturbations in specific humidity from the CNTL simulation zonal average. We calculate a separate radiative kernel for each surface temperature.

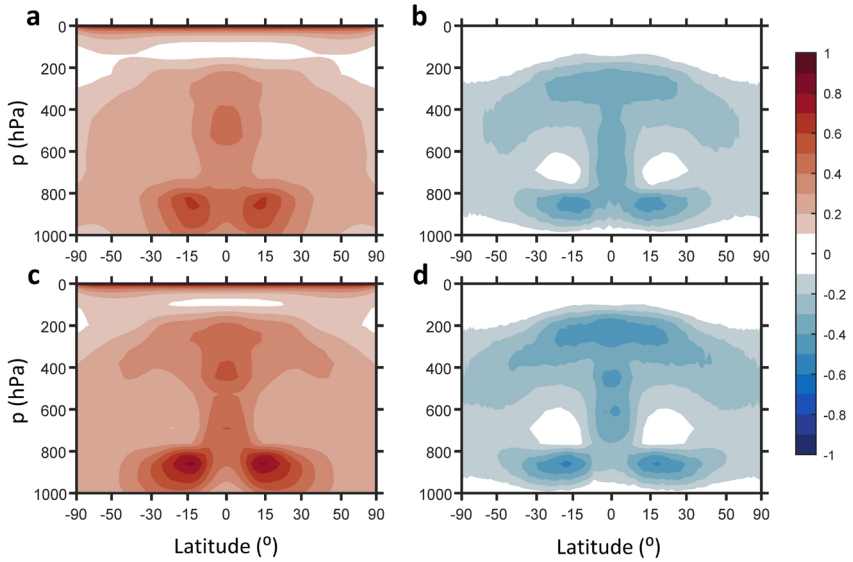


**Figure 3.8.** Radiative kernels (W/m$^2$/K/100 hPa) for (a) temperature and (b) humidity at an equatorial surface temperature of 300K, and for (c) temperature and (d) humidity for an equatorial surface temperature of 306K. The humidity kernels reflect 1K of warming at fixed $RH_T$.

# 4 Clear-Sky Longwave Feedbacks in a 1D Climate Model

**Abstract**

We construct a one-dimensional radiative-convective model and perform feedback analysis with a wide range of humidities and surface temperatures. We compare the VB feedback to other clear-sky longwave feedbacks: the surface Planck feedback, atmospheric Planck feedback, and moist-adiabatic lapse rate feedback. Our results show that the VB feedback is an appreciable non-leading-order climate feedback in the present climate and approaches leading order in hothouse climates characterizing the warmest periods from Earth's past.

## 4.1 Introduction

In this chapter, we implement a 1-D column model of clear-sky longwave feedback mechanisms. This serves several purposes. By adding to the hierarchy of models for the VB feedback, we can corroborate the theoretical explanation given in Chapter 2. Additionally, the simple framework allows us to define and quantify several other clear-sky longwave feedback processes. Finally, we would like to probe the transition to hothouse climate states substantially warmer than the present-day tropics. Such a temperature range requires the use of expensive line-by-line radiation calculations which are more accurate at high temperatures than calculations with a conventional radiation parameterization.

## 4.2 Model Design

We use Pyrads (Koll & Cronin, 2018), a one-dimensional climate model which calculates TOA LW fluxes for a prescribed temperature and moisture profile. It uses line-by-line radiation paired with the MT-CKD continuum model (Mlawer et al., 2012). The model temperature structure, depicted in Fig. 4.1, is similar to that of the 1D model of Yang and Seidel (2020). The atmosphere is comprised of two columns: a saturated plume with moist-adiabatic temperature profile $T_m$, and an unsaturated environment with the same

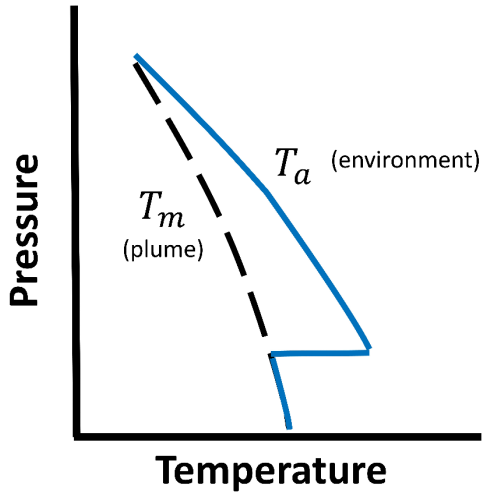


**Figure 4.1.** Schematic illustration of the 1D climate model temperature profile.

virtual temperature as the plume. This requires that the temperature of the dry environment is greater than that of the saturated convective plume by the amount:

$$\Delta T_{VB} = \nu T_m (q^*(T_m) - q) \tag{1}$$

where $q$ is the specific humidity of the unsaturated environment, and $q^*(T_m)$ is the saturation specific humidity of the moist plume. Assuming the cross-sectional area of the plume column is negligible compared to that of the environment, the free-troposphere temperature is then given by:

$$T_a = T_m + \Delta T_{VB} \tag{2}$$

The boundary-layer top is prescribed at 85% of the surface pressure. Below there, VB is assumed not to warm the atmosphere. The partial pressure of dry air is prescribed to be 1000 hPa at the surface, but total column mass (and thus surface pressure) increases with the amount of water vapor. In effect, the boundary-layer top is prescribed to be *near* 850 hPa, but the exact level depends on humidity.

We prescribe the specific humidity as a fixed proportion $\beta$ of that in the saturated plume:

$$q = \beta q^*(T_m) \tag{3}$$

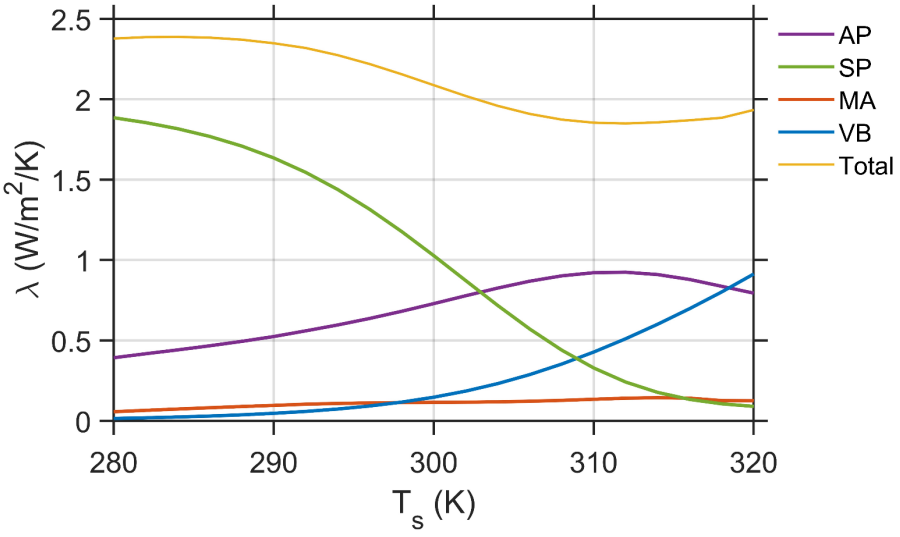


**Figure 4.2.** Clear-sky longwave feedbacks in the 1-D climate model for humidity parameter $\beta = 0.5$.

In the free troposphere, $\beta$ is equivalent to the density-relative humidity $RH_\rho$, or the ratio of specific humidity to its value after a constant-density saturation. In Appendix A we formally define $RH_\rho$ and quantify it in our GCM simulations. Within the boundary layer a fixed $\beta$ implies a fixed (conventional) relative humidity $RH_T$ of the same value since $T = T_m$ there. We prescribe an isothermal stratosphere ($T_{strat} = 200K$) in which specific humidity is fixed at its tropopause value.

We used a fixed $CO_2$ concentration of 348 ppmv, consistent with the aquaplanet simulations reported in the previous section. For the following calculations, we sample a range of surface temperatures and $\beta$ in increments of 2 K and 5% respectively. The radiation calculations use a spectral range of 0.1 to 3500 $cm^{-1}$ with a resolution of 0.01 $cm^{-1}$. We use a vertical grid consisting of 80 pressure levels, with spacing that is approximately linear near the surface and approximately logarithmic near the model top. That choice allows for more finely resolved lower- and middle-troposphere feedbacks but also sufficient resolution so that the amount of upwelling longwave radiation masked by the stratosphere does not become non-monotonic with climate warming.

## 4.3 Results

The yellow line in Figure 4.2 shows the total climate feedback in the model when the value of $\beta$ is fixed at 0.5. This feedback is calculated as the difference in outgoing longwave radiation (OLR) between a reference profile and a perturbation profile calculated with a 1K colder surface temperature, fixing the stratosphere.[3] As the surface temperature increases from 280 K to 320 K, the feedback magnitude declines somewhat, from 2.4 W/m$^2$/K to 1.9 W/m$^2$/K. At this humidity, we do not see a high-temperature transition to a runaway greenhouse state in which OLR becomes insensitive to surface temperature. This is similar to calculations reported by McKim et al. (2021), who showed an appreciable hot-climate clear-sky longwave feedback for intermediate and low humidities. By including $CO_2$ and VB, our calculations may increase the clear-sky longwave feedback even further.

In the following subsections, we decompose the total feedback into four distinct components.

### 4.3.1 Surface Planck Feedback

When quantifying climate feedbacks, it is conventional to calculate a "Planck feedback" which quantifies the response of OLR to a uniform change in surface and tropospheric temperature. In this study we shall further divide the Planck feedback in to a surface and atmospheric component. In the Surface Planck (SP) feedback, a warmer surface emits greater longwave radiation to space, principally through the relatively transparent water vapor window (Koll and Cronin 2018; McKim et al. 2021). The SP feedback is calculated by introducing a partial radiative perturbation $\delta T_s$ to surface temperature $T_s$, holding all other properties fixed. The SP feedback magnitude is then:

$$\lambda_{SP} = \frac{OLR(T_s + \delta T_s, T_a, q) - OLR(T_s, T_a, q)}{\delta T_s} \tag{4}$$

[3] This study only addresses tropospheric feedbacks, as the model may not contain the essential physics governing the stratospheric water vapor feedback.

The atmospheric profiles $T_a$ and $q$ are held fixed when calculating $\lambda_{SP}$. In all our feedback calculations we use downward perturbations in surface temperature ($\delta T_s < 0$). The value of $\lambda_{SP}$ for $\beta = 0.5$ is shown by the green curve in Figure 4.2. In climates at and below a surface temperature of 300 K (nearly all of present-day Earth), the SP feedback is the leading-order clear-sky longwave feedback. Figure 4.4a shows the SP feedback in the spectral dimension for surface temperatures of 290 K and 310 K. The feedback is contained almost entirely within the relatively transparent water vapor window between 800 and 1300 cm[1]. At high surface temperatures the water vapor window begins to close due to continuum absorption in the lower atmosphere, reducing the magnitude of the SP feedback.

### 4.3.2 Atmospheric Planck Feedback

The Atmospheric Planck (AP) feedback quantifies the response of OLR to a vertically uniform warming of the atmosphere equal to that of the surface. This is implemented in the model by perturbing the tropospheric temperature by the amount $\delta T_s$, holding the stratosphere fixed. Since this warming is applied to the whole troposphere, including the moist plume, the saturation specific humidity also increases. This causes a perturbation to the environmental humidity $\delta q_{AP}$:

The magnitude of the AP feedback is given by:

$$\lambda_{AP} = \frac{OLR(T_s, T_a + \delta T_s, q + \delta q_{AP}) - OLR(T_s, T_a, q)}{\delta T_s} \tag{5}$$

In this formulation, the value of the AP feedback is the result of a competition between perturbations to temperature and to water vapor, which have opposite effects on OLR. The AP feedback is given by the

$$\delta q_{AP} = \beta(q^*(T + \delta T_s) - q^*(T)) \tag{6}$$

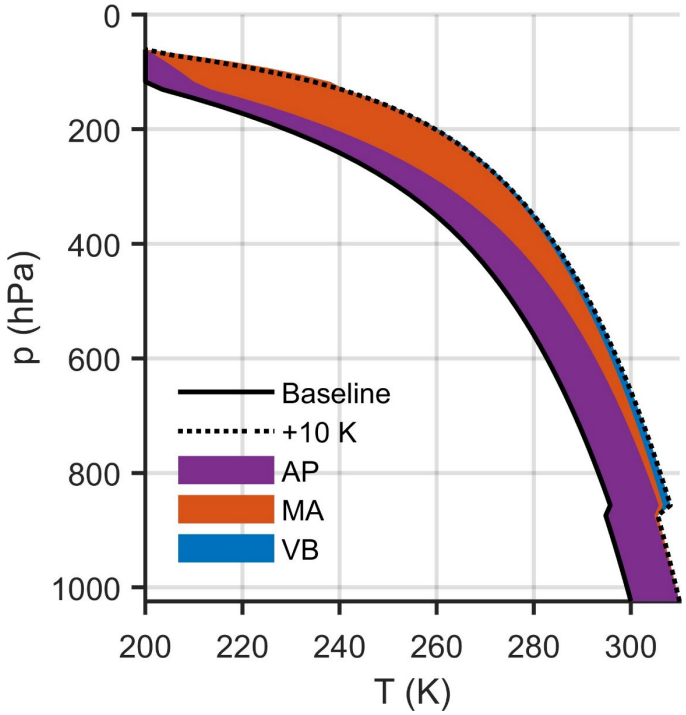


**Figure 4.3.** Partial radiative perturbations in the 1D climate model. The black lines represent the temperature profiles of two different atmospheres separated by 10 K of surface warming. The colors represent warming components to which we attribute different climate feedbacks.

purple line in Fig. 4.2. The feedback magnitude steadily increases with surface warming up to a surface temperature of around 310 K, above which it begins to decay. The spectrally resolved AP feedback (Fig. 4.4b) maximizes on the edges of the $CO_2$ band (between 600 and 800 $cm^{-1}$), where additional water vapor brought by warming does not significantly alter the emission level. This is consistent with the findings of Seeley and Jeevanjee (2021) and Koll et al. (2023), who also showed that the $CO_2$ bands are responsible for a stabilizing climate feedback.

### 4.3.3 Moist Adiabat Feedback

The moist-adiabatic lapse rate declines with climate warming, causing greater warming (but also greater specific humidity) in the upper troposphere than in the lower troposphere. We call the OLR response to this top-heavy warming profile the Moist Adiabat (MA) feedback. The associated partial temperature

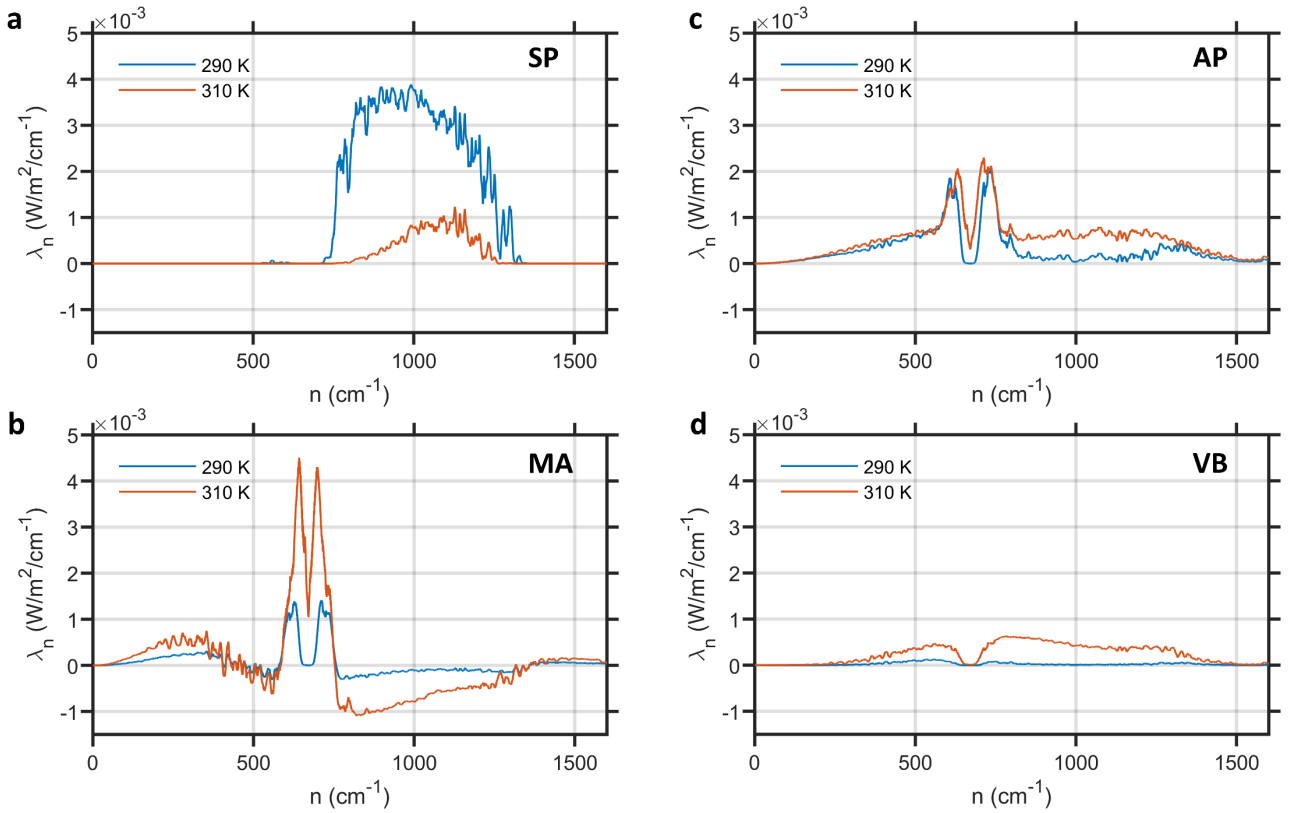


**Figure 4.4.** Spectrally resolved clear-sky longwave feedbacks in the 1-D climate model for $RH_\rho = 0.5$. We apply a 10 cm$^{-1}$ moving average to the data to improve interpretability.

perturbation $\delta T_{MA}$ is calculated as the residual of the change in moist-plume temperature after removing the vertically uniform component:

$$\delta T_{MA} = T_m(p, T_s + \delta T_s) - T_m(p, T_s) - \delta T_s \tag{7}$$

The top-heavy structure of $\delta T_{MA}$ is shown in Fig. 4.3, which depicts the sum of partial temperature perturbations in the model between surface temperatures of 300 K and 310 K. As before, the change to moist-column temperature causes a perturbation to environmental water vapor:

$$\delta q_{MA} = \beta(q^*(T + \delta T_{MA}) - q^*(T)) \tag{8}$$

The MA feedback is then given by competition between these two perturbations:

$$\lambda_{MA} = \frac{OLR(T_s, T_a + \delta T_{MA}, q + \delta q_{MA}) - OLR(T_s, T_a, q)}{\delta T_s} \quad (9)$$

$\lambda_{MA}$ is shown by the red line in Fig. 4.8. Despite the outsize warming due to the moist adiabat at superhot surface temperatures, the MA feedback does not achieve leading-order magnitude for any of the climates investigated here. As shown in Fig. 4.4c, this behavior is largely due to the competition between a large negative feedback component in the $CO_2$ bands and a large positive component in the water vapor window (likely due to water vapor masking of the SP and VB feedbacks).

### 4.3.4 Vapor-Buoyancy Feedback

The VB feedback in this model is calculated via partial radiative perturbations to temperature alone:

$$\delta T_{VB} = \Delta T_{VB,1D}(T_m + \delta T_s + \delta T_{MA}, q) - \Delta T_{VB,1D}(T_m, q) \quad (10)$$

Since the VB feedback results from temperature changes only in the subsaturated column, there is no perturbation in specific humidity associated with it. That is, $\delta q_{VB} = 0$. This choice is consistent with our findings in the previous section showing essentially no change in the water vapor feedback due to VB in the MD-DYN experiment, and little change in the net feedback between MD-DYN and MD-ALL. The VB feedback is then given by:

$$\lambda_{VB} = \frac{OLR(T_s, T_a + \delta T_{VB}, q) - OLR(T_s, T_a, q)}{\delta T_s} \quad (11)$$

Figure 4.3 shows the bottom-heavy warming profile associated with VB in the model. The blue curve in Fig. 4.2 shows the VB feedback. The feedback in this model (also shown in Fig. 3.6) has a similar magnitude to that of the GCM as well as the 2D CRM, and its magnitude similarly increases with warming. At surface temperatures around that of the present-day tropics (about 300 K), the VB feedback overtakes the MA feedback as the dominant lapse-rate feedback mechanism. It begins to approach leading order in hothouse climates approaching 320K surface temperature. Such hothouse surface temperatures may have occurred briefly on Earth as it exited snowball a state (Pierrehumbert et al., 2011), and may occur on Earth-

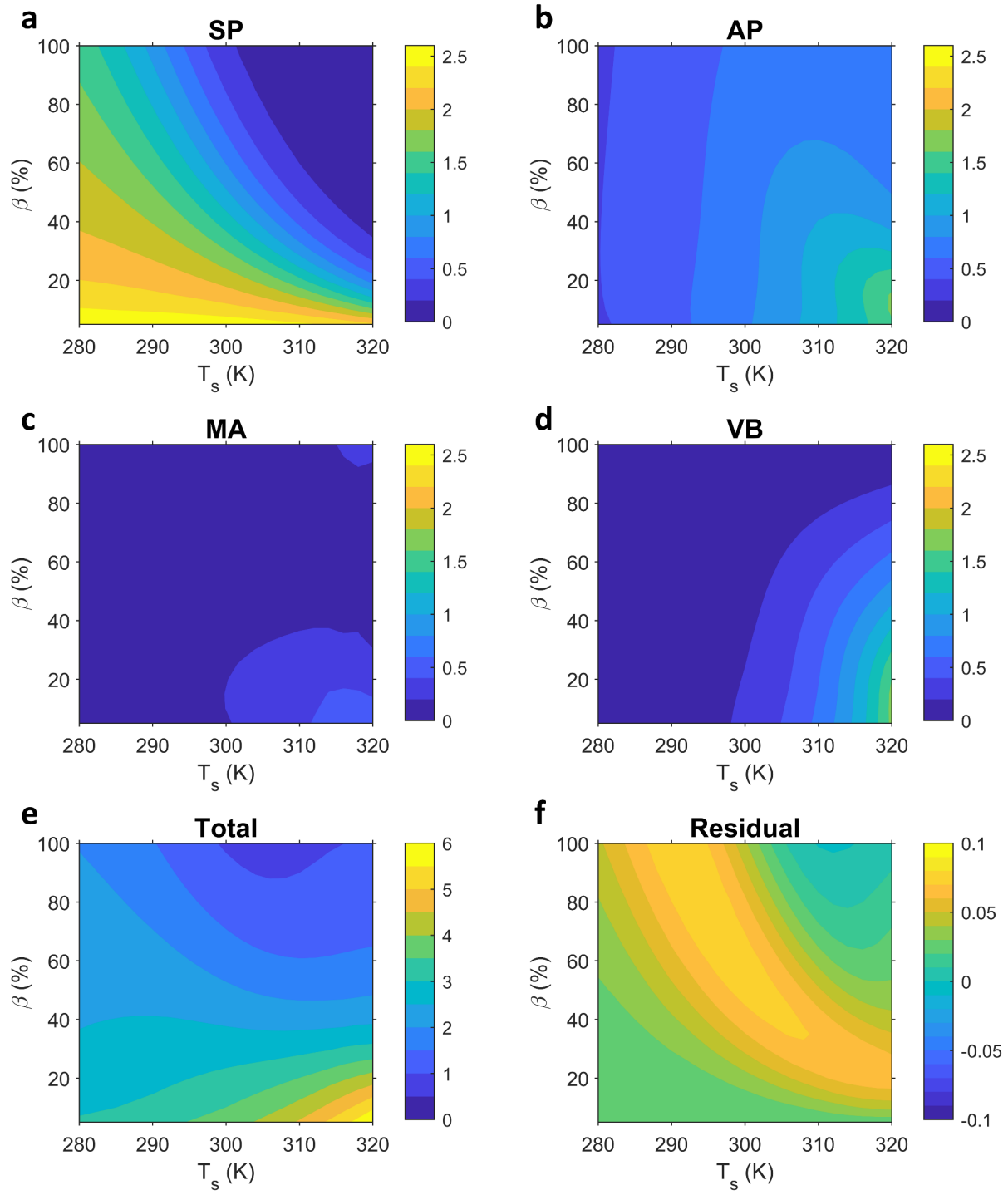


**Figure 4.5.** Clear-sky temperature feedbacks in the 1-D climate model for a wide range of temperatures and humidities ($W/m^2/K$). Note the difference in color scale between the panels.

like planets orbiting distant stars. The AP and VB feedbacks together allow the atmosphere to maintain a nearly constant total feedback of approximately 2 $W/m^2/K$ despite the loss of the SP feedback due to the closure of the water vapor window.

### 4.3.5 Humidity dependence of clear-sky longwave feedbacks.

Figure 4.5 shows the values for each of the 1D model's feedbacks over a range of surface temperature and humidity. Each of the temperature-based feedbacks in this model is greater in a dry climate, though the reasons for this vary. The VB feedback is greater because the VB temperature perturbation $\delta T_{VB}$ is greater in an atmosphere with smaller $\beta$. The inclusion of $CO_2$ in the model atmosphere also means that there is an appreciable VB feedback even at 0% $RH_\rho$, a significant departure from the results of Seidel and Yang (2020), whose 1D model did not include $CO_2$. The dry climate favors the SP feedback due to weakened continuum absorption in the water vapor window. Reduced humidity also favors the AP and MA feedbacks because reduced water vapor broadens the portion of the $CO_2$ spectrum emitting to space, consistent with calculations reported by Koll et al. (2023). The strong, nonlinear humidity-dependence of the total climate feedback resembles findings by McKim et al. (2021) in a similar model without VB. The clear-sky longwave feedback does not go to zero in significantly subsaturated climates. A runaway greenhouse may not occur in clear skies in this temperature range. Other physics may be necessary to destabilize climates at high surface temperatures.

## 4.4 Discussion

The feedback calculations in this chapter help to place the VB feedback within the broader context of clear-sky longwave feedbacks, particularly in the critical transition from a climate dominated by the surface feedback to a climate dominated by atmospheric feedbacks. For me, one of the most interesting findings is that the moist-adiabat feedback is small across the temperature and humidity spectrum we tested, and in many cases much smaller than the VB feedback. That is, vapor buoyancy may be the dominant lapse-rate-type feedback in hot tropical climates. That result entirely due to our modeling choice to include a countervailing water vapor feedback with the MA feedback but not the VB feedback. However, that choice can be readily justified: there is strong evidence that the distribution of relative humidity changes little with climate warming (Isaac M. Held & Shell, 2012), which would imply that lapse-rate-type climate feedbacks

must be paired with a countervailing water feedback. Our GCM experiments showed that the VB feedback is an exception to this rule, as removing VB from the dynamical core did not meaningfully alter the water vapor feedback. Our choice to include the countervailing component of the water vapor feedback is certainly responsible for the smallness of the

I hope to continue working with this model. It would be interesting to compare the MA and VB feedbacks as calculated in this model – through marginal perturbations from a base state – to the feedbacks as calculated by removing one process or the other from the model entirely (as we did for VB in the CRM and GCM). It is likely that will yield a somewhat different quantification of those feedbacks because the MA feedback mechanism interacts with all the other feedbacks through increased water vapor masking surface and lower-troposphere emission. Finally, it remains to be seen how VB influences super-hot climates in a comprehensive climate model. Our 1D model suggests that VB may delay or prevent a runaway greenhouse in clear-sky radiation: does this occur in hothouse climate simulations, or do other unaccounted-for positive feedbacks cause the system to run away?

# 5 Anvil and Tropopause in a Wide Array of Cloud-Resolving Simulations


## Abstract

We present 123 cloud-resolving simulations to study how temperatures of anvil clouds and radiative tropopause (RT) change with surface warming. Our simulation results show that the RT warms at approximately the same rate as anvil clouds. This relationship persists across a variety of modeling choices, including surface temperature, greenhouse gas concentration, and the representation of radiative transfer. We further show that the shifting ozone profile associated with climate warming may give rise to a fixed RT temperature as well as a fixed anvil temperature. This result points to the importance of faithful treatment of ozone in simulating clouds and climate change; the robust anvil-RT relationship may also provide alternative ways to understand what controls anvil temperature.


## 5.1 Introduction

The tropical upper troposphere is home to extensive cirrus clouds detrained from thunderstorms, known as anvil clouds. As the surface warms, anvil clouds are robustly predicted to rise to greater altitudes so that their mean temperature increases less than that of the surface. This holds true in cloud-resolving models (CRMs) (Harrop & Hartmann, 2012; M. Khairoutdinov & Emanuel, 2013; Kuang & Hartmann, 2007; Narenpitak et al., 2017; Tompkins & Craig, 1999) and general circulation models (GCMs) (D. W. J. Thompson et al., 2017; Zelinka & Hartmann, 2010), as well as observations (Zelinka & Hartmann, 2011). Since anvil clouds' temperature changes little under surface warming, they will emit less longwave radiation to space than if they were to retain the same, warmer altitude. This yields a positive climate feedback when our reference assumption is that clouds would otherwise be fixed in altitude. For this reason, the most recent IPCC report expressed *high confidence* in a positive longwave cloud altitude feedback (Forster et al., 2021).

The Fixed Anvil Temperature (FAT) hypothesis is the most enduring explanation for the trend of high-cloud temperature with surface warming (Hartmann & Larson, 2002). The FAT hypothesis claims that (1) upper tropospheric cloud amount is principally the result of the radiatively-driven horizontal convergence in clear skies, and (2) this convergence is physically constrained to occur at a fixed temperature where, for fixed relative humidity, the water vapor concentration becomes so small that it loses its ability to efficiently cool the atmosphere. Indeed, studies of CRMs, GCMs, and observations corroborate the first claim. The upper tropospheric maximum in convergence covaries with the upper tropospheric maximum in cloud amount (Bony et al., 2016; Kuang & Hartmann, 2007; Seeley, Jeevanjee, & Romps, 2019; Zelinka & Hartmann, 2010, 2011). However, models often contradict the second claim in FAT, showing that anvils and the location of maximum convergence may in fact warm appreciably, albeit slowly compared to the surface. For example, Kuang and Hartmann (Kuang & Hartmann, 2007) showed in a CRM that the location of maximum cloud fraction to warm by 2 K when the surface warmed by 8 K, and the recent Radiative-Convective Equilibrium Model Intercomparison Project found an average of 4.4 K of anvil warming over 10 K of surface warming (Wing et al., 2020). This slow but appreciable warming is sometimes known as a Proportionately Higher Anvil Temperature, or PHAT (Zelinka & Hartmann, 2010). PHAT is often found in models where the ozone profile is unrealistically fixed in pressure (Harrop & Hartmann, 2012).

It is sometimes assumed that anvil clouds are linked to the radiative tropopause (RT), where radiative heating first goes to zero in the upper troposphere (see, e.g., Birner and Charlesworth 2017; Kluft et al. 2019). The RT is the intersection of the radiative-convective equilibrium (RCE) temperature profile of the troposphere and the radiative or radiative-dynamical equilibrium profile of the stratosphere (S. Hu & Vallis, 2019; Vallis et al., 2015). Since RT is the highest location where latent heating from convection balances radiative cooling in RCE, the RT is also known as the convective top (Birner & Charlesworth, 2017; Dacie et al., 2019; Thuburn & Craig, 2002). However, convective clouds in fact occur considerably above this point as they overshoot the level of neutral buoyancy (Z. Hu et al., 2021; Kuang & Bretherton, 2004). Tompkins and Craig (Tompkins & Craig, 1999) found in a CRM that anvil temperature to increase with

surface warming. They suggested this occurred because the RT temperature increases with warming due to their fixed ozone profile. In Kluft et al. (2019), RT is found to warm by about 0.5 K per 1 K of surface warming in a 1-D RCE model without clouds. Assuming a close relationship between RT and anvil, the authors suggested that their result supported a PHAT. Such an assumption appears to be a crude simplification of FAT/PHAT thinking, according to which a decline in radiative cooling with height below RT causes clear-sky convergence.

Since RT may be simulated by 1-D models without clouds, a robust anvil-RT relationship would simplify our understanding of anvil clouds. However, Seeley et al. (Seeley, Jeevanjee, & Romps, 2019) achieved a contrary result in "minimal recipe" CRM simulations which isolated the longwave effect of water vapor by removing all other radiative constituents from the model. In their simulations the temperature of RT varied by less than 2 K despite 50 K of surface warming, yet the anvil warming was greater by an order of magnitude. They suggested there is a fixed (radiative) tropopause temperature (FiTT) with respect to surface warming, and RT temperature is unlikely to be related to the temperature of the anvil peak. That is, the top of the troposphere should be disentangled from the anvil location. However, Hartmann et al. (Hartmann et al., 2019) presented CRM simulations in which the anvil, the RT, and a sharp peak in the detrainment of cloud ice each occurred at a fixed temperature over 5 K of surface warming. They proposed that in convection-permitting RCE simulations the anvil is linked to the location of RT, as convective cooling from overshooting updrafts above the anvil must be compensated by radiative heating. Given this disagreement and the potential clarity provided by an anvil-RT relationship, it is worthwhile to investigate more thoroughly whether the location and temperature anvil clouds are in fact related to the location and temperature of RT.

Modeling choices about ozone are particularly important to the simulated anvil and RT temperatures. Many modeling studies of RCE often use an ozone profile which is unrealistically fixed in pressure, which can give rise to a PHAT (Kuang & Hartmann, 2007; Tompkins & Craig, 1999; Wing et al., 2020; Zelinka & Hartmann, 2010) as well as an increasing RT temperature (Dacie et al., 2019; Kluft et al., 2019). This

occurs because the upper troposphere is lifted into a layer of stronger ozone heating. A real atmosphere may give rise to a FAT as climate warming lifts the ozone profile higher in the atmosphere. On this assumption, CRM studies of anvil temperature have modeled an atmosphere with zero ozone (Harrop & Hartmann, 2012; Seeley, Jeevanjee, & Romps, 2019). In a similar vein, Nowack et al. (P. J. Nowack et al., 2015, 2018) found that prescribing an ozone profile fixed in pressure reduced upper tropospheric cloud amount in a GCM and reduced the positive cloud longwave feedback by about 0.1-0.2 $W/m^2/K$ as compared to simulations with interactive ozone. However, those two studies did not isolate the cloud altitude feedback, and to our knowledge it has yet to be explicitly verified whether the upward shift of ozone with warming equally offsets the PHAT behavior to give rise to an approximate FAT.

To test for an anvil-RT relationship, we conduct idealized experiments in a CRM systematically changing the radiation-relevant model settings. We ask: Do changes in model settings that change the simulated RT temperature cause similar changes in the anvil temperature? Are changes in the RT temperature's *trend* with respect to surface warming associated with similar changes in the anvil temperature trend? In particular, we test the sensitivity of anvil and RT temperature to: (1) A wide range of surface temperatures (280 K to 315 K); (2) the amount of carbon dioxide; (3) the amount of insolation; (4) the shape, concentration, and location of the ozone profile; (5) the presence of a large-scale circulation and convective organization; and (6) the domain size.

## 5.2 Simulations

We use the 2D formulation of the System for Atmospheric Modeling (SAM), version 6.10 (M. F. Khairoutdinov & Randall, 2003). SAM is a cloud-permitting model using the anelastic equations for dynamics. 2D CRMs have long been used to study convection and clouds in the tropics (Blossey et al., 2010; Grabowski et al., 2000; I. M. Held et al., 1993; Seidel & Yang, 2020; D. Yang, 2018a, 2018b). The horizontal resolution is 2 km. Radiation is parameterized using the Rapid Radiative Transfer Model for GCMs (RRTMG) (Mlawer et al., 1997). Cloud microphysics are parameterized using the SAM one-

| Experiment | Domain | Ozone | Insolation | $CO_2$ |
|---|---|---|---|---|
| Standard | 256 km | Standard | 409.6 W/m$^2$ | 280 ppm |
| Standard, no $CO_2$ | 256 km | Standard | 409.6 W/m$^2$ | 0 ppm |
| Standard, 4x$CO_2$ | 256 km | Standard | 409.6 W/m$^2$ | 1120 ppm |
| No Solar | 256 km | Standard | 0 W/m$^2$ | 0 ppm |
| 2x Solar | 256 km | Standard | 819.2 W/m$^2$ | 0 ppm |
| $H_2O$-only SW | 256 km | Standard | 409.6 W/m$^2$ (absorbed only by $H_2O$) | 0 ppm |
| $O_3$-only SW | 256 km | Standard | 409.6 W/m$^2$ (absorbed only by $O_3$) | 0 ppm |
| $O_2$-only SW | 256 km | Standard | 409.6 W/m$^2$ (absorbed only by $O_2$) | 0 ppm |
| Unif-$O_3$ | 256 km | Uniform | 409.6 W/m$^2$ | 280 ppm |
| No $O_3$ | 256 km | None | 409.6 W/m$^2$ | 280 ppm |
| Large | 2048 km | Standard | 409.6 W/m$^2$ | 280 ppm |
| Large-Organized* | 2048 km | Standard | 409.6 W/m$^2$ | 280 ppm |
| Standard-3D | 80km x 80km | Standard | 409.6 W/m$^2$ | 280 ppm |
| Thompson* | 256 km | Standard | 409.6 W/m$^2$ | 280 ppm |
| CAM Radiation* | 256 km | Standard | 409.6 W/m$^2$ | 280 ppm |

**Table 5.1. Summary of all idealized experiments conducted in this study.** Each experiment consists of 8 simulations with prescribed surface temperatures of 280 K, 285 K, 290 K, 295 K, 300 K, 305 K, 310 K, and 315 K. The asterisks denote further modifications not reflected in this Table: The Large-Organized experiment is conducted without homogenized radiation. The Thompson experiment uses Thompson microphysics rather than the SAM one-moment scheme. The CAM Radiation experiment is conducted using the CAM3 radiation scheme rather than RRTMG.

moment scheme. For the purposes of replicability and comparability, we borrowed many modeling parameters from the Radiative Convective Equilibrium Model Intercomparison Project (RCEMIP) protocol (Wing et al., 2018). The vertical grid is a modified version of the RCEMIP high-vertical-resolution grid, extended to allow for greater surface temperature. It consists of 160 levels, with a vertical resolution of 40m at the surface, 200m at altitudes between 3 km and 25 km, and increasing to 500m above that. The model top is at 36 km. A sponge layer occupies the upper 30% of the model domain. The model stratosphere is allowed to equilibrate without any nudging of the thermodynamic profiles. To accommodate the

computational cost of exploring a wide range of modeling conditions, as well as the long equilibration times required, our standard simulations use a small, 256 km domain. To test the relevance of convective organization, we use a larger 2048 km domain. Following RCEMIP, we use an idealized equatorial ozone profile and $CH_4$ and $N_2O$ concentrations of 1650 and 306 ppbv, respectively. Insolation is fixed at 409.6 $W/m^2$. Unlike the RCEMIP protocol, we set $CO_2$ to its preindustrial value of 280 ppmv. All other well-mixed greenhouse gases are set to zero.

The model is run over a sea surface with a prescribed temperature until the atmosphere approximately reaches radiative-convective equilibrium (RCE). RCE is an idealization of the tropical atmosphere which states that the latent heating from convection is balanced by radiative cooling in the free troposphere. Each simulation is integrated for 500 days, except for simulations without ozone, which required 1000 days to equilibrate. The data reported are from the final 40% of the model integration. We identify cloudy grid cells as those whose condensates exceed either $1x10^{-5}\ kg/kg$ or 1% of the saturation specific humidity, whichever is smaller. This is consistent with the method of the RCEMIP protocol as well as SAM's own diagnostic code. Even for small domains, SAM has a high propensity to undergo convective self-aggregation, in which convection spontaneously organizes into persistent moist and dry patches (Bretherton et al., 2005; I. M. Held et al., 1993; Tompkins, 2001). The spatial scale of self-aggregation depends on surface temperature (D. Yang, 2018b), altering the climate state in ways independent of the physics at interest here. To prevent this, we horizontally homogenize radiation after computing each column, except in a set of large-domain simulations testing the importance of organization. To verify that the choice of a 2D modeling domain does not give substantially altered results, we performed 200-day 3D simulations in an 80 km x 80 km domain with a resolution of 1km. Due to the long equilibration times required, the 3D simulations were initialized using thermodynamic profiles from an otherwise identical 2D simulation. Since cloud microphysics are known to affect the properties of convection and convective clouds (Z. Hu et al., 2021; Sokol & Hartmann, 2022), we have performed one set of simulations with Thompson microphysics (G. Thompson et al., 2008). Each "experiment" in this study consists of eight simulations with prescribed

sea-surface temperatures from 280 K to 315 K. We present fifteen experiments in total, variously adjusting the $CO_2$ concentration, the insolation, and the ozone profile. These experiments are summarized in Table 5.1.

## 5.3 Results

As the climate warms, anvil clouds rise in altitude so that their temperature increases less than the air at any given level. Figure 5.1a shows profiles of cloud fraction from the Standard simulations (see Table 1). The cloud fraction profile has a two-peaked structure. Following the convention of other studies (Kuang & Hartmann, 2007; Wing et al., 2020), we refer to upper-tropospheric peak in cloud fraction as the anvil. The anvil migrates upward as the surface warms. Figure 5.1b shows cloud fraction on a temperature coordinate and normalized by dividing by its local maximum value. The anvil temperature increases with warming.

We require a precise and general definition of "anvil temperature" appropriate for the wide range of surface temperature and physics perturbations in this study. Defining anvil to be the temperature where the cloud fraction reaches its maximum value (Kuang & Hartmann, 2007; Seeley, Jeevanjee, & Romps, 2019; Wing et al., 2020) proved inadequate for some of our experiments. Our testing showed that the temperature of maximum cloud fraction may shift dramatically with warming due to a modest change in cloud profile shape, rather than a meaningful change in high-cloud. Using a cloud-mass-weighted temperature over the entire portion of the troposphere below a certain temperature (Harrop & Hartmann, 2012; Zelinka & Hartmann, 2010) is also not adequate for our experiments. Given the wide range of surface temperatures in our experiments, there is not a single temperature or pressure level consistently demarcating the "upper troposphere" from the "lower troposphere". To avoid these shortcomings, we first identify the upper-tropospheric peak in cloud fraction. Then we calculate a cloud-mass-weighted temperature over the locations where cloud coverage of at least 80% of that maximum value:

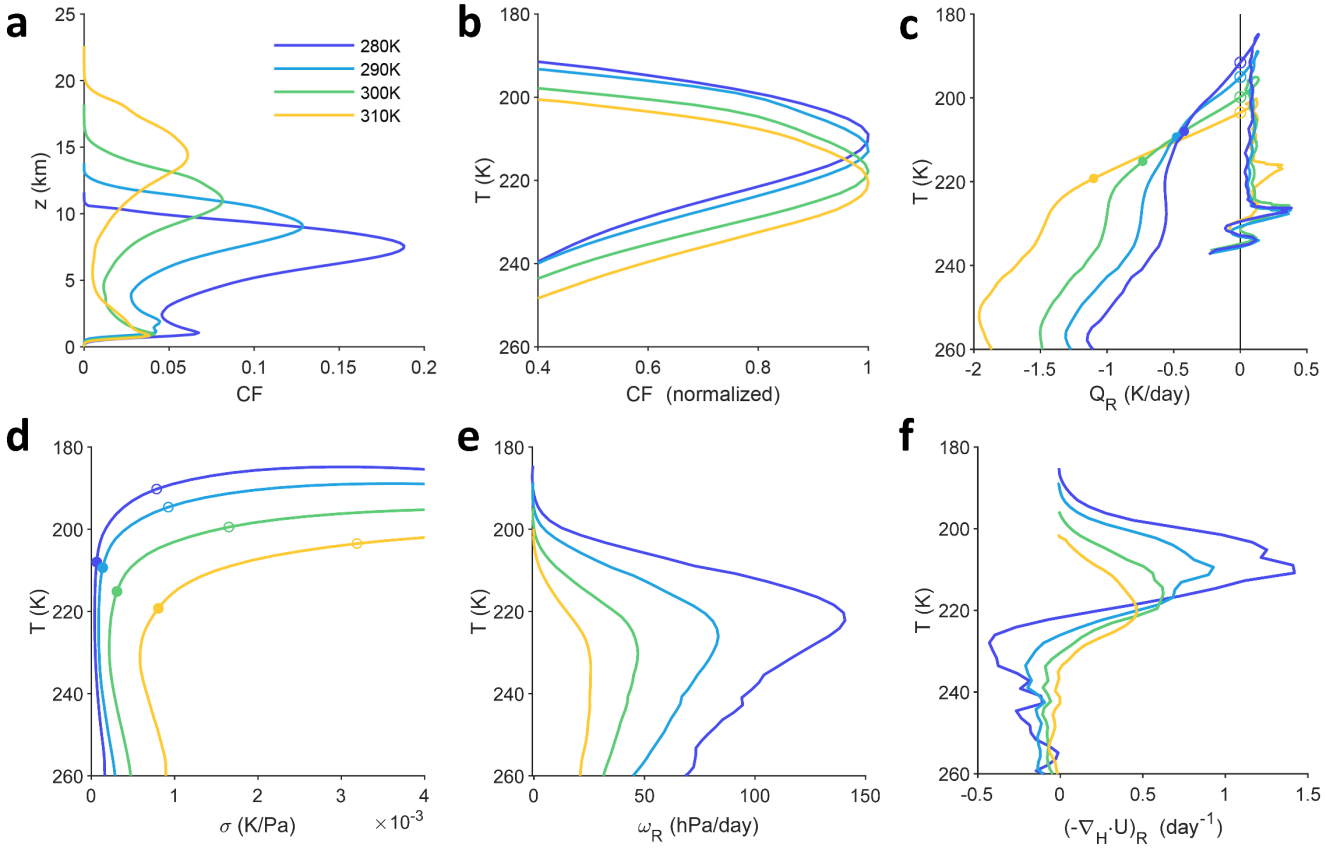


**Figure 5.1. The Standard experiment.** (a) Profiles of cloud fraction from the Standard simulations. (b) Cloud fraction, normalized by its maximum value, and plotted against temperature. (c) All-sky radiative heating plotted against temperature. The open circles on the y-intercept indicate RT. The closed circles indicate the location of $T_{Conv}$. (d) Static stability profiles. The open circles indicate RT. The closed circles indicate $T_{Conv}$. (e) Radiatively driven subsidence. (f) Radiatively driven convergence.

$$T_{Anv} = \frac{\int_{p_{80\%,\uparrow}}^{p_{80\%,\downarrow}} T(p) \cdot CF(p)\, dp}{\int_{p_{80\%,\uparrow}}^{p_{80\%,\downarrow}} CF(p)\, dp} \tag{12}$$

where T is temperature, CF is cloud fraction, and $p_{80\%,\uparrow}$ and $p_{80\%,\downarrow}$ are the highest and lowest pressure levels where the cloud fraction is at least 80% of its maximum value. This cutoff is arbitrary choice, but in the supplemental material we show that Eq. (12) gives nearly the same temperature as a strict "peak" definition except in a few cases where the shape of the cloud profile changes abruptly with warming (Appendix Figs. 5.8 and 5.9). In those cases Eq. (12) retains monotonic behavior rather than allowing an

arbitrary jump in $T_{Anv}$. Therefore, this method is more appropriate for this study. To reduce the imprecision introduced by a discrete model resolution, we linearly interpolate $T(p)$ and $CF(p)$ in pressure and calculate the integral in Eq. (12) numerically.

Figure 5.2 shows $T_{Anv}$ for each experiment in this study. In the Standard simulations, anvil temperature ($T_{Anv}$) increases by 13.2 K while the surface temperature ($T_s$) increases by 35 K, so that $\Delta T_{Anv}/\Delta T_s = 0.38$. The anvil warms appreciably albeit more slowly than the surface, which agrees with previous CRM and GCM studies. (Harrop & Hartmann, 2012; M. Khairoutdinov & Emanuel, 2013; Kuang & Hartmann, 2007; Zelinka & Hartmann, 2010). RCEMIP, whose protocol forms the basis for our experimental design, showed an average anvil warming of $\Delta T_{Anv}/\Delta T_s = 0.44$ (Wing et al., 2020).

As the climate warms, the RT becomes warmer as well. Figure 5.1c shows all-sky radiative heating against temperature as a vertical coordinate. Considering the troposphere as the region of the atmosphere in radiative-convective equilibrium, we identify RT as the temperature at which radiative heating changes sign. That is, RT is the y-intercept in Fig. 5.1c, marked with an open circle for each simulation. The RT temperature for the Standard experiment is shown in Fig. 5.2a. RT temperature ($T_{RT}$) increases by 14.8 K over a 35 K increase in $T_s$, so that $\Delta T_{RT}/\Delta T_s = 0.42$. This replicates recent studies of radiative-convective equilibrium in 1-D models without clouds. Kluft et al. (2019) showed $\Delta T_{RT}/\Delta T_s \approx 0.5$ and noted that the temperature increase of RT (or "convective top") resembled the slow temperature increase of anvil clouds. Dacie et al. (2019) similarly showed $\Delta T_{RT}/\Delta T_s \approx 0.4$, though that study defined RT as the threshold where convective heating (or radiative cooling) equals 0.2 K/day.

### 5.3.1 Radiatively Driven Convergence

The cloud fraction profile is the result of sources and sinks of cloudy air: detrainment from the convective core and evaporation or precipitation, respectively (Seeley, Jeevanjee, Langhans, et al., 2019). We focus on one component of the sources, due to the radiatively driven subsidence of air in clear skies (Kuang & Hartmann, 2007; Zelinka & Hartmann, 2010):

$$\omega_R = -\frac{Q_R}{\sigma} \tag{13}$$

Here, $\omega_R$ is a pressure velocity (Pa/day), $Q_R$ is the radiative heating rate (K/day) and σ is the static stability (K/Pa), given by:

$$\sigma = \frac{\Gamma_d - \Gamma}{\rho g} \tag{14}$$

where Γ is the lapse rate (K/m), $\Gamma_d$ is the dry-adiabatic lapse rate, $\rho$ is density, and $g$ is the acceleration due to gravity. The radiatively driven horizontal convergence of air in clear skies is then given by:

$$(-\nabla_H \cdot \mathbf{U})_R = \partial\omega_R/\partial p \tag{15}$$

In the absence of mean ascent or subsidence over the domain, $(-\nabla_H \cdot \mathbf{U})_R$ is balanced by divergence out of the convective region at the same altitude. Past modeling studies found that the peak upper-tropospheric cloud fraction tends to be located at or near the maximum in $(-\nabla_H \cdot \mathbf{U})_R$ (Kuang & Hartmann, 2007; Seeley, Jeevanjee, & Romps, 2019; Zelinka & Hartmann, 2010). **U** is a large-scale velocity. The velocities associated with individual convective events are generally greater but in aggregate would imply divergence from convective plumes at approximately the same level.

The radiative heating rate $Q_R$ from the Standard experiment is shown in Fig. 5.1c. Since radiation is horizontally homogenized in our simulations, we use domain-averaged values of $Q_R$ in our calculation. Figures 1d and 1e show σ and $\omega_R$, plotted against a temperature coordinate. The static stability σ increases with height as the atmosphere transitions from a radiative-convective equilibrium temperature profile below to a more stable radiative equilibrium profile above. This transition to greater static stability is coincident with a steady decline in the magnitude of $Q_R$ toward the RT. Therefore, $\omega_R$ declines sharply with altitude at that level. The peak in radiative convergence $(-\nabla_H \cdot \mathbf{U})_R$ occurs there, as shown in Fig. 5.1f. The peak shifts to a higher temperature as the surface temperature increases, much like the peak in cloud fraction in Fig. 5.1b. Separately, the magnitude of $(-\nabla_H \cdot \mathbf{U})_R$ declines due to increasing $\sigma$. This matches a decline in

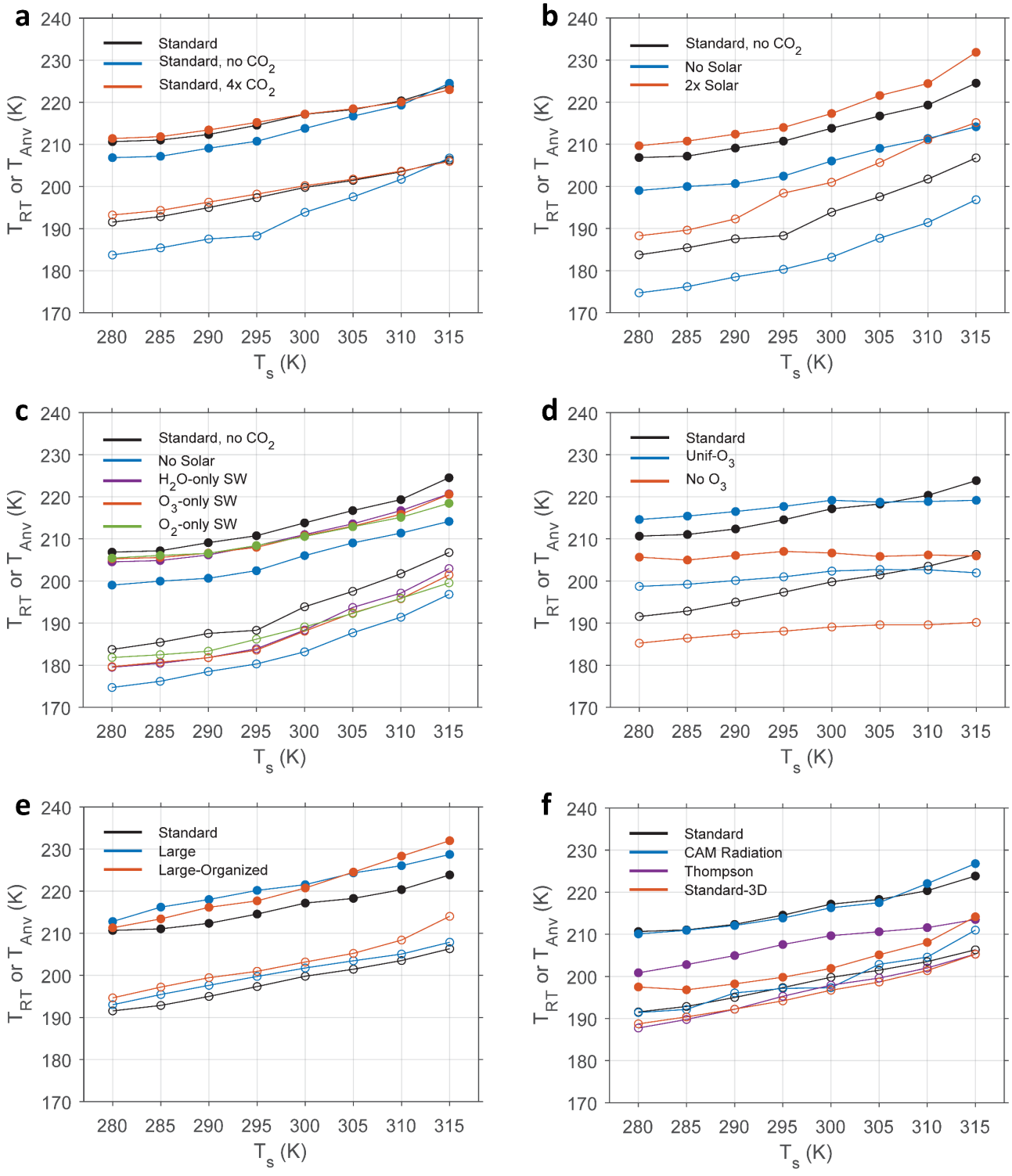


**Figure 5.2.** RT temperature (open circles) and anvil temperature (closed circles) for each simulation used in this study. Black lines and marks indicate a simulation, also present in another panel, used as a baseline for comparison.

anvil cloud extent seen in Fig. 5.1a, consistent with the "stability iris" hypothesis described by Bony et al. (Bony et al., 2016).

### 5.3.2 Sensitivity to $CO_2$

We examine the relationship between the anvil and RT temperatures using a variety of modeling choices. We ask: do anvil temperature and RT temperature covary in response to a change of model parameters? We will focus on a sequence of experiments designed to elucidate the physical processes governing anvil and RT. We begin by removing carbon dioxide from the Standard setup. With $CO_2$ removed, RT and anvil become colder. The temperature increases more rapidly with warming ($\Delta T_{RT}/\Delta T_s = 0.66$), as does the anvil temperature ($\Delta T_{Anv}/\Delta T_s = 0.50$). Figure 5.3a shows the clear-sky $CO_2$ longwave heating rate from the Standard experiment. We obtain this from offline radiative transfer calculations with and without $CO_2$ in RRTMG, using the Standard experiment thermodynamic profiles. This calculation reasonably captures the differences in all-sky radiative heating between the Standard experiment and its no-$CO_2$ counterpart (Fig. 5.3b). $CO_2$ causes net heating around RT. This may be explained by the curvature of the temperature profile: near RT $CO_2$ is absorbing radiation from the warm troposphere below, while only emitting at its own, relatively cold temperature (Thuburn & Craig, 2002). This $CO_2$ heating results in a greater radiative equilibrium temperature and therefore a greater RT temperature. The anvil warming from $CO_2$ may be due to a shift in the static stability profile (Fig. 5.3c). RT marks the transition from the tropospheric RCE temperature profile below to the approximate radiative equilibrium profile above, which requires a sharp increase in static stability in the upper troposphere. Via eqs. (2) and (4), this helps to set the peak radiatively-driven convergence and anvil location, linking the RT to the anvil.

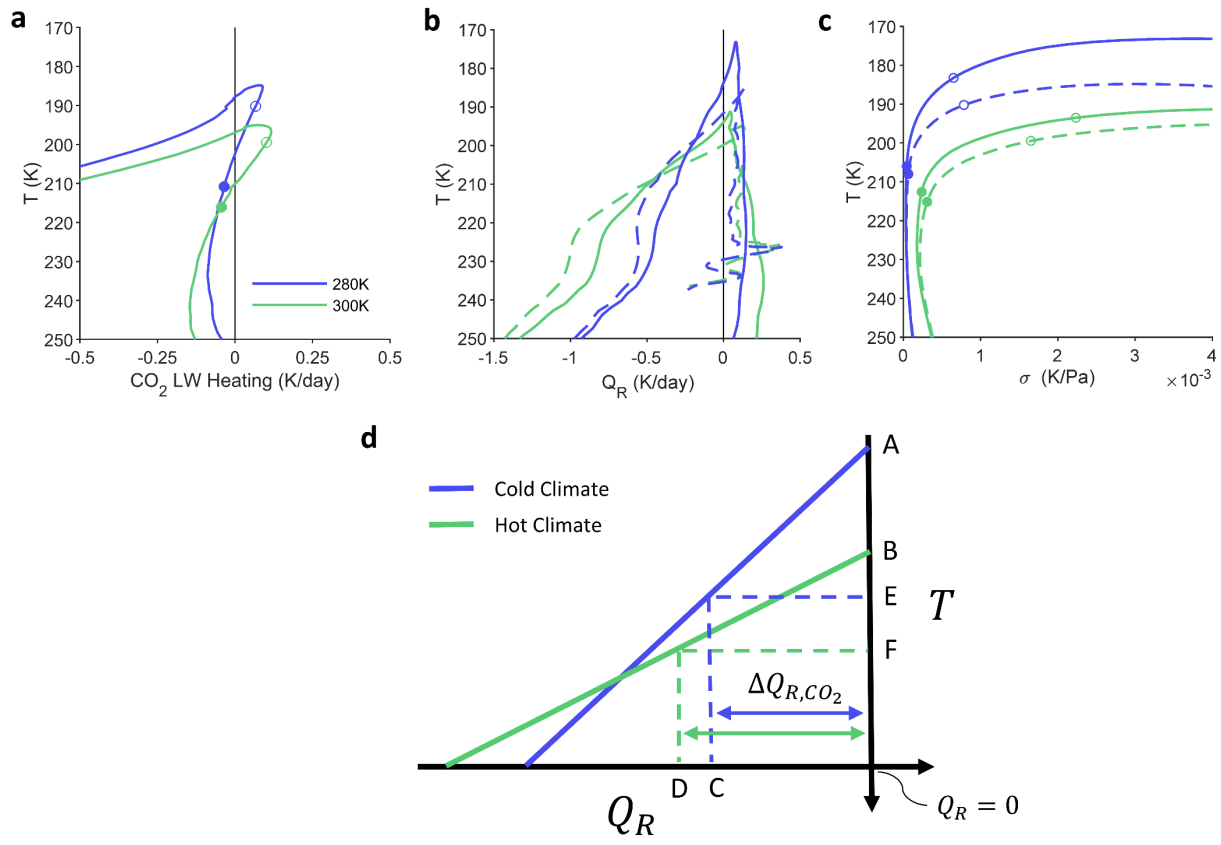


**Figure 5.3. The role of $CO_2$.** (a) The $CO_2$ clear-sky longwave heating rate in the Standard experiment, as obtained from offline calculations. The open circles indicate RT. The closed circles indicate $T_{Conv}$. (b) Radiative heating rate for the Standard experiment (dashed lines) and the Standard, no $CO_2$ experiment (solid lines). (c) Static stability for the Standard experiment (dashed lines) and the Standard, no $CO_2$ experiment (solid lines). (d) Conceptual picture of how $CO_2$ helps to set RT temperature. Points A and B denote the RT without $CO_2$. Points C and D denote $-\Delta Q_{R,CO_2}$. Points E and F denote the RT with $CO_2$.

To understand the difference in RT *trend* with warming, we offer a schematic explanation in Fig. 5.3d. The solid lines are the longwave heating rate for an atmosphere without $CO_2$ in the vicinity of RT, plotted against a temperature vertical coordinate. That is, we have zoomed in on the upper portion Fig. 5.3b. The magnitude of $Q_R$ declines with decreasing temperature as the water vapor concentration becomes too small to efficiently cool the atmosphere, and its dependence on temperature is dominated by this mechanism (Hartmann & Larson, 2002; Jeevanjee & Fueglistaler,

2020). In an atmosphere without $CO_2$, RT occurs at the intercept (e.g., point A). With $CO_2$, RT occurs at a lower, warmer level where the water vapor cooling can offset $CO_2$ heating (point E). As the climate warms, there are two competing factors at play: (1) the changing slope of the $T$-$Q_R$ curve, and (2) the changing magnitude of $CO_2$ heating near RT. The slope of the $T$-$Q_R$ curve declines due to the greater characteristic upper-tropospheric cooling rate at warmer surface temperatures, as seen in Fig. 5.1c or 5.3b. This may be explained by pressure effects on the transmission of radiation (Hartmann et al. 2022). The declining slope reduces the $CO_2$ effect on RT temperature. The $CO_2$ heating rate near RT is increasing with climate warming, which would enhance the $CO_2$ effect on RT temperature (Fig. 5.3a). This effect partially counters that of the declining slope of the $T$-$Q_R$ curve. In our simulations, the declining $T$-$Q_R$ slope dominates, so the RT temperature increases more slowly with $CO_2$ than without.

### 5.3.3 Sensitivity to insolation

Solar radiation also has a substantial effect on anvil and RT temperatures. With $CO_2$ still excluded, we also remove solar radiation from the model (Fig. 5.2b) and find that this cools both the RT and the anvil by about 10 K in all simulations. This is easily understood as the result of a colder stratospheric radiative equilibrium temperature, as $H_2O$, $O_3$, and $O_2$ are all responsible for shortwave heating there. Since RT is the intersection of the approximate radiative equilibrium profile above and the tropospheric RCE profile below, the colder radiative equilibrium temperature results in a colder RT. Figure 5.2b also shows that a doubling of solar radiation has an analogous warming effect on both RT and anvil. Curiously, for both No Solar and 2x Solar, the trends $\Delta T_{RT}/\Delta T_s$ and $\Delta T_{Anv}/\Delta T_s$ are not especially sensitive to solar radiation. Since ozone heating is usually considered responsible for anvil warming, it might be surprising that this PHAT behavior

persists in the absence of solar radiation. However, longwave heating by ozone is about as strong as its shortwave heating in the upper troposphere and tropopause layer (Thuburn & Craig, 2002), so even in the absence of shortwave radiation there remains a substantial vertical gradient in ozone heating. Figure 5.2c shows three additional experiments, $H_2O$-only SW, $O_3$-only SW, and $O_2$-only SW, which selectively turn off all shortwave absorption except by $H_2O$, $O_3$, and $O_2$, respectively. These show that shortwave heating from any one of these constituents alone is sufficient to produce much of the response to solar radiation.

### 5.3.4 Sensitivity to O3

Our choices regarding ozone have a profound effect on the simulated trends of anvil and RT temperature. The RCEMIP ozone profile is based on the equatorial climatology so that it increases with height in the upper troposphere and lower stratosphere. Thus, when the surface warms, the troposphere is lifted into a region of greater ozone concentration. Beginning again from the Standard setup, we now manipulate ozone. In the Unif-O3 experiment we remove ozone's vertical structure by prescribing a vertically uniform profile of the same column mass as in the Standard experiment. Indeed, the warming of the RT as well as anvil are greatly reduced compared to the Standard experiment, to $\Delta T_{RT}/\Delta T_s = 0.09$ and $\Delta T_{Anv}/\Delta T_s = 0.14$, respectively.

The No-$O_3$ experiment achieved a similar result to Unif-O3 (Fig. 5.4d), as $\Delta T_{RT}/\Delta T_s = 0.14$ and $\Delta T_{Anv}/\Delta T_s = 0.00$. The small change in anvil temperature replicates the findings of Harrop and Hartmann (Harrop & Hartmann, 2012) in a similar setup. Seeley et al. (Seeley, Jeevanjee, & Romps, 2019), in their analogous "full complexity" simulations, found a more strictly fixed RT temperature as well as a nearly fixed anvil temperature for surface temperatures greater than freezing. That study used a different model and a small 3D domain, choices which may affect the

RT temperature trend. At a tropical Earth-like surface temperature of 300K, the No-$O_3$ experiment shows a colder anvil and RT than the Standard experiment, whereas the Unif-$O_3$ experiment is a closer match since the ozone heating warms both the anvil and RT.

### 5.3.5 Sensitivity to organization, domain geometry, and parameterizations

Finally, we verify that our choice of a small 2D domain and lack of convective organization do not affect our earlier conclusions. Figure 5.2e shows the anvil and RT temperatures for the two large-domain experiments, as well as the Standard experiment. In one experiment the radiative heating is horizontally homogenized, preventing convective organization, and in the other radiation is interactive to allow organization. Compared to the standard, small-domain simulations presented in Fig. 5.1 and depicted by the black marks in Fig. 5.2e, the anvil temperature and RT temperature are both slightly warmer but display otherwise similar trends with warming. The warmer RT and anvil may be explained by the large-domain simulations having reduced upper-tropospheric relative humidity, moving the effective emission level to a lower, warmer location (Appendix Fig. 5.10a). This is analogous to the findings by Harrop & Hartmann (Harrop & Hartmann, 2012), who found that artificially reducing the amount of upper tropospheric water vapor passed to the radiation scheme increased anvil temperature. Convective organization does not appear to affect the anvil temperature's trend with warming, consistent with previous studies (Harrop & Hartmann, 2012; Wing et al., 2020).

Figure 5.2f shows a series of simulations using a small 3D domain, as well as simulations using Thompson two-moment microphysics (G. Thompson et al., 2008). In either case, the anvil is considerably colder than in the Standard experiment, but the trend with climate warming is similar. The anvil-RT relationship remains robust. The colder anvils appear to be the result of

greater upper tropospheric humidity in those experiments, which would move the emission level to a colder temperature (Appendix Fig. 5.10a). This may arise from, or be complementary to, cloud-radiative interactions or differences between 2D and 3D convection. Another experiment using the CAM3 radiation scheme (Collins et al., 2006) demonstrates that the sensitivity to our choice of radiation parameterization is small.

## 5.4 An Anvil-Radiative Tropopause Relationship

Throughout our experiments, we find that the temperature of the cloud anvil is empirically related to the temperature of RT. Figure 5.4a shows the anvil temperature plotted against the RT temperature for each simulation we conducted. Anvil and RT always occur at different locations and temperatures from one another, yet they appear closely related. If a simulation results in a warmer RT, then it generally yields a warmer anvil. This behavior appears particularly robust when comparing the temperature trends $\Delta T_{trop}/\Delta T_s$ and $\Delta T_{anv}/\Delta T_s$ for a single experimental configuration (Fig. 5.5a). The anvil-RT relationship is robust over 120 simulations in a wide range of model settings. This is our central result.

Insofar as the anvil location is set by the location of radiatively-driven convergence, we would expect those locations to have similar temperatures. We define a convergence-weighted temperature similar to how we defined an anvil temperature before:

$$T_{Conv} = \frac{\int_{p_{80\%,\uparrow}}^{p_{80\%,\downarrow}} T(p) \cdot (-\nabla_{\mathrm{H}} \cdot \mathbf{U})_R \, dp}{\int_{p_{80\%,\uparrow}}^{p_{80\%,\downarrow}} (-\nabla_{\mathrm{H}} \cdot \mathbf{U})_R \, dp} \tag{16}$$

where $p_{80\%,\uparrow}$ and $p_{80\%,\downarrow}$ are the highest and lowest pressure levels where $(-\nabla_{\mathrm{H}} \cdot \mathbf{U})_R$ is at least 80% of its maximum value. Figure 5.4b shows the relationship between this convergence-weighted

temperature and anvil temperature. As found by previous studies of CRMs, GCMs, and observations, the temperature of cloud anvils is well-predicted by the convergence temperature.

The empirical relationship between RT temperature, anvil temperature, and convergence temperature suggests that anvil and RT arise from related physics. If convection is comprised of a spectrum of plumes with varying entrainment rates (Arakawa & Schubert, 1974), then the non-dilute (non-entraining) plume reaches the greatest altitude. The level of neutral buoyancy for the non-dilute plume occurs near RT, as convection would not be buoyant in the stable temperature profile substantially above RT. It detrains there, setting the temperature as that of the moist adiabat. Below that level, dilute plumes are responsible for setting the temperature as colder than the moist adiabat. See, for example, Figs. 1a and 2f from Zhou & Xie (Zhou & Xie, 2019), which show a sharp increase in temperature relative to the moist adiabat at the top of the troposphere. This causes static stability to increase with height below RT, as seen in our Fig. 5.1d. The static stability profile then links RT to the level of convergence and anvil according to Eqs. (2) and (4).

This explanation resembles that of Hartmann et al. (2019), who noted that due to convective overshooting, the least entraining plumes inject relatively cold air above the level of the anvil (see also, Kuang and Bretherton 2004). This causes a buoyancy flux divergence which must be balanced by radiative heating, so RT appears there. Figure 5.6 shows a plot of virtual potential temperature flux in our Standard experiment. It is expressed as an energy flux $\rho c_p \overline{w'\theta_v'}$. Above the level of zero buoyancy flux, where $\overline{w'\theta_v'} = 0$, significant convective activity is present due to overshooting. RT occurs above the minimum in virtual potential temperature flux, where there is flux divergence. The temperature at the level of zero buoyancy flux is very close to $T_{Conv}$, indicating that convection tends to lose its buoyancy near the level of large-scale divergence from convection. The temperature at the level of zero buoyancy flux increases with surface warming at

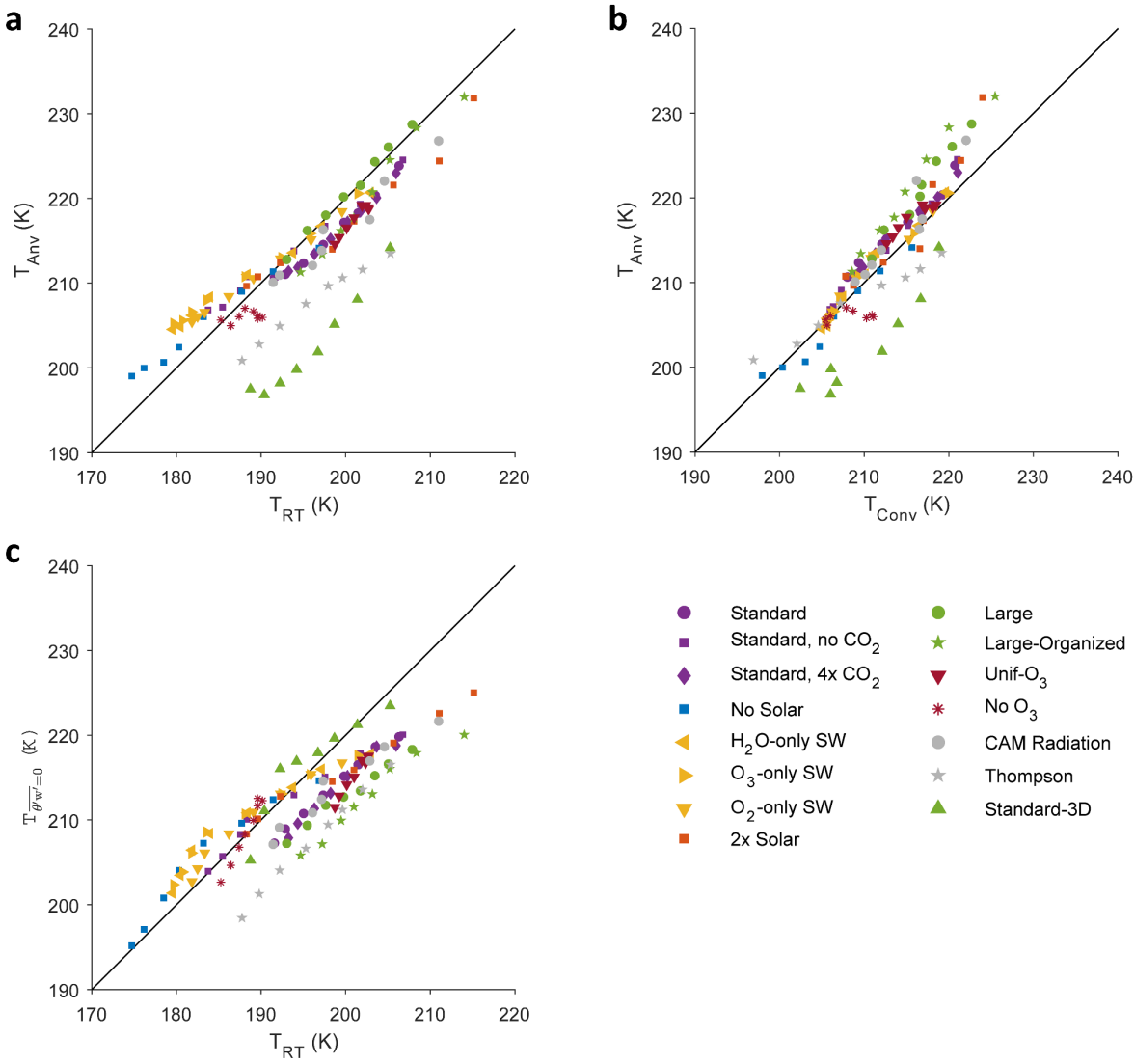


**Figure 5.4. Relationship between $T_{RT}$ and $T_{Anv}$.** (A) $T_{Anv}$ plotted against $T_{RT}$ for each simulation in this study. (B) $T_{Anv}$ plotted against $T_{Conv}$ for each simulation in this study. (c) $T_{\overline{w'\theta'_v}=0}$ plotted against $T_{RT}$ for each simulation in this study. A one-to-one line is shown in black as an aid to the reader.

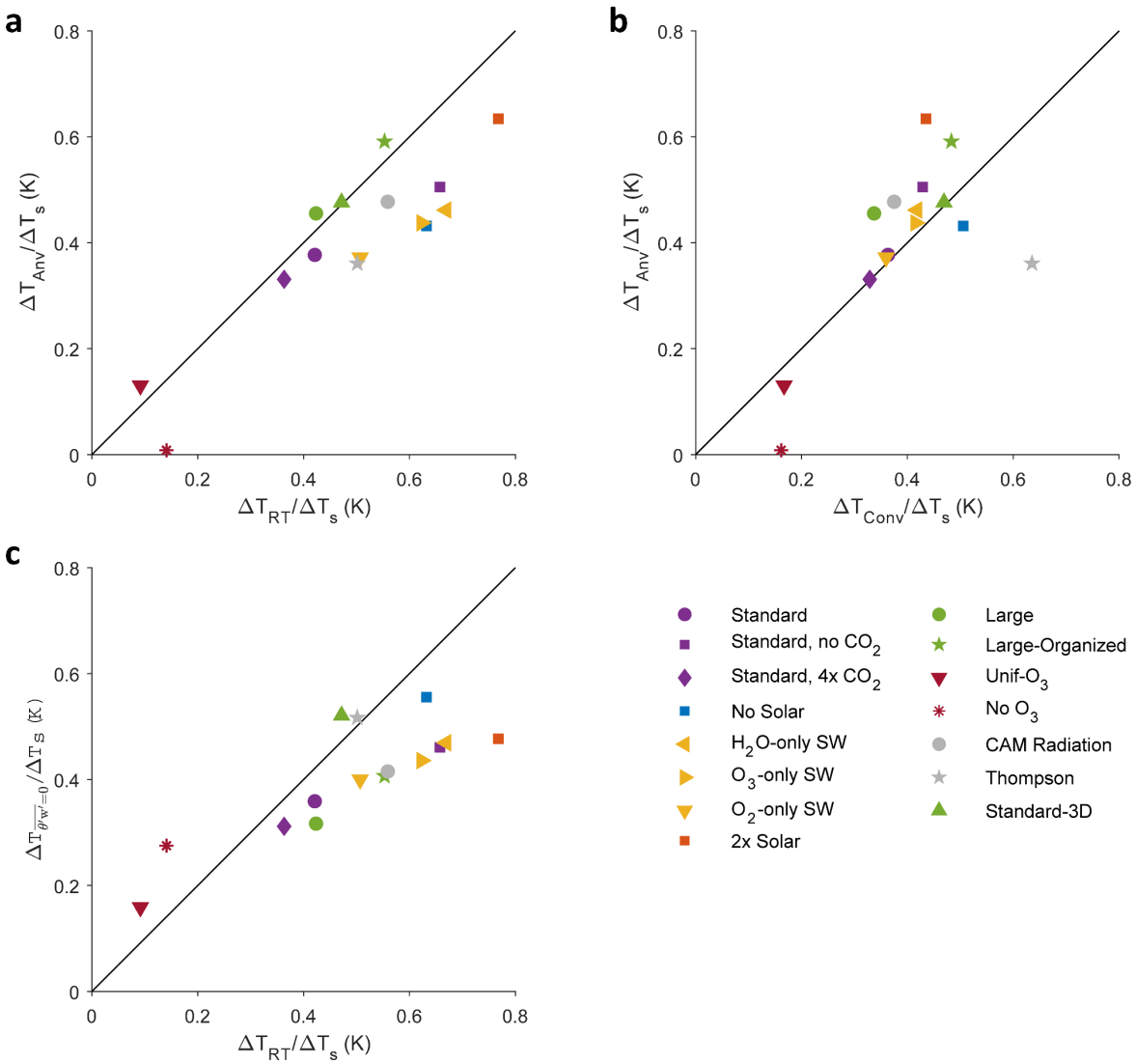


**Figure 5.5. Relationship between $\Delta T_{RT}$ and $\Delta T_{Anv}$.** (A) $\Delta T_{Anv}/\Delta T_s$ plotted against $\Delta T_{RT}/\Delta T_s$ for each simulation in this study. (B) $\Delta T_{Anv}/\Delta T_s$ plotted against $\Delta T_{Conv}/\Delta T_s$for each simulation in this study. (c) $\Delta T_{\overline{w'\theta_v'}=0}/\Delta T_s$ plotted against $\Delta T_{RT}/\Delta T_s$ for each simulation in this study. A one-to-one line is shown in black as an aid to the reader.

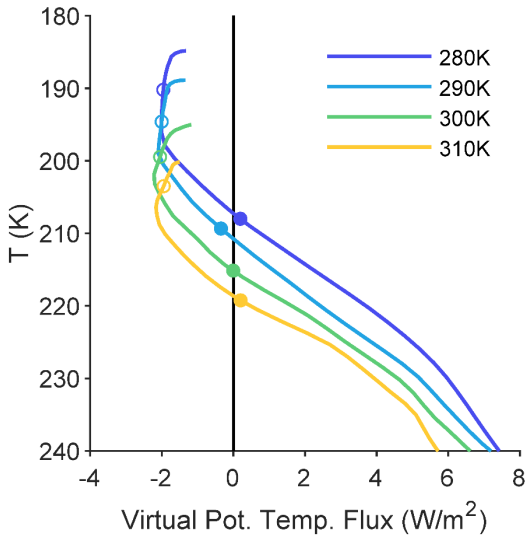


**Figure 5.6. Virtual potential temperature flux in the Standard experiment.** The open circles indicate RT. The closed circles indicate $T_{Conv}$. Data are cut off at the cold point.

a rate comparable to both RT and anvil ($\Delta T_{\overline{w'\theta_v'}=0}/\Delta T_s = 0.36$). Plots comparing the temperatures at the level of zero buoyancy flux and at RT across all our simulations show that they indeed covary (Figs. 4c and 5c). This corroborates the explanation provided by Hartmann et al.

However, 1D radiative-convective models simulate a similar RT temperature and trend to that found in our Standard experiment when given the same RCEMIP radiation parameters (see Kluft et al. 2019, or the "hard convective adjustment" simulations in Dacie et al. 2019). The simplest such models do not simulate or parameterize overshooting convection and its associated negative buoyancy flux, and the level of neutral buoyancy is essentially set at RT. The fact that RT is well represented in these models suggests that RT is not caused or set by the reversal in buoyancy flux. Regardless of the particular explanation, when the modeled RT and anvil each remain at a nearly fixed temperature, as in our Unif-$O_3$ and No-$O_3$ experiments, this behavior likely arises in part from the FAT mechanism. That is, the Clausius-Clapeyron scaling of saturation vapor pressure

causes $H_2O$ radiative cooling to decline near a fixed temperature (Hartmann & Larson, 2002; Jeevanjee & Fueglistaler, 2020).

## 5.5 Tug of war: rising $O_3$ profiles vs. surface warming

Our Standard simulations used an ozone profile which is fixed in pressure despite a warming surface. This is unrealistic. In the real tropical atmosphere, the ozone profile would evolve in response to deeper convective mixing of small tropospheric ozone concentrations. Additionally, upward transport of ozone may increase as stratospheric upwelling intensifies with surface warming (Lin et al., 2017). A fixed-in-pressure ozone profile will alter the equilibrium RT temperature, as ozone is the main absorber responsible for radiative heating there (Thuburn & Craig, 2002). As shown in our simulations, surface warming leads to a warmer RT with a fixed $O_3$ profile. However, lifting the $O_3$ profile can lead to the local decline of ozone heating, which tends to reduce temperature. Therefore, there is a "tug of war" between the two effects to determine how RT temperature responds to climate warming in the real tropical atmosphere. We cannot predict the anvil or RT temperature trend with warming using a fixed ozone profile.

To investigate the role of ozone, past studies have artificially increased upper-tropospheric ozone, leading to greater anvil temperature (Kuang & Hartmann, 2007) as well as greater RT temperature (Birner & Charlesworth, 2017; Dacie et al., 2019). Other authors have simply removed ozone entirely (Harrop & Hartmann, 2012; Jeevanjee & Romps, 2018; Seeley, Jeevanjee, & Romps, 2019), as in our No $O_3$ experiment. However, those idealized treatments of the ozone profile cannot provide a quantitative estimate of how ozone influences the warming trend of anvil or RT. Does the rising troposphere or declining ozone concentration win the tug of war, or do they cancel one another? To answer that question, we shall prescribe ozone from the Whole Atmosphere

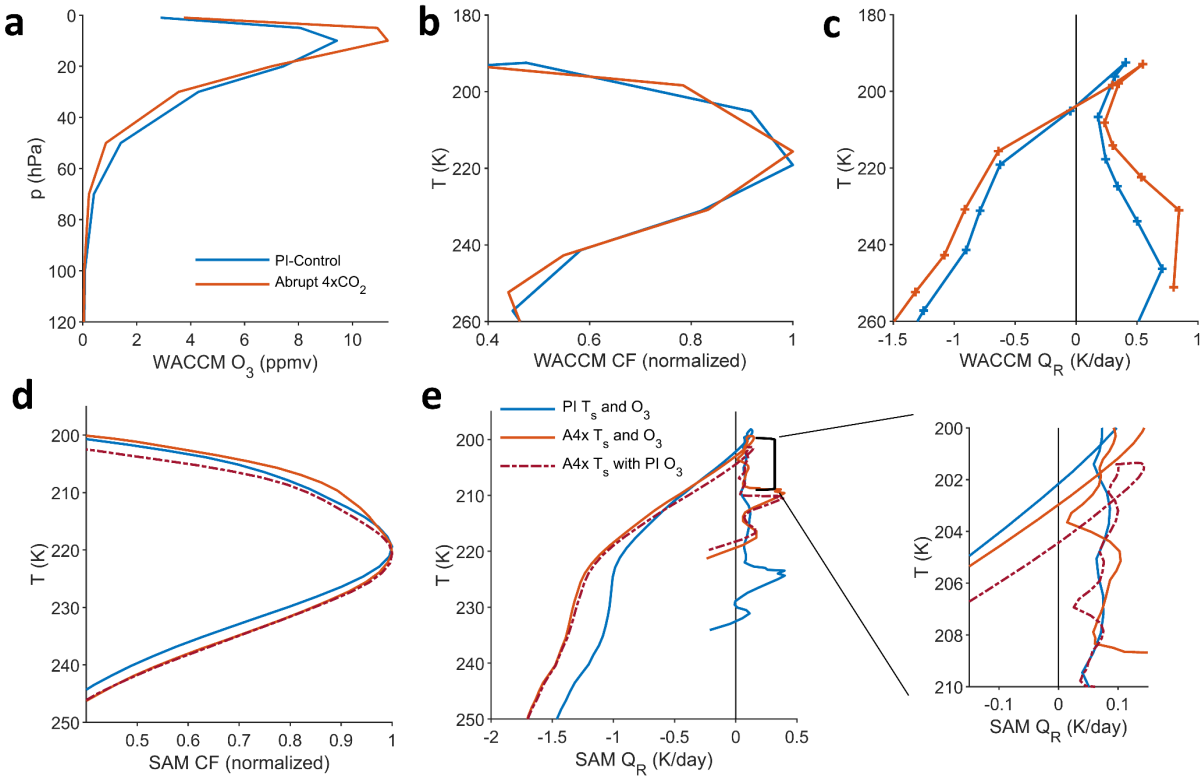


**Figure 5.7. CESM2-WACCM simulations and WACCM-informed SAM simulations.** (a) CESM2-WACCM ozone. (b) Cloud fraction plotted against a temperature coordinate. (c) Radiative heating plotted against temperature. (d) Normalized cloud fraction for the SAM simulations based on WACCM surface temperature and ozone. (e) Radiative heating for the SAM simulations based on WACCM surface temperature and ozone.

Community Climate Model (CESM2-WACCM6), which employs coupled ozone chemistry (Gettelman et al., 2019).

We use WACCM6 data from a pre-industrial control run in which the $CO_2$ concentration is fixed at 280 ppm ("piControl"), as well as a simulation of the response to an abrupt quadrupling of $CO_2$ concentration ("abrupt-4xCO2") (Gokhan Danabasoglu, 2019; Eyring et al., 2016). Those two experiments are commonly used for estimating climate feedbacks, and the large forcing results in a large difference in surface temperature. For either simulation we average the final 50 years of data, within 10 degrees of the equator. In that region, tropical sea surface temperature increases

from 301.21 K at the end of the piControl simulation to 306.65 K at the end of the abrupt-4xCO2 simulation. Figure 5.7a shows that as the climate warms, the ozone concentration decreases below the 20 hPa level and increases above. Figure 5.7b shows that the normalized cloud profiles are nearly the same in a temperature coordinate.[4] WACCM simulates a FAT in the deep tropics. Figure 5.7c shows that WACCM also simulates a FiTT in the deep tropics: RT temperature increases by only 0.05 K. The coarse resolution and small surface temperature increment of the GCM output undercut the precision of this estimate, but it is nevertheless a striking result.

To what extent does the shifted ozone profile account for the apparent temperature-invariance of the WACCM radiative tropopause and anvil clouds? We modify our Standard formulation of 2D SAM. We conduct one simulation with the piControl surface temperature and ozone profile and a second simulation with the abrupt-4xCO2 surface temperature and ozone profile. As a mechanism-denial experiment, we conduct a third simulation with the warmer abrupt-4xCO2 surface temperature and the piControl ozone profile, which is shifted lower in altitude compared to the abrupt-4xCO2 ozone profile. Consistent with the GCM simulations, we increase $CO_2$ by four times in both warming simulations.

Figure 5.7d shows the cloud fraction profiles of the WACCM-informed SAM simulations. With ozone prescribed to match the surface temperature, the normalized cloud fraction profile is nearly unchanged with respect to temperature. $T_{Anv}$, calculated according to Eq. (12). increases by less than 0.1 K so that $\Delta T_{Anv}/\Delta T_s = .01$. When ozone is instead fixed, $T_{anv}$ increases by 1.3 K so that $\Delta T_{Anv}/\Delta T_s = .23$. The difference in $T_{Anv}$ between the two ozone treatments is mostly attributable

[4] $T_{anv}$ as calculated from Eq. (12) decreases from 217.2 K to 216.6 K. However, due to the coarseness of the GCM output, the sign and magnitude of that change depend non-monotonically on what percentage threshold we consider as the "anvil" in that formula.

to greater cloud amount above the peak in the realistic-ozone scenario. The temperature at the peak itself is nearly unchanged. Figure 5.7e shows the radiative heating profiles of all three simulations. When ozone matches the surface temperature, $T_{RT}$ increases by 0.8 K so that $\Delta T_{RT}/\Delta T_s = .15$. When ozone is instead fixed, $T_{RT}$ increases by 2.3 K so that $\Delta T_{RT}/\Delta T_s = .42$. The ozone-shifted results resemble the idealized No-$O_3$ experiment presented earlier. For both anvil and RT, the shifted ozone profile offsets most of the warming that would occur with fixed ozone. In summary, if ozone is realistically modeled as in WACCM, then the effects of increasing surface temperature and a lifted ozone profile roughly cancel one another to produce a FiTT as well as a FAT. However, the ozone we prescribe does not reflect the ozone sources and sinks associated with deep convection in SAM, but rather those of a different model. Also, our simulations are also performed without a Brewer-Dobson circulation, though Kuang & Hartmann (Kuang & Hartmann, 2007) found it had only a small effect on anvil temperature in an idealized CRM. In future studies it may also be worthwhile to investigate more than a single GCM's representation of ozone.

The difference in anvil warming between the fixed-ozone and lifted-ozone scenarios gives rise to a difference in top-of-atmosphere radiation in SAM. The cloud longwave radiative effect is 0.43 W/m$^2$ more positive when we prescribe ozone to shift upward (or .31 W/m$^2$ net including shortwave.) This results in a stronger positive cloud longwave feedback by about 0.08 W/m$^2$/K (or 0.06 W/m$^2$/K net including shortwave). This is smaller than the ozone-related cloud radiative effect of about 0.8 W/m$^2$ longwave feedback of 0.21 W/m$^2$/K found in a GCM by Nowack et al. (P. J. Nowack et al., 2015), which may be due in part to the comparatively smaller SAM cloud fraction profile[5].

[5] We are comparing the Nowack et al.'s B and C1 simulations. We estimated the cloud radiative effect using the Web Plot Digitizer (Rohatgi, 2019) for their Fig. 2c and a comparable 5.44 K of surface warming.

## 5.6 Discussion

We have shown that the temperatures of cloud anvils and radiative tropopause (RT) strongly covary across a wide range of model settings and surface temperatures in a 2D cloud-resolving model. This affirms the intuition in FAT thinking that anvils occur near the top of the troposphere where the radiative cooling rate declines towards zero (Hartmann & Larson, 2002). We have shown that the presence of $CO_2$ causes the anvil and RT temperatures to increase more slowly with surface warming than they otherwise would, and we have shown that solar radiation warms the RT and anvil. Both of these effects on RT temperature can be understood by considering the resulting change to the radiative equilibrium temperature there. Finally, we found that accounting for the shift in ozone profile with warming offsets the ozone-induced warming usually found in CRM studies, producing a nearly fixed RT temperature as well as a FAT.

Those results are significant in light of a recent contrary result. Seeley et al. (Seeley, Jeevanjee, & Romps, 2019) found that anvil temperature increased in spite of a fixed RT temperature in "minimal recipe" CRM simulations which isolated the longwave effect of water vapor from other gases present in Earth's atmosphere. Their anvil and RT may have become decoupled because that modeling choice resulted in a greater distance between anvil and RT than would be found in more earthlike simulations. In our Standard simulations the distance between anvil and RT is 2-3 km, substantially less than the 5-10 km reported for the minimal recipe simulations in Seeley et al. The minimal-recipe anvil warming may be partly attributable to the exclusion of $CO_2$, a choice we found to increase the temperature trend with warming (Fig. 5.2a). The Seeley et al. "full complexity" simulations, which contain $CO_2$, show very little anvil warming for surface temperatures above freezing. Using the same model and a similar fixed-$CO_2$ setup, Romps (Romps, 2020) found a near FAT for surface temperatures between 285 K and 315 K. Considering

the results of those studies as well as the present study, the FAT prediction appears well-supported by the modeling evidence. Therefore, the contribution of Seeley et al. is principally conceptual: Although theory strongly suggests that the anvil is linked to a decline in $H_2O$ radiative cooling at a fixed temperature (Hartmann & Larson, 2002; Jeevanjee & Fueglistaler, 2020), other radiatively-active gases and physical processes help to shape the anvil temperature trend, or lack thereof.

Our WACCM-informed simulations showed that RT temperature is nearly fixed when the ozone profile is lifted with climate warming to match the surface temperature. In the CMIP6 *piControl* and *abrupt-4x$CO_2$* experiments, used to estimate climate feedbacks and climate sensitivity, models without interactive ozone chemistry instead fix ozone at its pre-industrial concentrations (Eyring et al., 2016). For those models, our results suggests their RT and anvil may be biased towards warming. This would introduce a negative bias in cloud longwave feedback, similar to that found by Nowack et al. (P. J. Nowack et al., 2015, 2018). Models' representation of clouds may be improved if ozone can respond to the rising tropopause with climate change, as suggested in recent literature (Hardiman et al., 2019; Meraner et al., 2020; P. Nowack et al., 2018). The continued development of models with interactive ozone chemistry, such as those documented by the Chemistry-Climate Model Initiative (CCMI), may also improve the simulation of clouds (Morgenstern et al., 2017).

Finally, we mention several caveats to this study. To afford the computational expense of conducting 123 five-hundred-day simulations, we use a small, two-dimensional domain. We prescribe no mean ascent or descent, whereas real tropical anvil clouds form in the context of mean ascent in both the troposphere and the stratosphere. We homogenize the radiation in all our experiments except for one, which may decouple any cloud-radiation feedback. Our analysis relates cloud amount to the radiatively driven convergence in clear skies. However, that is not a

closed budget for cloud amount. Other factors are known to cause detrainment from the convective core, and cloud lifetime after detrainment depends on evaporation, microphysics, and within-cloud turbulence (Gasparini et al., 2019; Hartmann et al., 2018; Lilly, 1988; Seeley, Jeevanjee, Langhans, et al., 2019). The peak cloud amount itself also depends on microphysics as well as model resolution (Jeevanjee & Zhou, 2022; Sokol & Hartmann, 2022), and there is more work to be done to understand how cloud properties depend on these choices. As with other studies on this topic, we only consider the temperature of the cloud near its peak amount, not its effective radiating temperature, which may be different.

## 5.7 Appendix

The figures in this appendix are intended to support the analyses reported in this chapter, but they are not necessary for understanding the core results.

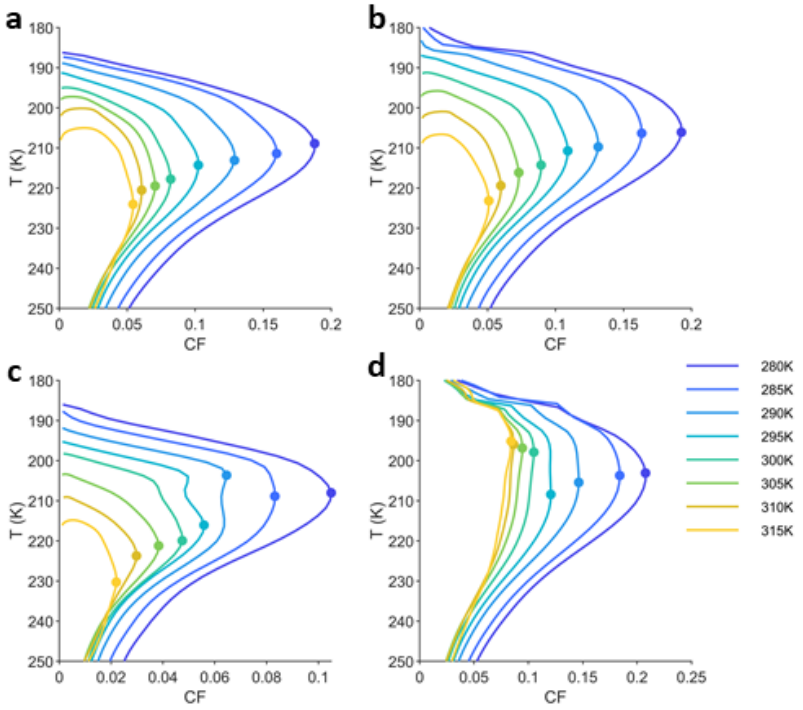


**Figure 5.8. Non-monotonic behavior of the anvil peak.** Profiles of cloud fraction, plotted against a temperature coordinate for (a) the Standard experiment, (b) the Standard, no $CO_2$ experiment, (c) the 2x Solar experiment, and (d) the No $O_3$ experiment. The circles mark the maximum in upper-tropospheric cloud fraction. In the 2x Solar and No $O_3$ experiments, temperature of maximum cloud fraction abruptly shifts as the shape of the cloud fraction profile changes.

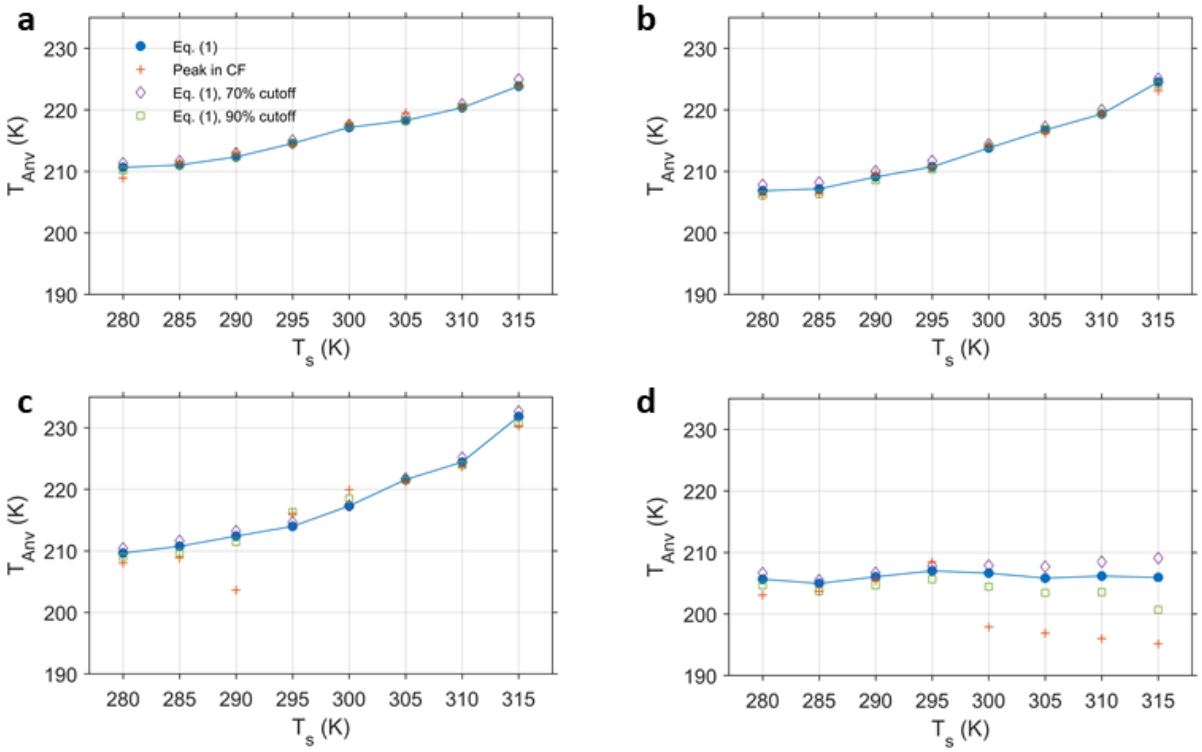


**Figure 5.9. Anvil temperature according to several definitions.** To demonstrate the robustness of Eq. (1), we show the anvil temperature as defined by (i) Eq. (1), (ii) the peak in CF (as in Fig. S1), (iii) Eq. (1), modified so that the "anvil" is declined to include all levels where cloud fraction as at least 70% of its maximum value, and (iv) Eq. (1), with a 90% cutoff. The different panels are for (a) the Standard experiment, (b) the Standard-no $CO_2$ experiment, (c) the 2x Solar experiment, and (d) the No $O_3$ experiment. Note the dependence on definition for the experiment without ozone.

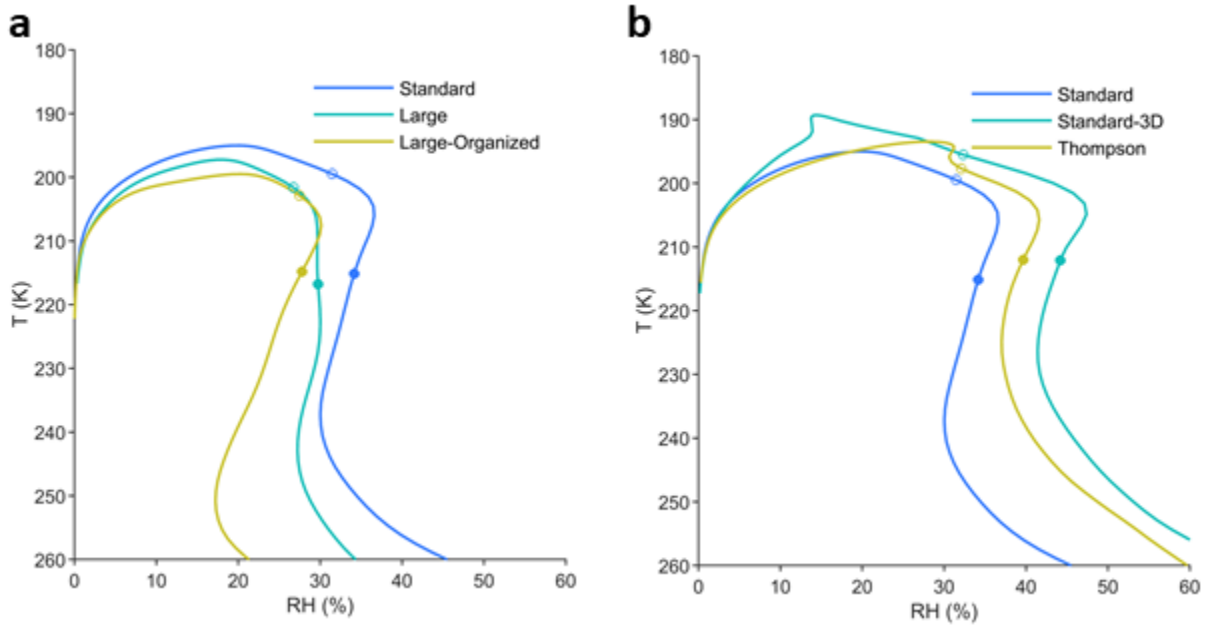


**Figure 5.10. Relative Humidity from selected experiments.** Data presented from the $T_s = 300\,K$ simulations.

# 6 References


Arakawa, A., & Schubert, W. H. (1974). Interaction of a Cumulus Cloud Ensemble with the Large-Scale Environment, Part I. *Journal of the Atmospheric Sciences*, *31*(3), 674–701. https://doi.org/10.1175/1520-0469(1974)031<0674:ioacce>2.0.co;2

Birner, T., & Charlesworth, E. J. (2017). On the relative importance of radiative and dynamical heating for tropical tropopause temperatures. *Journal of Geophysical Research*, *122*(13), 6782–6797. https://doi.org/10.1002/2016JD026445

Blossey, P. N., Kuang, Z., & Romps, D. M. (2010). Isotopic composition of water in the tropical tropopause layer in cloud-resolving simulations of an idealized tropical circulation. *Journal of Geophysical Research Atmospheres*, *115*(24). https://doi.org/10.1029/2010JD014554

Bogenschutz, P. A., Gettelman, A., Morrison, H., Larson, V. E., Craig, C., & Schanen, D. P. (2013). Higher-order turbulence closure and its impact on climate simulations in the community atmosphere model. *Journal of Climate*, *26*(23). https://doi.org/10.1175/JCLI-D-13-00075.1

Bony, S., Stevens, B., Frierson, D. M. W., Jakob, C., Kageyama, M., Pincus, R., et al. (2015). Clouds, circulation and climate sensitivity. *Nature Geoscience*, *8*(4), 261–268. https://doi.org/10.1038/ngeo2398

Bony, S., Stevens, B., Coppin, D., Becker, T., Reed, K. A., Voigt, A., & Medeiros, B. (2016). Thermodynamic control of anvil cloud amount. *Proceedings of the National Academy of Sciences*, *113*(32), 8927–8932. https://doi.org/10.1073/pnas.1601472113

Boucher, O., Randall, D., Artaxo, P., & Bretherton, C. S. (2013). *Chapter 7: Clouds and aerosols*. *Climate Change 2013 the Physical Science Basis: Working Group I Contribution to the Fifth Assessment Report of the Intergovernmental Panel on Climate Change* (Vol. 9781107057). https://doi.org/10.1017/CBO9781107415324.016

Bretherton, C. S., Peters, M. E., & Back, L. E. (2004). Relationships between water vapor path and precipitation over the tropical oceans. *Journal of Climate*, *17*(7), 1517–1528. https://doi.org/10.1175/1520-0442(2004)017<1517:RBWVPA>2.0.CO;2

Bretherton, C. S., Blossey, P. N., & Khairoutdinov, M. (2005). An energy-balance analysis of deep convective self-aggregation above uniform SST. *Journal of the Atmospheric Sciences*, *62*(12), 4273–4292. https://doi.org/10.1175/JAS3614.1

Budyko, M. I. (1969). The effect of solar radiation variations on the climate of the Earth. *Tellus*, *21*(5), 611–619. https://doi.org/10.3402/tellusa.v21i5.10109

Cai, M. (2005). Dynamical amplification of polar warming. *Geophysical Research Letters*, *32*(22), 1–5. https://doi.org/10.1029/2005GL024481

Charney, J. G. (1963). A Note on Large-Scale Motions in the Tropics. *Journal of the Atmospheric Sciences*, *20*, 607–609.

Collins, W. D., Rasch, P. J., Boville, B. A., Hack, J. J., McCaa, J. R., Williamson, D. L., et al. (2006). The formulation and atmospheric simulation of the Community Atmosphere Model version 3 (CAM3). *Journal of Climate*, *19*(11), 2144–2161. https://doi.org/10.1175/JCLI3760.1

Colman, R., & Soden, B. J. (2021). Water vapor and lapse rate feedbacks in the climate system. *Reviews of Modern Physics*, *93*(4). https://doi.org/10.1103/RevModPhys.93.045002

Cronin, T. W., & Wing, A. A. (2017). Clouds, Circulation, and Climate Sensitivity in a Radiative-Convective Equilibrium Channel Model. *Journal of Advances in Modeling Earth Systems*, *9*(8), 2883–2905. https://doi.org/10.1002/2017MS001111

Cvijanovic, I., & Caldeira, K. (2015). Atmospheric impacts of sea ice decline in CO2 induced global warming. *Climate Dynamics*, *44*(5–6), 1173–1186. https://doi.org/10.1007/s00382-015-2489-1

Dacie, S., Kluft, L., Schmidt, H., Stevens, B., Buehler, S. A., Nowack, P. J., et al. (2019). A 1D RCE study of factors affecting the tropical tropopause layer and surface climate. *Journal of Climate*, *32*(20), 6769–6782. https://doi.org/10.1175/JCLI-D-18-0778.1

Danabasoglu, G., Lamarque, J. F., Bacmeister, J., Bailey, D. A., DuVivier, A. K., Edwards, J., et al. (2020). The Community Earth System Model Version 2 (CESM2). *Journal of Advances in Modeling Earth Systems*, *12*(2). https://doi.org/10.1029/2019MS001916

Danabasoglu, Gokhan. (2019). *NCAR CESM2-WACCM model output prepared for CMIP6 CMIP abrupt-4xCO2*. https://doi.org/22033/ESGF/CMIP6.10039

Emanuel, K., Wing, A. A., & Vincent, E. M. (2014). Radiative-convective instability. *Journal of Advances in Modeling Earth Systems*, *6*(1), 75–90. https://doi.org/10.1002/2013MS000270

EMANUEL, K. A., NEELIN, J. D., & BRETHERTON, C. S. (1994). On large-scale circulations in convecting atmospheres. *Quarterly Journal of the Royal Meteorological Society*, *120*(519), 1111–1143. https://doi.org/10.1256/smsqj.51901

Evans, D., Sagoo, N., Renema, W., Cotton, L. J., Müller, W., Todd, J. A., et al. (2018). Eocene greenhouse climate revealed by coupled clumped isotope-Mg/Ca thermometry. *Proceedings of the National Academy of Sciences*, *115*(6), 1174–1179. https://doi.org/10.1073/pnas.1714744115

Eyring, V., Bony, S., Meehl, G. A., Senior, C. A., Stevens, B., Stouffer, R. J., & Taylor, K. E. (2016). Overview of the Coupled Model Intercomparison Project Phase 6 (CMIP6) experimental design and organization. *Geoscientific Model Development*, *9*(5), 1937–1958. https://doi.org/10.5194/gmd-9-1937-2016

Flato, G., Marotzke, J., Abiodun, B., Braconnot, P., Chou, S. C., Collins, W. D., et al. (2013). *Chapter 9: Evaluation of Climate Models*. *Climate Change 2013: The Physical Science Basis. Contribution of Working Group I to the Fifth Assessment Report of the Intergovernmental Panel on Climate Change*. https://doi.org/10.1017/CBO9781107415324

Forster, P. M., Storelvmo, T., Armour, K., Collins, W., Dufresne, J. L., Frame, D., et al. (2021). Chapter 7: The Earth's Energy Budget, Climate Feedbacks, and Climate Sensitivity. *Climate Change 2021: The Physical Science Basis. Contribution of Working Group I to the Sixth Assessment Report of the Intergovernmental Panel on Climate Change*, (August).

Frieling, J., Gebhardt, H., Huber, M., Adekeye, O. A., Akande, S. O., Reichart, G. J., et al. (2017). Extreme warmth and heat-stressed plankton in the tropics during the Paleocene-Eocene Thermal Maximum. *Science Advances*, *3*(3), e1600891. https://doi.org/10.1126/sciadv.1600891

Gasparini, B., Blossey, P. N., Hartmann, D. L., Lin, G., & Fan, J. (2019). What Drives the Life Cycle of Tropical Anvil Clouds? *Journal of Advances in Modeling Earth Systems*, *11*(8). https://doi.org/10.1029/2019MS001736

Gettelman, A., Mills, M. J., Kinnison, D. E., Garcia, R. R., Smith, A. K., Marsh, D. R., et al. (2019). The Whole Atmosphere Community Climate Model Version 6 (WACCM6). *Journal of Geophysical Research: Atmospheres*, *124*(23), 12380–12403. https://doi.org/10.1029/2019JD030943

Grabowski, W. W., Yano, J. I., & Moncrieff, M. W. (2000). Cloud resolving modeling of tropical circulations driven by large-scale SST gradients. *Journal of the Atmospheric Sciences*, *57*(13), 2022–2039. https://doi.org/10.1175/1520-0469(2000)057<2022:crmotc>2.0.co;2

Hardiman, S. C., Andrews, M. B., Andrews, T., Bushell, A. C., Dunstone, N. J., Dyson, H., et al. (2019). The Impact of Prescribed Ozone in Climate Projections Run With HadGEM3-GC3.1. *Journal of Advances in Modeling Earth Systems*, *11*(11), 3443–3453. https://doi.org/10.1029/2019MS001714

Harrop, B. E., & Hartmann, D. L. (2012). Testing the role of radiation in determining tropical cloud-top temperature. *Journal of Climate*, *25*(17), 5731–5747. https://doi.org/10.1175/JCLI-D-11-00445.1

Hartmann, D. L., & Larson, K. (2002). An important constraint on tropical cloud - climate feedback. *Geophysical Research Letters*. https://doi.org/10.1029/2002gl015835

Hartmann, D. L., Gasparini, B., Berry, S. E., & Blossey, P. N. (2018). The Life Cycle and Net Radiative Effect of Tropical Anvil Clouds. *Journal of Advances in Modeling Earth Systems*, *10*(12). https://doi.org/10.1029/2018MS001484

Hartmann, D. L., Blossey, P. N., & Dygert, B. D. (2019). Convection and Climate: What Have We Learned from Simple Models and Simplified Settings? *Current Climate Change Reports*. https://doi.org/10.1007/s40641-019-00136-9

Hartmann, D. L., Dygert, B. D., Blossey, P. N., Fu, Q., & Sokol, A. B. (2022). The Vertical Profile of Radiative Cooling and Lapse Rate in a Warming Climate. *Journal of Climate*, 1–29. https://doi.org/10.1175/jcli-d-21-0861.1

Held, I. M., Hemler, R. S., & Ramaswamy, V. (1993). Radiative-convective equilibrium with explicit two-dimensional moist convection. *Journal of the Atmospheric Sciences*, *50*(23). https://doi.org/10.1175/1520-0469(1993)050<3909:RCEWET>2.0.CO;2

Held, Isaac M., & Shell, K. M. (2012). Using relative humidity as a state variable in climate feedback analysis. *Journal of Climate*, *25*(8), 2578–2582. https://doi.org/10.1175/JCLI-D-11-00721.1

Holloway, C. E., & Woolnough, S. J. (2016). The sensitivity of convective aggregation to diabatic processes in idealized radiative-convective equilibrium simulations. *Journal of Advances in Modeling Earth Systems*, *8*(1), 166–195. https://doi.org/10.1002/2015MS000511

Hope, C. (2015). The $10 trillion value of better information about the transient climate response. *Philosophical Transactions of the Royal Society A: Mathematical, Physical and Engineering Sciences*, *373*(2054). https://doi.org/10.1098/rsta.2014.0429

Hu, S., & Vallis, G. K. (2019). Meridional structure and future changes of tropopause height and temperature. *Quarterly Journal of the Royal Meteorological Society*, *145*(723), 2698–2717. https://doi.org/10.1002/qj.3587

Hu, Z., Lamraoui, F., & Kuang, Z. (2021). Influence of upper-troposphere stratification and cloud-radiation interaction on convective overshoots in the tropical tropopause layer. *Journal of the Atmospheric Sciences*, *78*(8), 2493–2509. https://doi.org/10.1175/JAS-D-20-0241.1

Huang, X., Chuang, H. W., Dessler, A., Chen, X., Minschwaner, K., Ming, Y., & Ramaswamy, V. (2013). A radiative-convective equilibrium perspective of weakening of the tropical walker circulation in response to global warming. *Journal of Climate*, *26*(5), 1643–1653. https://doi.org/10.1175/JCLI-D-12-00288.1

INGERSOLL AP. (1969). Runaway Greenhouse. History of Water on Venus. *Journal of the Atmospheric Sciences*, *26*(6), 1191–1198. https://doi.org/10.1175/1520-0469(1969)026<1191:trgaho>2.0.co;2

Jeevanjee, N., & Fueglistaler, S. (2020). Simple spectral models for atmospheric radiative cooling. *Journal of the Atmospheric Sciences*, *77*(2). https://doi.org/10.1175/JAS-D-18-0347.1

Jeevanjee, N., & Romps, D. M. (2018). Mean precipitation change from a deepening troposphere. *Proceedings of the National Academy of Sciences of the United States of America*, *115*(45), 11465–11470. https://doi.org/10.1073/pnas.1720683115

Jeevanjee, N., & Zhou, L. (2022). On the Resolution-Dependence of Anvil Cloud Fraction and Precipitation Efficiency in Radiative-Convective Equilibrium. *Journal of Advances in Modeling Earth Systems*, *14*(3). https://doi.org/10.1029/2021ms002759

Jeevanjee, N., Koll, D. D. B., & Lutsko, N. (2021). "Simpson's Law" and the Spectral Cancellation of Climate Feedbacks. *Geophysical Research Letters*, *48*(14). https://doi.org/10.1029/2021GL093699

Keating-Bitonti, C. R., Ivany, L. C., Affek, H. P., Douglas, P., & Samson, S. D. (2011). Warm, not super-hot, temperatures in the early Eocene subtropics. *Geology*, *39*(8), 771–774. https://doi.org/10.1130/G32054.1

Khairoutdinov, M., & Emanuel, K. (2013). Rotating radiative-convective equilibrium simulated by a cloud-resolving model. *Journal of Advances in Modeling Earth Systems*, *5*(4), 816–825. https://doi.org/10.1002/2013ms000253

Khairoutdinov, M. F., & Randall, D. A. (2003). Cloud Resolving Modeling of the ARM Summer 1997 IOP: Model Formulation, Results, Uncertainties, and Sensitivities. *Journal of the Atmospheric Sciences*, *60*(4), 607–625. https://doi.org/10.1175/1520-0469(2003)060<0607:CRMOTA>2.0.CO;2

Kluft, L., Dacie, S., Buehler, S. A., Schmidt, H., & Stevens, B. (2019). Re-examining the first climate models: Climate sensitivity of a modern radiative–convective equilibrium model. *Journal of Climate*, *32*(23), 8111–8125. https://doi.org/10.1175/JCLI-D-18-0774.1

Koll, D. D. B., & Cronin, T. W. (2018). Earth's outgoing longwave radiation linear due to H2O greenhouse effect. *Proceedings of the National Academy of Sciences of the United States of America*, *115*(41), 10293–10298. https://doi.org/10.1073/pnas.1809868115

Koll, D. D. B., Jeevanjee, N., & Lutsko, N. J. (2023). An Analytic Model of the Clear-Sky Longwave Feedback. *Journal of the Atmospheric Sciences*. https://doi.org/https://doi.org/10.1175/JAS-D-22-0178.1

Kopparapu, R. K., Ramirez, R., Kasting, J. F., Eymet, V., Robinson, T. D., Mahadevan, S., et al. (2013). Habitable zones around main-sequence stars: New estimates. *Astrophysical Journal*, *765*(2). https://doi.org/10.1088/0004-637X/765/2/131

Kuang, Z., & Bretherton, C. S. (2004). Convective influence on the heat balance of the tropical tropopause layer: A cloud-resolving model study. *Journal of the Atmospheric Sciences*, *61*(23). https://doi.org/10.1175/JAS-3306.1

Kuang, Z., & Hartmann, D. L. (2007). Testing the fixed anvil temperature hypothesis in a cloud-resolving model. *Journal of Climate*, *20*(10), 2051–2057. https://doi.org/10.1175/JCLI4124.1

Lee, S. (2014). A theory for polar amplification from a general circulation perspective. *Asia-Pacific Journal of Atmospheric Sciences*. https://doi.org/10.1007/s13143-014-0024-7

Lilly, D. K. (1988). Cirrus outflow dynamics. *Journal of the Atmospheric Sciences*, *45*(10). https://doi.org/10.1175/1520-0469(1988)045<1594:COD>2.0.CO;2

Lin, P., Paynter, D., Ming, Y., & Ramaswamy, V. (2017). Changes of the tropical tropopause layer under

global warming. *Journal of Climate*, *30*(4), 1245–1258. https://doi.org/10.1175/JCLI-D-16-0457.1

Lindzen, R. S., Chou, M.-D., & Hou, A. Y. (2001). Does the Earth Have an Adaptive Infrared Iris? *Bulletin of the American Meteorological Society*, *82*(3), 417–432. https://doi.org/10.1175/1520-0477(2001)082<0417:DTEHAA>2.3.CO;2

Masson-Delmotte, V., Schulz, M., Abe-Ouchi, A., Beer, J., Ganopolski, A., González Rouco, J. F., et al. (2014). *Chapter 5: Information from Paleoclimate Archives*. *Climate Change 2013: The Physical Science Basis. Contribution of Working Group I to the Fifth Assessment Report of the Intergovernmental Panel on Climate Change*. https://doi.org/10.1017/cbo9781107415324

Mauritsen, T., & Stevens, B. (2015). Missing iris effect as a possible cause of muted hydrological change and high climate sensitivity in models. *Nature Geoscience*, *8*(5), 346–351. https://doi.org/10.1038/ngeo2414

McKim, B. A., Jeevanjee, N., & Vallis, G. K. (2021). Joint Dependence of Longwave Feedback on Surface Temperature and Relative Humidity. *Geophysical Research Letters*, *48*(18). https://doi.org/10.1029/2021GL094074

Meraner, K., Rast, S., & Schmidt, H. (2020). How Useful Is a Linear Ozone Parameterization for Global Climate Modeling? *Journal of Advances in Modeling Earth Systems*, *12*(4). https://doi.org/10.1029/2019MS002003

Mlawer, E. J., Taubman, S. J., Brown, P. D., Iacono, M. J., & Clough, S. A. (1997). Radiative transfer for inhomogeneous atmospheres: RRTM, a validated correlated-k model for the longwave. *Journal of Geophysical Research: Atmospheres*, *102*(D14), 16663–16682. https://doi.org/10.1029/97jd00237

Mlawer, E. J., Payne, V. H., Moncet, J. L., Delamere, J. S., Alvarado, M. J., & Tobin, D. C. (2012). Development and recent evaluation of the MT-CKD model of continuum absorption. *Philosophical Transactions of the Royal Society A: Mathematical, Physical and Engineering Sciences*, *370*(1968). https://doi.org/10.1098/rsta.2011.0295

Morgenstern, O., Hegglin, M., Rozanov, E., O'Connor, F., Luke Abraham, N., Akiyoshi, H., et al. (2017). Review of the global models used within phase 1 of the Chemistry-Climate Model Initiative (CCMI). *Geoscientific Model Development*. https://doi.org/10.5194/gmd-10-639-2017

Muller, C., & Bony, S. (2015). What favors convective aggregation and why? *Geophysical Research Letters*, *42*(13), 5626–5634. https://doi.org/10.1002/2015GL064260

Muller, C. J., & Held, I. M. (2012). Detailed Investigation of the Self-Aggregation of Convection in Cloud-Resolving Simulations. *Journal of the Atmospheric Sciences*, *69*(8), 2551–2565. https://doi.org/10.1175/jas-d-11-0257.1

Narenpitak, P., Bretherton, C. S., & Khairoutdinov, M. F. (2017). Cloud and circulation feedbacks in a near-global aquaplanet cloud-resolving model. *Journal of Advances in Modeling Earth Systems*, *9*(2), 1069–1090. https://doi.org/10.1002/2016MS000872

Nowack, P., Braesicke, P., Haigh, J., Abraham, N. L., Pyle, J., & Voulgarakis, A. (2018). Using machine learning to build temperature-based ozone parameterizations for climate sensitivity simulations. *Environmental Research Letters*, *13*(10). https://doi.org/10.1088/1748-9326/aae2be

Nowack, P. J., Luke Abraham, N., Maycock, A. C., Braesicke, P., Gregory, J. M., Joshi, M. M., et al. (2015). A large ozone-circulation feedback and its implications for global warming assessments. *Nature Climate Change*, *5*(1). https://doi.org/10.1038/nclimate2451

Nowack, P. J., Abraham, N. L., Braesicke, P., & Pyle, J. A. (2018). The Impact of Stratospheric Ozone

Feedbacks on Climate Sensitivity Estimates. *Journal of Geophysical Research: Atmospheres*, *123*(9). https://doi.org/10.1002/2017JD027943

Pagani, M., Huber, M., & Sageman, B. (2013). Greenhouse Climates. In *Treatise on Geochemistry: Second Edition* (Vol. 6, pp. 281–304). Elsevier. https://doi.org/10.1016/B978-0-08-095975-7.01314-0

Pearson, P. N., van Dongen, B. E., Nicholas, C. J., Pancost, R. D., Schouten, S., Singano, J. M., & Wade, B. S. (2007). Stable warm tropical climate through the Eocene Epoch. *Geology*, *35*(3), 211–214. https://doi.org/10.1130/G23175A.1

Pierrehumbert, R. T. (1995). Thermostats, Radiator Fins, and the Local Runaway Greenhouse. *Journal of the Atmospheric Sciences*, *52*(10), 1784–1806. https://doi.org/10.1175/1520-0469(1995)052<1784:trfatl>2.0.co;2

Pierrehumbert, R. T., Abbot, D. S., Voigt, A., & Koll, D. (2011). Climate of the neoproterozoic. *Annual Review of Earth and Planetary Sciences*, *39*. https://doi.org/10.1146/annurev-earth-040809-152447

Rohatgi, A. (2019). https://automeris.io/WebPl otDigitizer/.

Romps, D. M. (2014). An analytical model for tropical relative humidity. *Journal of Climate*, *27*(19), 7432–7449. https://doi.org/10.1175/JCLI-D-14-00255.1

Romps, D. M. (2017). Exact expression for the lifting condensation level. *Journal of the Atmospheric Sciences*, *74*(12). https://doi.org/10.1175/JAS-D-17-0102.1

Romps, D. M. (2020). Climate Sensitivity and the Direct Effect of Carbon Dioxide in a Limited-Area Cloud-Resolving Model. *Journal of Climate*, *33*(9), 3413–3429. https://doi.org/10.1175/jcli-d-19-0682.1

Schneider, T., Kaul, C. M., & Pressel, K. G. (2019). Possible climate transitions from breakup of stratocumulus decks under greenhouse warming. *Nature Geoscience*, *12*(3), 164–168. https://doi.org/10.1038/s41561-019-0310-1

Seeley, J. T., & Jeevanjee, N. (2021). H2O Windows and CO2 Radiator Fins: A Clear-Sky Explanation for the Peak in Equilibrium Climate Sensitivity. *Geophysical Research Letters*, *48*(4). https://doi.org/10.1029/2020GL089609

Seeley, J. T., Jeevanjee, N., & Romps, D. M. (2019). FAT or FiTT: Are Anvil Clouds or the Tropopause Temperature Invariant? *Geophysical Research Letters*. https://doi.org/10.1029/2018GL080096

Seeley, J. T., Jeevanjee, N., Langhans, W., & Romps, D. M. (2019). Formation of Tropical Anvil Clouds by Slow Evaporation. *Geophysical Research Letters*. https://doi.org/10.1029/2018GL080747

Seidel, S. D., & Yang, D. (2020). The lightness of water vapor helps to stabilize tropical climate. *Science Advances*, *6*(19). https://doi.org/10.1126/sciadv.aba1951

Sobel, A. H., Nilsson, J., & Polvani, L. M. (2002). The Weak Temperature Gradient Approximation and Balanced Tropical Moisture Waves*. *Journal of the Atmospheric Sciences*, *58*(23), 3650–3665. https://doi.org/10.1175/1520-0469(2001)058<3650:twtgaa>2.0.co;2

Soden, B. J., & Held, I. M. (2006). An assessment of climate feedbacks in coupled ocean-atmosphere models. *Journal of Climate*, *19*(14), 3354–3360. https://doi.org/10.1175/JCLI3799.1

Soden, B. J., Held, I. M., Colman, R. C., Shell, K. M., Kiehl, J. T., & Shields, C. A. (2008). Quantifying climate feedbacks using radiative kernels. *Journal of Climate*, *21*(14), 3504–3520. https://doi.org/10.1175/2007JCLI2110.1

Sokol, A. B., & Hartmann, D. L. (2022). Radiative Cooling, Latent Heating, and Cloud Ice in the Tropical Upper Troposphere. *Journal of Climate*, *35*(5). https://doi.org/10.1175/JCLI-D-21-0444.1

Thompson, D. W. J., Bony, S., & Li, Y. (2017). Thermodynamic constraint on the depth of the global tropospheric circulation. *Proceedings of the National Academy of Sciences of the United States of America*, *114*(31), 8181–8186. https://doi.org/10.1073/pnas.1620493114

Thompson, G., Field, P. R., Rasmussen, R. M., & Hall, W. D. (2008). Explicit forecasts of winter precipitation using an improved bulk microphysics scheme. Part II: Implementation of a new snow parameterization. *Monthly Weather Review*, *136*(12). https://doi.org/10.1175/2008MWR2387.1

Thuburn, J., & Craig, G. C. (2002). On the temperature structure of the tropical substratosphere. *Journal of Geophysical Research Atmospheres*, *107*(1–2). https://doi.org/10.1029/2001jd000448

Tompkins, A. M. (2001). Organization of tropical convection in low vertical wind shears: The role of water vapor. *Journal of the Atmospheric Sciences*, *58*(6), 529–545. https://doi.org/10.1175/1520-0469(2001)058<0529:OOTCIL>2.0.CO;2

Tompkins, A. M., & Craig, G. C. (1999). Sensitivity of tropical convection to sea surface temperature in the absence of large-scale flow. *Journal of Climate*, *12*(2), 462–476. https://doi.org/10.1175/1520-0442(1999)012<0462:SOTCTS>2.0.CO;2

Vallis, G. K., Zurita-Gotor, P., Cairns, C., & Kidston, J. (2015). Response of the large-scale structure of the atmosphere to global warming. *Quarterly Journal of the Royal Meteorological Society*, *141*(690), 1479–1501. https://doi.org/10.1002/qj.2456

Wing, A. A., Reed, K. A., Satoh, M., Stevens, B., Bony, S., & Ohno, T. (2018). Radiative-convective equilibrium model intercomparison project. *Geoscientific Model Development*. https://doi.org/10.5194/gmd-11-793-2018

Wing, A. A., Stauffer, C. L., Becker, T., Reed, K. A., Ahn, M. S., Arnold, N. P., et al. (2020). Clouds and Convective Self-Aggregation in a Multimodel Ensemble of Radiative-Convective Equilibrium Simulations. *Journal of Advances in Modeling Earth Systems*. https://doi.org/10.1029/2020MS002138

Yang, D. (2018a). Boundary Layer Diabatic Processes, the Virtual Effect, and Convective Self-Aggregation. *Journal of Advances in Modeling Earth Systems*, *10*(9), 2163–2176. https://doi.org/10.1029/2017MS001261

Yang, D. (2018b). Boundary Layer Height and Buoyancy Determine the Horizontal Scale of Convective Self-Aggregation. *Journal of the Atmospheric Sciences*, *75*(2), 469–478. https://doi.org/10.1175/jas-d-17-0150.1

Yang, D., & Seidel, S. D. (2020). The Incredible Lightness of Water Vapor. *Journal of Climate*. https://doi.org/10.1175/jcli-d-19-0260.1

Yang, D., & Seidel, S. D. (2023). Vapor buoyancy increases clear-sky thermal emission. *Environmental Research: Climate*, *2*(1), 015006. https://doi.org/10.1088/2752-5295/acba39

Yang, D., Zhou, W., & Seidel, S. D. (2022). Substantial influence of vapour buoyancy on tropospheric air temperature and subtropical cloud. *Nature Geoscience*, *15*(10), 781–788. https://doi.org/10.1038/s41561-022-01033-x

Yang, J., & Abbot, D. S. (2014). A low-order model of water vapor, clouds, and thermal emission for tidally locked terrestrial planets. *Astrophysical Journal*, *784*(2), 155. https://doi.org/10.1088/0004-637X/784/2/155

Zelinka, M. D., & Hartmann, D. L. (2010). Why is longwave cloud feedback positive? *Journal of Geophysical Research Atmospheres*. https://doi.org/10.1029/2010JD013817

Zelinka, M. D., & Hartmann, D. L. (2011). The observed sensitivity of high clouds to mean surface temperature anomalies in the tropics. *Journal of Geophysical Research Atmospheres*, *116*(23). https://doi.org/10.1029/2011JD016459

Zelinka, M. D., Myers, T. A., McCoy, D. T., Po-Chedley, S., Caldwell, P. M., Ceppi, P., et al. (2020). Causes of Higher Climate Sensitivity in CMIP6 Models. *Geophysical Research Letters*, *47*(1). https://doi.org/10.1029/2019GL085782

Zender, C. S. (1999). Global climatology of abundance and solar absorption of oxygen collision complexes. *Journal of Geophysical Research Atmospheres*, *104*(D20), 24471–24484. https://doi.org/10.1029/1999JD900797

Zhang, G. J., & McFarlane, N. A. (1995). Sensitivity of climate simulations to the parameterization of cumulus convection in the canadian climate centre general circulation model. *Atmosphere - Ocean*, *33*(3). https://doi.org/10.1080/07055900.1995.9649539

Zhou, W., & Xie, S. P. (2019). A conceptual spectral plume model for understanding tropical temperature profile and convective updraft velocities. *Journal of the Atmospheric Sciences*, *76*(9), 2801–2814. https://doi.org/10.1175/JAS-D-18-0330.1